Electromagnetic Inspection Method for Welding Imaging

A thesis submitted to The University of Manchester for the degree of

Doctor of Philosophy

in the Faculty of Science and Engineering

2019

By

Hanyang Xu

School of Electrical and Electronic Engineering

The University of Manchester

TABLE OF CONTENTS

TABLE OF CONTENTS 2

LIST OF ABBREVIATIONS AND NOMENCLATURE 6

LIST OF FIGURES 9

LIST OF TABLES 15

ABSTRACT 16

DECLARATION 17

COPYRIGHT STATEMENT 18

ACKNOWNLEDGEMENT 19

THE AUTHOR 20

PUBLICATIONS BY THE AUTHOR 21

Chapter 1 Introduction 22

1.1 Motivation 22

1.2 Aim and Objectives 24

1.3 Contributions 26

1.4 Thesis Outline 27

Chapter 2 Background 29

2.1 Welding Process and Microstructure 29

2.1.1 Pressure Welding 30

2.1.2 Fusion Welding 33

2.1.3 Microstructure of Weld 36
2.2 Welding Inspection Method 40
2.2.1 Destructive 41
2.2.2 Non-destructive 42
2.2.3 Electromagnetic Methods 46
2.3 Summary 49
Chapter 3 Support Theory 51
3.1 Fundamental of Inductive Sensor 51
3.1.1 Maxwell's Equations 51
3.1.2 Impedance of Sensor 53
3.1.3 Geometry Effect of Sample 55
3.2 Analytical Solution based on Dodd and Deeds 57
3.2.1 Analytical Solution for Co-axial Sensor 60
3.2.2 Analytical Solution for Non-axial Sensor 68
3.3 Summary 70
Chapter 4 Sensor Design 71
4.1 Design Strategy 71
4.2 Study of Traditional Sensor 72
4.2.1 FEM Model 73
4.2.2 Summary 75
4.3 Sensor Configurations 76

4.4 EM Instrument 77
4.5 Sensor Characterisation 79
4.5.1 Sensitivity 79
4.5.2 Spatial Resolution 81
4.6 Conductivity Invariance Phenomenon (CIP) 85
4.6.1 Influence of Conductivity Range 86
4.6.2 Influence of Excitation Frequency 89
4.6.3 Influence of Sample Thickness 90
4.6.4 Effect of Test Sample Dimension 94
4.7 Permeability Measurement Based on CIP 95
4.8 Summary 97
Chapter 5 Imaging of Weld Cross-section 99
5.1 Sample Preparation 99
5.1.1 Macrograph and Hardness 100
5.1.2 Micrograph 101
5.2 Imaging Procedure 103
5.3 EM Imaging with Inductance 105
5.4 EM Imaging with Offset-Crossing Frequency 108
5.4.1 Crossing Frequency Feature 108
5.4.2 Offset-Crossing Frequency Image 112
5.4.3 Relationship Between Offset-Crossing Frequency and Hardness 114

5.5 Summary 115

Chapter 6 Conclusion 117

6.1 Summary 117

6.2 Future Work 119

REFERENCES 121

Total words: 21624

LIST OF ABBREVIATIONS AND NOMENCLATURE

Abbreviations

AC	Alternating Current
ADC	Analogue to Digital Converter
BCC	Body-Centred Cubic
BM	Base Metal
CIP	Conductivity Invariance Phenomenon
CNC	Computer Numerical Control
CT	Computed Tomography
DAC	Digital to Analogue Converter
DP	Dual-Phase
DR	Digital Radiography
ECT	Eddy Current Testing
EM	Electromagnetic
EMATs	Electromagnetic Acoustic Transducers
EMI	Electromagnetic Interference
FCC	Face-Centred Cubic
FEM	Finite Element Method
FPGA	Field Programmable Gate Array
FSW	Friction Stir Welding
FZ	Fusion Zone

HAZ	Heat Affected Zone
HCP	Hexagonal Close-Packed
MPI	Magnetic Particle Inspection
NDT	Non-Destructive Testing
RT	Radiological Testing
SAW	Submerged Arc Welding
SNR	Signal to Noise Ratio
T-R	Transmitter-Receiver (Excitation-Pickup)
UKOPA	United Kingdom Onshore Pipeline Operators' Association
UT	Ultrasonic Testing
WN	Weld Nugget
WWII	World War II

Nomenclature

α , α -Fe	Body-centred cubic iron, Ferrite
γ , γ -Fe	Face-centred cubic iron, Austenite
ε	Hexagonal close-packed iron
δ , δ -Fe	The higher temperature designation of ferrite iron
α_a	Allotriomorphic ferrite
α_w	Widmanstätten ferrite
$\mathbf{E}$	Symbol of electric field intensity

$\mathbf{H}$	Symbol of magnetic intensity
$\mathbf{B}$	Symbol of magnetic flux density
$\mathbf{D}$	Symbol of electric flux density
$\mathbf{J}$	Symbol of current density
ρ	Symbol of electric charge density
μ	Symbol of the magnetic permeability
μ_0	Symbol of the magnetic permeability in free space
σ	Symbol of the electrical conductivity
ε	Symbol of the permittivity
ε_0	Symbol of the permittivity in free space
ω	Denotes the angular frequency
L	Denotes the inductance of a coil
$\boldsymbol{Z}_0$	Represents the impedance of a coil
l_1, l_2	Denotes the distance between the bottom or the top of a coil and the sample; (l_2 - l_1) denotes the lift-off
r_1, r_2	Denotes the inner and outer radii of a coil
c	Denotes the thickness of a tested sample
δ	Denotes the skin depth
f	Denotes the frequency
$\mathbf{A}$	Denotes the vector potential generated by a coil
$\mathbf{I}$, i_0	Denotes the exciting current density in a coil

LIST OF FIGURES

Figure 1.1 Spiral seam welding pipeline manufacturing 22

Figure 1.2 Product loss incident frequency by causes and size of leak in the period 1962 to 2017 cited from [1]. 23

Figure 2.1 Nomenclature of zones and boundaries for a weld joint [13] 30

Figure 2.2 Schematic of resistance spot welding. 31

Figure 2.3 (a) A FSW tool; and (b) Schematic of FSW process [21] 32

Figure 2.4 Schematic of SAW [26]. 34

Figure 2.5 The demonstration of the effect of welding speed on weld appearance and penetration (Cross-section area of the weld) [26]..... 35

Figure 2.6 The demonstration of the effect of filler angle on weld appearance and penetration [26]. 35

Figure 2.7 The phase diagram for pure iron [28]. The triple point temperature and pressure are 490℃ and 110 kbar, respectively. α, γ and ε refer to ferrite, austenite and ε-iron, respectively. δ is simply the higher temperature designation of α. 37

Figure 2.8 Mean volume per atom in iron crystals with dependence on temperature [28]..... 38

Figure 2.9 (a) Schematic of the essential constituents of the microstructure in the columnar austenite grains of a steel weld deposit.(b) Scanning electron micrograph of the microstructure of a steel weld [29]..... 39

Figure 2.10 Schematic of possible microstructural variation in the HAZ of steel welds [29]..... 40

Figure 2.11 Schematic illustration of film radiography, defect is displayed on the film as a projection 43
Figure 2.12 (a) Pitch-catch method with two transducers; (b) Pulse-echo method, transmitter, and receiver are the same transducer..... 45
Figure 3.1 Front view of an air core rectangular cross-section coil above a tested sample (c denotes the thickness of the sample, r_1 and r_2 denote the inner and outer radius of the coil, and l_1 and l_2 denote the distance between the bottom or the top of the coil and the sample), with brief view of primary and induced eddy current and secondary field. 54
Figure 3.2 Impedance plane for ferromagnetic and non-ferromagnetic materials [76]. 55
Figure 3.3 Diagrams of Dodd and Deeds' solution: (a) a rectangular cross-section coil above a half-space planar with a conductive coating; (b) a rectangular cross-section coil encircling a two-conductor cylinder with infinite longitude. The diagrams are in cylindrical coordinate system. The red rectangular represents the coil cross-section..... 58
Figure 3.4 The diagram of the co-axial sensor..... 60
Figure 3.5 Approximation of the Bessel term with a sinusoid..... 63
Figure 3.6 Top view of non-axial sensor 68
Figure 4.1 The configuration of sensors: (a) with co-axial coils; (b) with non-axial coils. 72
Figure 4.2 (a) and (b) are the models of sensors built in ANSYS Maxwell; (c) and (d) illustrate the mesh condition for numerical solution. 74
Figure 4.3 The eddy current on the surface of aluminium plate from the top view for two models at frequencies of 1 kHz, 10 kHz and 100 kHz..... 75

Figure 4.4 The pictures of practical models; (a) traditional open T-R sensor, and (b) cup-ferrite enclosed T-R sensor. 76
Figure 4.5 The picture of inner structure of the cup-ferrite T-R sensor, showing the exciting and pickup coils, cup-ferrite, and Ethernet socket for connections with instrument. 77
Figure 4.6 The picture of the custom designed EM inspection instrument. .. 78
Figure 4.9 The FEM models for traditional T-R sensor and cup-ferrite T-R sensor in ANSYS Maxwell; The sensors are above a ferrite plate. 79
Figure 4.10 Mutual inductance of (a) Cup-ferrite sensor and (b) traditional T-R sensor. The figures illustrate the mutual inductance changes with lift-off and frequency. 80
Figure 4.11 Mutual inductance of the T-R sensor and cup-ferrite sensor in the air measured by the Impedance Analyser (SI1260) with frequency sweeping from 10 – 10^7 Hz 81
Figure 4.12 The picture of sensitive resolution setup, with T-R sensor and ferrite rod under tested. 82
Figure 4.13 The spatial resolution curves of T-R sensor of different lift-offs with respect to 0.75 mm ferrite rod. Y-axis is the imaginary part of induced voltage with normalisation by subtracting the induced voltage in the air. The measurements were acquired by a custom-designed instrument under 40 kHz. 82
Figure 4.14 The spatial resolution curves of cup-ferrite sensor of different lift-offs with respect to the ferrite rod. Y-axis is the imaginary part of induced voltage with normalisation by subtracting the induced voltage in the air. The

measurements were acquired by a custom-designed instrument under 40 kHz. 83
Figure 4.15 Analytical and experimental data of given samples inductance variance with respect to brass sample (conductivity of brass sample is 15.9 MS/m). 86
Figure 4.16 Analytical data of 40% σ_0, 100% σ_0, and 160% σ_0 inductance variance with respect to brass sample 87
Figure 4.17 Analytical data of 80% σ_0, 100% σ_0, and 120% σ_0 inductance variance with respect to brass sample 87
Figure 4.18 Analytical results of given samples inductance variance with respect to brass sample under different excitation frequencies (a) 80 kHz (b) 90 kHz (c) 100 kHz. 90
Figure 4.19 Analytical results of given samples inductance variance with respect to brass sample under different plate thickness (a) 0.5 mm (b) 5 mm (c) 10 mm. 92
Figure 4.20 Magnitude of vector potential in x – z plane. 94
Figure 5.1 (a) Schematic of SAW thick plate with finishing and backing bead contour. The steel dimensions are 26.8 mm × 200 mm × 1 m; (b) picture of the weld cross-section sample extracted from the SAW API X70 steel as illustrated in (a). The specimen dimensions are 49 mm traverse (X-axis), 9 mm longitude (Z-axis), and 26.8 mm height (Y-axis). 100
Figure 5.2 (a) The macrograph of the weld cross-section, dotted lines indicate the weld metal boundaries; (b) the hardness map of the sample; black crosses indicate hardness measurement point locations; and the squares indicate the location of micrographs in Figure 5.3. 101

Figure 5.3 Micrographs of weld metal (left) and HAZ (right) of the weld (adapted from [100]). The locations from which the micrographs were taken are indicated in Figure 5.2. 102
Figure 5.4 (a) The picture of setup of experimental system with EM instrument, scanning stage, host PC, stage driver system, EM probe and tested specimen; (b) the diagram of scanning, shows the sensor arrangement, scanning path and sensor starting and ending position. 104
Figure 5.5 EM images of the weld specimen with 40 kHz excitation frequency, and circumstance of 0.5 mm lift-off (a) and (b) are EM images with the air boundaries when the sensor is out of the specimen; (c) and (d) are EM images of the specimen extracted from (a) and (b), also with calibration applied; X-axis and Y-axis display the width and height of the scanning; (a), (c) and (b), (d) exhibit the images of real parts and imaginary parts respectively. The contour of the weld specimen is clearly defined, and the estimated dimensions are 49.36 mm × 26.5 mm for 0.5 mm lift-off. 107
Figure 5.6 The correlation between EM signals and hardness at same locations, which are picked randomly in BM, WN, FZ and HAZ. 107
Figure 5.7 (a) Real part and (b) imaginary part of complex inductance, tested on the X70 sample with 1 mm lift-off. 112
Figure 5.8 Images of the weld cross-section, reconstructed by offset-crossing frequency with Re(ΔL) offset from 1.2×10^{-5} to 1.9×10^{-5}. 113
Figure 5.9 Images of the X70 cross-section sample reconstructed by (a) offset-crossing frequency, the dotted lines indicate the boundary of weld metal and HAZ; and (b) hardness map (Same as Figure 5.2 (b)). 114

Figure 5.10 Correlation of zero-crossing frequency and hardness data at a position of 4 mm away from the top of the image..... 114

LIST OF TABLES

Table 4-1 Parameters of sensor..... 73

Table 4-2 The spatial resolution of T-R sensor and Cup-ferrite sensor..... 83

Table 4-3 Inductance variance of samples with different conductivity under the Conductivity Invariance Lift-off..... 88

Table 4-4 A comparison of given samples permeability calculated by both Conductivity Invariance Lift-off and its neighbours..... 96

Table 5-1 SAW input parameters and weld dimensions. 100

ABSTRACT

Weld inspection is significant in manufacturing to improve productivity and ensure safety. During the welding process, steel microstructures experience complex transformations depending on welding conditions. Examining weld microstructures can reveal valuable information on its metallurgical, mechanical and electromagnetic properties.

In this research, a novel weld imaging method has been proposed based on EM testing. The newly designed electromagnetic (EM) sensor has a feature that at certain lift-off, the effect of a sample's conductivity on the sensor's response is reduced. Hence, the permeability can be estimated in a reasonable accuracy without the influence of its conductivity for dual phase steels. This sensor design enables better spatial resolution for weld imaging with reduced lift-off effect. A cross-section of an X70 steel submerged arc welding (SAW) sample has been imaged using impedance and a novel frequency feature in multi-frequency EM testing. It is derived that this frequency feature is closely related to the permeability of the sample. Therefore, the imaging results obtained from this feature reflects better permeability map of the sample. These images show good correlation with the hardness testing and metallurgical information of the weld sample. An approximate linear relationship was found between the EM signal and the hardness of the weld. The novel method significantly reduces scanning time with respect to hardness test and requires less surface preparation. And the operation frequency range can be adjusted to suit a particular instrument capability.

DECLARATION

What portion of the work referred to in the thesis has been submitted in support of an application for another degree or qualification of this or any other university or other institute of learning. This should include reference to joint authorship of published materials which might have been included in a thesis submitted by another student to this university or any other university or other institute of learning.

COPYRIGHT STATEMENT

i. The author of this thesis (including any appendices and/or schedules to this thesis) owns certain copyright or related rights in it (the “Copyright”) and s/he has given The University of Manchester certain rights to use such Copyright, including for administrative purposes.

ii. Copies of this thesis, either in full or in extracts and whether in hard or electronic copy, may be made only in accordance with the Copyright, Designs and Patents Act 1988 (as amended) and regulations issued under it or, where appropriate, in accordance with licensing agreements which the University has from time to time. This page must form part of any such copies made.

iii. The ownership of certain Copyright, patents, designs, trademarks and other intellectual property (the “Intellectual Property”) and any reproductions of copyright works in the thesis, for example graphs and tables (“Reproductions”), which may be described in this thesis, may not be owned by the author and may be owned by third parties. Such Intellectual Property and Reproductions cannot and must not be made available for use without the prior written permission of the owner(s) of the relevant Intellectual Property and/or Reproductions.

iv. Further information on the conditions under which disclosure, publication and commercialisation of this thesis, the Copyright and any Intellectual Property and/or Reproductions described in it may take place is available in the University IP Policy (see http://documents.manchester.ac.uk/DocuInfo.aspx?DocID=24420) in any relevant Thesis restriction declarations deposited in the University Library, The University Library’s regulations (see http://www.library.manchester.ac.uk/about/regulations/) and in The University’s policy on Presentation of Theses.

ACKNOWNLEDGEMENT

The past four years have been an extraordinary period of my life. I would like to express my sincere appreciation to those who supported and guided me throughout my Ph.D. research. I wish you all have a wonderful and meaningful life.

I would like to thank my supervisor, Dr Wuliang Yin, whose expertise was invaluable in the formulating of the research topic. He is not only an excellent supervisor who guides me in academic direction, but also an elder and friend who guides me in the direction of my life. I would like to thank him again for his patience, support and constant care.

I would like to thank my colleagues and friends for their company and support. Thanks to Dr Yuedong Xie, Dr Peipei Hu, Dr Wenbin Tian, Dr Wenqian Zhu, Dr Mingyang Lu and Mr Jorge Salas Avila, who have helped me a lot in researching area. They selflessly shared their acknowledge with me and supported me in experiments and simulations.

Finally, I want to thank my beloved wife, Yuge Wang, for her devotion and dedication to me and for giving me courage and motivation when I am depressed. Thanks for holding me together all the time. I want to thank my parents, Mr Guangru Xu, Mrs Zhenxiang Chen, and Mr Xinglong Wang, Mrs Ping Ji. They love and support me with all hearts and taught me to be a man. The gratitude can not be expressed with any words.

THE AUTHOR

The author received his B.Eng. (2013) and M.Sc. (2014) in electrical and electronic engineering from the University of Manchester. He is currently pursuing his Ph.D. in sensing and imaging. He is a reviewer for IEEE Transactions on Industrial Informatics, International Journal of Pressure Vessels and Piping and IEEE Access, etc. His research mainly involves non-destructive testing based on electromagnetic method. His research interests include the material characterisation, conductivity and permeability measurements, weld inspection, imaging and signal processing.

PUBLICATIONS BY THE AUTHOR

Journal Papers (* indicates communication author**):**

J1 **Xu, H**., J. R. Salas Avila, F. Wu, M. J. Roy, Y. Xie, F. Zhou, A. Peyton and W. Yin (2018). "Imaging x70 weld cross-section using electromagnetic testing." NDT & E International **98**: 155-160.

J2 Lu, M., **H. Xu**, W. Zhu, L. Yin, Q. Zhao, A. Peyton and W. Yin (2018). "Conductivity Lift-off Invariance and measurement of permeability for ferrite metallic plates." NDT & E International **95**: 36-44.

J3 Yin, L., B. Ye, Z. Zhang, Y. Tao, **H. Xu**, J. R. Salas Avila and W. Yin (2019). "A novel feature extraction method of eddy current testing for defect detection based on machine learning." NDT & E International, Accepted/In press.

J4 Yin, W., J. Tang, M. Lu, **H. Xu**, R. Huang, Q. Zhao, Z. Zhang, and A. Peyton (2019). "An Equivalent-Effect Phenomenon in Eddy Current Non-Destructive Testing of Thin Structures." IEEE Access 7: 70296-70307.

J5 Zhao, Q., Z. Kai, S. Zhu, **H. Xu**, D. Cao, L. Zhao, R. Zhang, and W. Yin (2019). "Review on the Electrical Resistance/Conductivity of Carbon Fiber Reinforced Polymer." Applied Sciences **9**(11): 2390.

J6 **Xu, H.**, M. Lu, J. R. Salas Avila, Q. Zhao, F. Zhou, X. Meng, and W. Yin (2019). "Imaging Weld Cross-Section Using a Novel Frequency Feature in Multi-Frequency Eddy Current Testing." Insight-Non-Destructive Testing and Condition Monitoring, 61(12), 738-743.

J7 Xie, Y., M. Lu, W. Yin, **H. Xu***, S. Zhu, J. Tang, ... & Z. Qu (2019). "Novel Wearable Sensors for Biomechanical Movement Monitoring Based on Electromagnetic Sensing Techniques." IEEE Sensors Journal, 20(2), 1019-1027.

Conference Papers:

C1 **Xu, H.**, Z. Cui, A. Peyton, M. J. Roy and W. Yin (2016), "Imaging Weld Cross-Section Using Eddy Current Testing." *in 21st International Workshop on Electromagnetic Nondestructive Evaluation 2016 (ENDE)*.

C2 Avila, J. R. S., Z. Chen, **H. Xu** and W. Yin (2018). "A multi-frequency NDT system for imaging and detection of cracks." *2018 IEEE International Symposium on Circuits and Systems (ISCAS).*

Chapter 1 Introduction

1.1 Motivation

Welding is one of the most common fabrication techniques within manufacturing today in a variety of industries, such as automotive, aviation, aerospace, and nuclear energy, etc. It is widely used to join two or more metals. For example in pipeline manufacturing, steel strips are rolled into circular section or in continuous spiral manner and the seam can be welded as shown in Figure 1.1. The pipeline quality relies significantly on welding quality. Based on the pipeline product loss incidents and faults report from UKOPA reported in March 2019, the product loss caused by faulty weld amounts for 19.8% among all causes, involving main UK collaborative natural gas pipeline up to the end of 2017 [1].

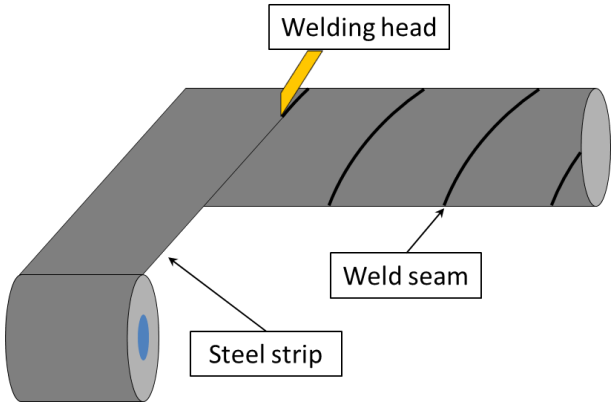

Figure 1.1 Spiral seam welding pipeline manufacturing

Based on the data shown in Figure 1.2, external corrosion, external interference, and weld seam defect can cause high volume of product loss. The failure frequency and severity attributing to external interference varies in diameter, wall thickness of the pipeline and the area. Small diameter and wall thickness pipelines are the primary objects of this cause. Besides failure

frequency is much higher in urban cities than rural area due to more human activities. In other industries, such as train, aerospace, and nuclear energy, an incident caused by weld failure could endanger thousands of lives. During the product lifetime, welding joints are more likely to suffer external pressure, corrosion and fatigue. It is vitally important to examine the welding quality and perform continuous inspection on the welds during their service life to avert severe economy loss, environmental damage and people injury.

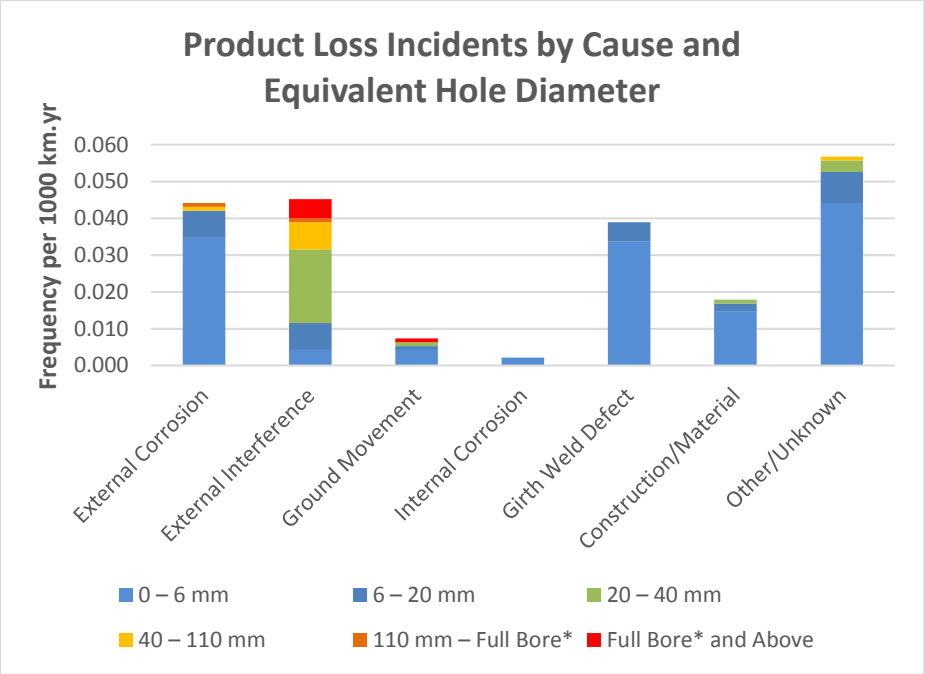

Construction/Material = Seam Weld Defect + Pipe Defect + Pipe Mill Defect + Damage during Original Construction

* Full Bore ≡ diameter of pipeline

Figure 1.2 Product loss incident frequency by causes and size of leak in the period 1962 to 2017 cited from [1].

Welding quality examining methods have experienced fast development since 1960s [2] [3] [4]. Traditionally, destructive testing methods such as tension test, bend test, Charpy test and hardness test, are used to evaluate the weld quality,

to characterise material's mechanical properties, like tensile strengths, ductility, impact toughness, and hardness. It is known that the mechanical properties of welds can be affected by the microstructural changes during the welding process and post-weld heat treatment [5] [6] [7] [8] [9].

Methods such as magnetic particle inspection (MPI) are used for surface and shallow subsurface imperfections detection for ferromagnetic materials. Other non-destructive testing (NDT) methods such as radiographic and ultrasonic testing are commonly in use for detection of crack, defect and porosity. Electromagnetic (EM) method such as eddy current testing (ECT) can be used for flaw detection for welding [10] [11]. However, there are currently few NDT methods which are used for material characterisation, particularly for weld macrograph and micrograph.

The relationship between EM properties and microstructure is worth investigating. EM methods can be implemented for both conductive and ferromagnetic materials, which are suitable for most welding materials. As a consequence, EM methods have potential for microstructure characterisation of weld, taking the advantages of being cheap, rapid, no radiative hazard and the non-contacting nature with the test sample.

1.2 Aim and Objectives

The aim of the research is to develop a weld inspection method based on the EM inspection principle for material characterisation and defect detection. The goal is to acquire the EM properties of a weld sample and construct a mapping image that can be related to the microstructure, hence the mechanical

properties of the sample; in addition, to explore the possibility of using the method for online welding testing.

The specific objectives are:

i. Investigate the parameters that affect the performance of an EM sensor, such as coil arrangements, the number of turns, dimensions, the distance between the coil(s) and the test sample, dimension of samples and operation frequency through testing of a traditional EM sensor on different materials. This helps to develop further understanding of EM NDT technology.

ii. Design a novel EM weld imaging system through integrating an EM measurement instrument (Impedance Analyser), an EM sensor and a scanning stage. The EM instrument used can be a commercial Impedance Analyser (SI1260), or a custom designed EM instrument in our laboratory. The focus is to integrate the system and test the imaging method.

iii. Map the surface of a weld cross-section using the EM imaging system and compare the images with micro-hardness measurements and the metallograph of the test sample.

iv. Improve EM sensor to achieve a better spatial resolution without losing sensitivity and fast imaging speed.

v. Explore the applicability of the imaging system in a real-time online welding scenario. Test its immunity to electromagnetic interference (EMI) caused by the large current and voltage for arc generation during welding.

1.3 Contributions

The thesis has contributed in several novel aspects in electromagnetic testing for welding inspection.

i. Designed a novel cup-ferrite enclosed T-R sensor consisting of a pair of non-axial excitation, pickup coils and a ferrite cup. This design enables that the eddy current is mainly restricted to the area between the excitation and pickup coils and immune to external interference. Therefore, the sensor enables better spatial resolution for weld imaging with reduced lift-off effect.

ii. Discovered a novel conductivity invariance phenomenon (CIP) of the designed non-axial sensor. The non-axial sensor has a feature that at certain lift-off, the effect of a sample's conductivity on the sensor's response is reduced. Based on this phenomenon, a novel permeability measurement approach is proposed. The proposed approach was verified by both simulation and experimental data. And the permeability can be estimated in a reasonable accuracy (with an error of 2.86 %) by the proposed approach without the influence of its conductivity.

iii. Proposed a new method for imaging the cross-section of a weld based on EM testing. Experiments indicate that the obtained EM image shows clearly different weld zones for a high strength pipeline steel weld cross-section. And the EM image is compared to the hardness map of the weld cross-section with a high correlation coefficient (R=0.9479). The novel method significantly reduces scanning time with respect to hardness test and requires less surface preparation.

iv. Proposed an imaging method using a novel frequency feature (the frequency at which the real part of the inductance reaches a specified value) in multi-frequency EM testing. It is derived that this frequency feature is closely related to the permeability of the sample. Therefore, the imaging results obtained from this feature reflects better permeability map of the sample. The obtained images are then compared with the weld macrograph and hardness map. The shape and contour of three weld zones (FZ, HAZ, and BM) can be identified. This novel imaging method has a high sensitivity to microstructure changes and by adjusting the inductance value it crosses; the frequency range can be adjusted to suit a particular instrument capability.

1.4 Thesis Outline

This chapter has introduced the motivation, aim and objectives of this research, contributions of the thesis and the thesis outline.

Chapter 2 introduces the related background of welding process and the microstructure transformation of weld. The chapter reviews current research efforts on welding inspection. In addition, this chapter also describes the salient aspects of existing welding inspection technologies.

Chapter 3 describes the supporting EM theory of inductive sensor including basic Maxwell's equations, and eddy current, impedance and skin depth. The chapter also presents a classic analytical solution proposed by Dodd and Deeds for a coil above a planar. The solution has been expanded to co-axial

and non-axial sensor structure, describing the calculation of impedance changes of sensor due to test sample.

Chapter 4 describes the main parameters in sensor design. This chapter also introduces the novel designed sensor, and its performance characterisation, including sensitivity, spatial resolution, and lift-off effect. In addition, the chapter investigates a novel finding (conductivity invariance phenomenon) of the sensor. Permeability measurement method is introduced per the conductivity invariance phenomenon.

Chapter 5 demonstrates the imaging results of a weld sample applying the designed EM welding imaging system. This chapter provides the metallographic information of weld sample, including macrograph, and hardness mapping of the sample. The obtained EM images are mapped using the impedance and a frequency feature of the proposed method. The EM images are then compared with the hardness mapping.

Chapter 6 concludes the work accomplished in this research and proposes potential future work.

Chapter 2 Background

Welding is a process of joining materials, usually metals, which is widely used in industries, in areas such as automotive, aviation, aerospace, and nuclear energy, where welding qualities dominate the successful implementation of industries and safety of personnel involved. Hence, it is essential to ensure quality meanwhile keeping high productivity in manufacturing industry. For the welding, due to some likely inexperienced manipulations, the risk of failure as with incomplete penetration, defects, and flaws gives rise to the development of welding inspection.

This chapter introduces the background of welding process and microstructure. It helps to understand the basic of weld and their exhibition performance. An overview of welding inspection techniques is included in this chapter. The EM testing is introduced on emphasis.

2.1 Welding Process and Microstructure

Welding process has been known in human history for thousands of years as forge welding. However, modern welding principles emerged at the end of 19th century [12]. Generally welding technologies are classified into pressure welding and fusion welding. The definition and terms of welding are given in ISO/TR 25901. These welding methods all include a heat source that can soften or melt the material that joining two parts together. Figure 2.1 shows the zones and their names of a welding joint. The metallurgy of weld joint can be categorised into zones that includes weld metal or nugget (WN), penetration zone or fusion zone (FZ), heat affected zone (HAZ) and base metal (BM).

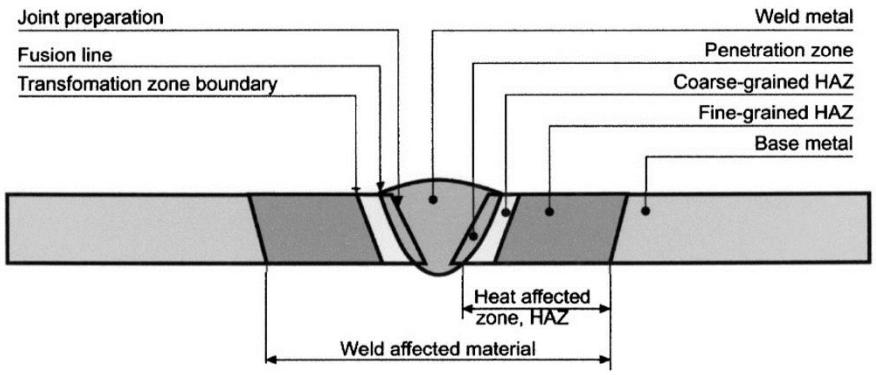

Figure 2.1 Nomenclature of zones and boundaries for a weld joint [13]

The material microstructure experiences complex transformation during the welding process [14] [15] [16] [17]. A material's performance is intrinsically determined by its microstructures. Consequently, it is essential understand the microstructure changes during welding in industry in order to improve the performance.

2.1.1 Pressure Welding

The pressure welding uses extra force to press two parts together through plastic deformation [18]. The facing surfaces of two parts are usually heated to enable the bonding. With different heat input sources, main pressure welding technology includes resistance welding and friction welding.

2.1.1.1 Resistance Welding

Resistance welding uses the passage of high current to melt the metal. The current is usually very high, in the range of 1 000-100 000 A [18]. Well-known resistance welding method such as spot weld, seam weld, projection weld, butt weld and flash weld are generally used for welding metal sheet and end of rods, wires to surfaces.

The substance of resistance welding is to control the thermal energy that melt the joining surfaces. The thermal energy is varying by the resistance of weld material, electrode, external force, electric current and time duration. Thanks to the large electric current, large thermal energy can be delivered to the weld area in a short duration. Consequently, less remainder of the workpiece is affected by excessive thermal.

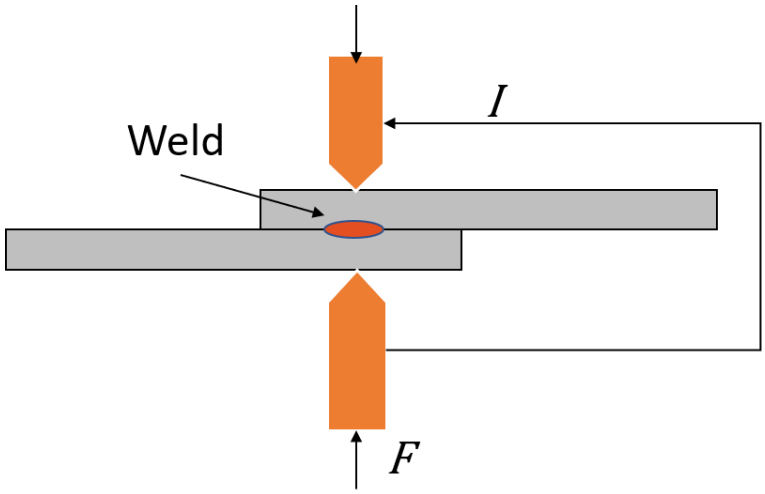

Figure 2.2 Schematic of resistance spot welding.

The schematic of spot welding is shown in Figure 2.2. Spot weld is largely used in industry. An ordinary private car can have up to 5000 spot-welded joints [19]. The advantages of the method are fast, efficiency, low-polluting and usually no filler material is required. But the method has limited range of applications and large variations in weld quality. The challenge in modern industry is to develop a real-time inspection to improve the production while ensuring the weld quality [20].

2.1.1.2 Friction Welding

Another well-known pressure welding method is friction welding. Two parts of workpieces are pressed against each other and welded through plastic

deformation by simultaneous heat input from mechanical rotation. The method is usually used for two rotationally symmetrical bodies, e.g. bar to bar, pipe to pipe, flanges or endpieces [18]. The performance of the welding is determined by the rotation speed, time that the workpiece is rotated and the applied pressure. The friction welding uses pure mechanical heat input and has been serving industry for more than 30 years. Usually materials at two ends are pressed out and formed as a collar to the joint. Hence, the welding joint can be homogenous and not degraded by any contamination on the welding surfaces. This welding technology has developed in recent years. It can have more applications.

2.1.1.3 Friction Stir Welding

Friction stir welding (FSW) is an upgraded friction method that an external rotation tool is penetrated in the workpiece. FSW is particularly suitable for welding aluminium and its alloy [18].

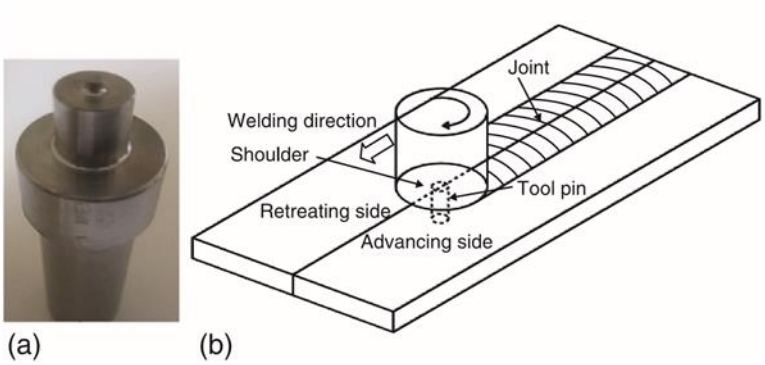

Figure 2.3 (a) A FSW tool; and (b) Schematic of FSW process [21]

The FSW process and tool is illustrated in Figure 2.3. The friction of the rotating tool pin and shoulder against the workpiece generates heat that softens the material and enables the two parts to be joined [21]. The material around the pin experiences plastic deformation and flows from the front of the tool to the

trailing edges of joint. Meanwhile the shoulder of the tool prevents the material displaced upwards. The resultant welding seam is very smooth and at the same level of original surface. The main advantages of the method are smooth and reproducible joint; little thermal stress or distortion; and good mechanical properties preservation. The drawbacks can be that a hole will be left at the end by the tool. In addition, due to its low thermal energy, the weld speed can be slow for hard materials.

2.1.2 Fusion Welding

Fusion welding represents the welding processes where the material is molten and solidified to join two parts. A molten pool is necessary for fusion welding based on the definition. The heat input could be various, such as gas flame, arc, laser, and electron beam [12]. Gas welding process is a cheap and versatile manual process for repair and maintenance work at 1900s [22]. The heat is generated by the combustion of fuel gases in oxygen, among which acetylene provides the hottest flame. But the heat is still less concentrated and has lower temperature comparing to the electrical arc [23]. It is a lot less used today. Arc welding process takes great share of all fusion welding processes. There were already at least 35 divisions back in late 1900s [24].

2.1.2.1 Arc Welding

An electric arc is an electrical breakdown of gas that produces plasma where plasma arc contains extremely high temperature. Electrodes are essential for generating arc. For welding usage, one of the electrodes is the conducting workpiece while the other pole of the arc is usually a rod known as electrode. A molten pool is formed at the surface of workpiece where with a high welding current [25]. After World War I, several grades of electrodes were developed,

including tungsten, low carbon steel, high carbon steel electrodes and copper alloy rods to accommodate different applications. Since the diffusion of oxygen and nitrogen in the molten weld metal resulted in brittle and sometimes porous welds, the weld zone can be protected by gas or flux [21]. In 1930s submerged arc welding (SAW) succeeded the automation process of welding where a continuous wire is fed and the arc is submerged by granular fusible flux [12].

2.1.2.2 Submerged Arc Welding

The schematic of SAW is illustrated in Figure 2.4. The flux closest to the arc melts and forms slag on the surface of the weld, thus protecting the molten metal from reacting with the oxygen and nitrogen in the air. The slag also usually comes away by itself [26]. Residual powder is sucked up, returned to the flux hopper and re-used. The welding is affected by the following parameters: arc current, arc voltage, filler wire material and dimensions, filler wire angle, welding speed, and flux types (acid / neutral / basic), etc. These parameters have dominating effects on the weld appearance and mechanical performance.

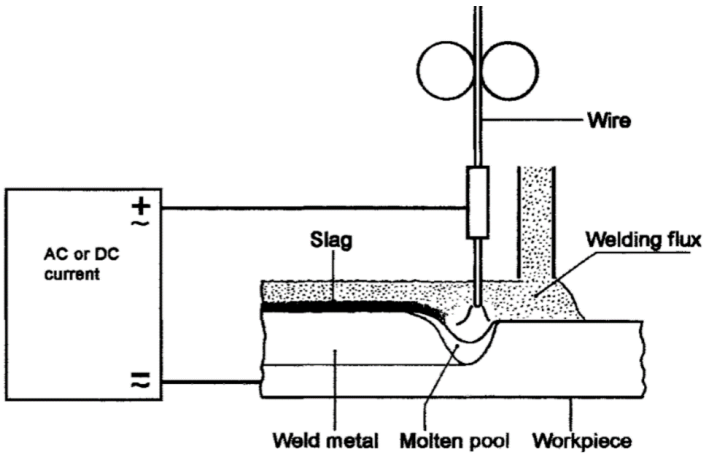

Figure 2.4 Schematic of SAW [26].

For example, the welding speed affects the penetration and the width of the weld bead. A high speed welding produces narrow weld cross-section, but shallow penetration as demonstrated in Figure 2.5.

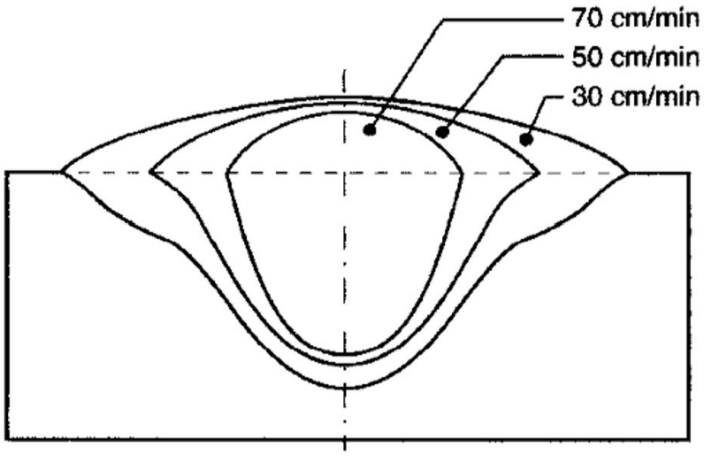

Figure 2.5 The demonstration of the effect of welding speed on weld appearance and penetration (Cross-section area of the weld) [26].

The wire angle has similar effects on the weld appearance and penetration as illustrated in Figure 2.6. Backhand produces a narrow and deep penetration weld bead.

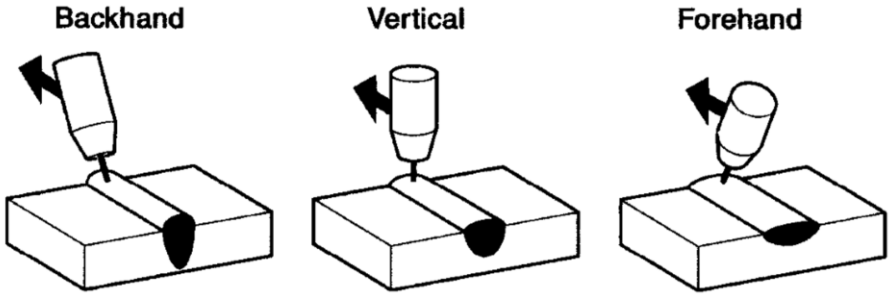

Figure 2.6 The demonstration of the effect of filler angle on weld appearance and penetration [26].

With a combination of choices of weld parameter, the weld appearance and its performance can be designed. If the welding parameters are properly set, the appearance of the weld is often very uniform and bright, merging smoothly into the workpiece material. SAW is mainly applied for large items in industry,

like longitudinal tubes and large diameter vessels. It takes the advantages of high productivity and quality.

2.1.2.3 Other Fusion Welding

High density laser and electron beams are usually used to produce deep, narrow penetration. One of the main application areas for laser welding is the automotive industry, which welds relatively thin sheet [27]. Because of small area of heating, the methods provide a smaller HAZ and fewer distortions than conventional methods. The welding speed is also very fast. The methods also require more highly accurate jigs and fixtures because the diameter of the beams is minor.

2.1.3 Microstructure of Weld

A weld usually composites different metallic alloys. They all represent different structure if viewing in micro-scale. The microstructure is specified by number of phases, their proportion and space arrangements in metallographic. Since the research of thesis focuses on weld of steels, the microstructure of steel is studied.

2.1.3.1 Pure Iron Allotropes

Pure iron is simplest form to study. Three crystal structure of iron can occur naturally including body-centred cubic (bcc, α, ferrite), face-centred cubic (fcc, γ, austenite) and hexagonal close-packed (hcp, ε) [28]. Figure 2.7 illustrates the pure iron phase with relationship of pressure and temperature. Each point on any boundary between the phase fields represents an equilibrium state in which two phases can coexist.

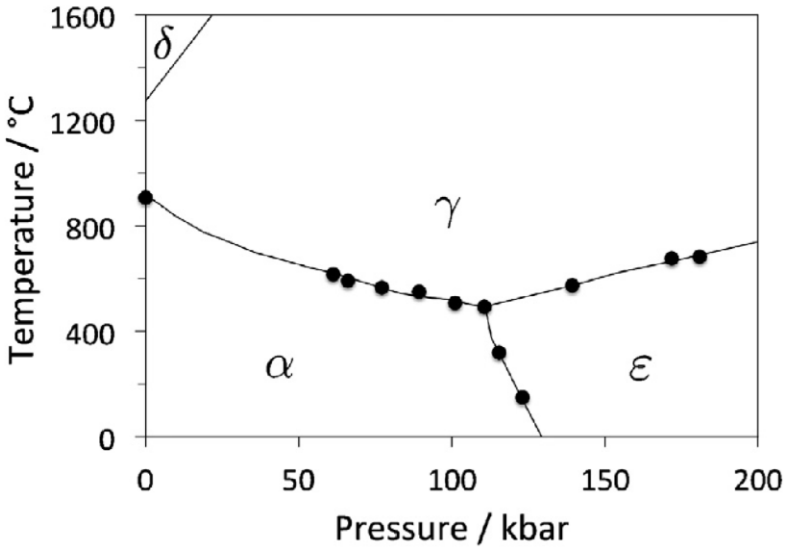

Figure 2.7 The phase diagram for pure iron [28]. The triple point temperature and pressure are 490℃ and 110 kbar, respectively. α, γ and ε refer to ferrite, austenite and ε-iron, respectively. δ is simply the higher temperature designation of α.

2.1.3.2 Phase Transformation of Austenite and Ferrite

Figure 2.8 illustrates the phase change of pure iron dependence of temperature. At ambient pressure, α-Fe will transform to γ-Fe, when temperature increases to 910 ℃. When temperature reaches at 1390 ℃, α-Fe reverts to δ-Fe which has the same crystal structure as α-Fe. The δ-Fe remains the stable phase until melting occurs at 1536 ℃ [28]. The volume per atom of α-Fe is smaller than γ-Fe. The volume and relevant loose structure of bcc, α-Fe results in different in plastic deformation and diffusion of elements such as carbon comparing to fcc, γ-Fe. Most steels contain modest concentration of alloying elements. Thus, they have similar phase transformation as pure iron.

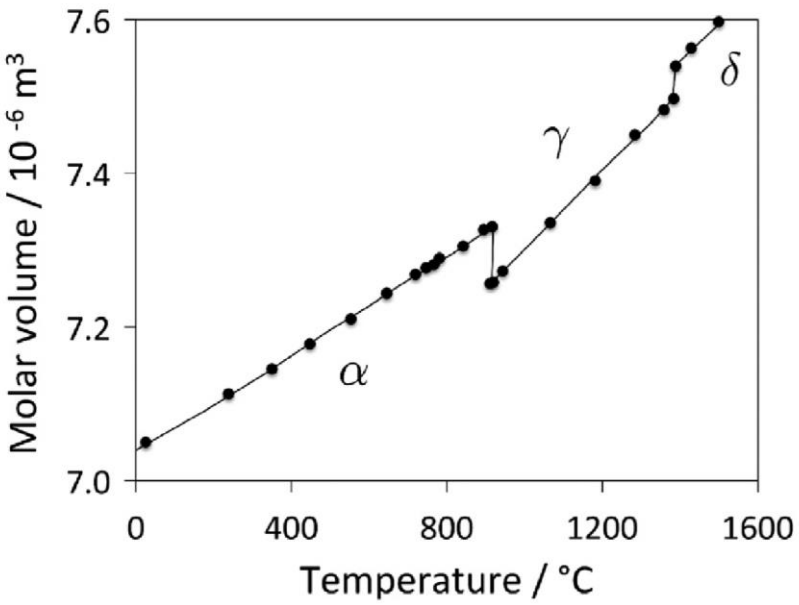

Figure 2.8 Mean volume per atom in iron crystals with dependence on temperature [28].

2.1.3.3 Phase Transformation in Weld

In a fusion welding process, the steel melts and solidifies in the FZ where a solidification microstructure forms. In addition, the HAZ microstructure also experiences a heating and cooling cycle, affected by the heat diffused from the FZ.

In FZ, the primary microstructure major components are allotriomorphic ferrite (α_a), Widmanstätten ferrite (α_w), and acicular ferrite [29]. Figure 2.9 illustrates the primary microstructure of a steel weld deposit, showing the components and their distribution. The mechanical property of weld FZ normally drops below the BM. Acicular ferrite is a desired microstructure as it improves especially the toughness [30]. An increase of oxide inclusions benefits the formation of acicular ferrite.

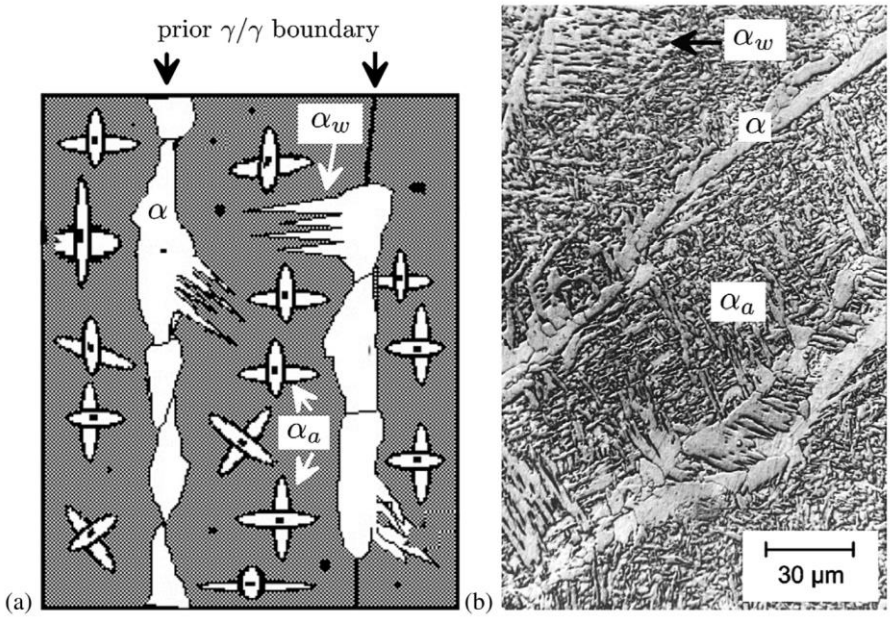

Figure 2.9 (a) Schematic of the essential constituents of the microstructure in the columnar austenite grains of a steel weld deposit.(b) Scanning electron micrograph of the microstructure of a steel weld [29].

In HAZ, the heat changes as a function of the distance to the FZ boundary. The heating rate reduces as the distance increases. However, the cooling rate is less sensitive to the distance. Figure 2.10 illustrates the expected microstructure in HAZ of steel welds. At the rightest side, the FZ has columnar grains. To the left, the HAZ is fully austenitic, and forms coarse austenite structure as the it experiences annealing under heating high than 1200 ℃. Further to the left, the grain size decreases with the zone of fine austenite. Besides, the coarse austenite has increased ductility and reduced hardness compared to fine austenite. With further distance to the FZ boundary, the HAZ is only partially austenitic.

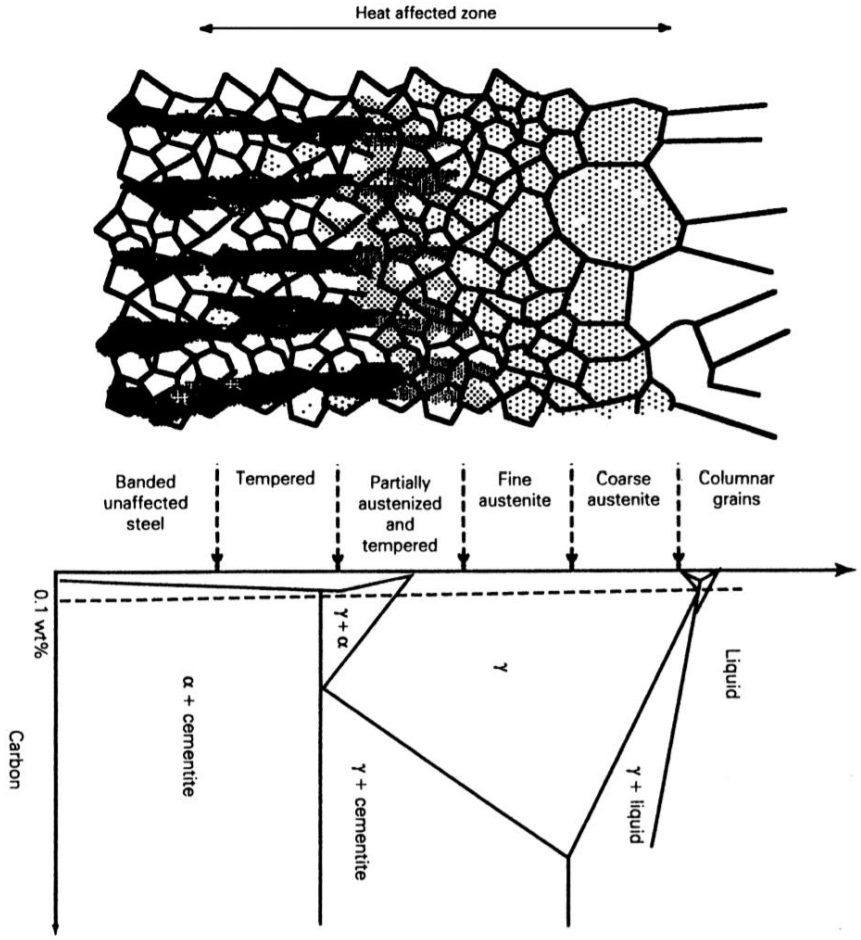

Figure 2.10 Schematic of possible microstructural variation in the HAZ of steel welds [29].

Depends on the welding process, parameters and base materials, the microstructure transformation is very complexing. In practice, there is usually more than one phase in an area. Consequently, the weld results in different mechanical properties.

2.2 Welding Inspection Method

Weld inspection is a significant process. It makes sure the weld joint meets the desired mechanical, metallurgical, and physical properties that required by a standard such as API 1104, which is a common standard used throughout the world for pipeline construction [31]. Besides, there are standards for examination of weld such as EN1206, EN970, etc. Weld inspection methods

can be divided into two categories, including vision, radiographic, ultrasonic, and magnetic testing in non-destructive manner, and destructive methods such like hardness testing, Charpy testing and tension testing for directly mechanical properties measurement.

Three main methods are briefly reviewed above, among which there are still many subsets. Besides, methods such as acoustic emission, active thermography, liquid penetrant, and microwave inspection were described in [32], and so as optical methods. There are usually some combinations of these NDT methods to provide a better result. To sum up, ECT methods has been proved to be a sufficient, rapid, and relatively low cost technique for weld inspection.

2.2.1 Destructive

2.2.1.1 Hardness Testing

Hardness is defined as the resistance to indentation on surface of a material. In response to different welding protocols, hardness testing is a very useful tool to infer microstructural parameters and compare material processing histories and therefore validate welding quality. Vickers hardness testing is one of the most popular hardness tests. It uses a diamond shape impression into the material under a specified load (Micro-Vickers hardness test uses load less than 1 kgf). The unit of Vickers test is HV, calculated through the dimensions of the indentation.

In addition, many international structural integrity codes specify hardness testing as a quality control measurement, such as ISO15156-1 [33] and ASME BPVC Section IX [34], and there are international standards available which

cover the application of singular measurements (e.g. ISO 6507-1 and ASTM E384-10).

The practice of 'mapping' regions with hardness measurements for a weld is usually applied on the cross-section (thickness), since the welding results in apparent hardness reduction in the FZ and HAZ. Not only to measure the mechanical property, hardness test also allows one to identify specific metallographic regions in the case of weld. Most importantly, subtle changes in microstructure of HAZ might not be immediately apparent through standard optical microscopy [35] [36]. The disadvantages of the hardness test are:

- It requires surface preparation.
- It usually takes long operation time.
- The method is destructive, though the indentation can be small.

2.2.2 Non-destructive

The basic definition or the advantage of NDT is that it evaluates materials or products without impairing their performance in the future services [37]. Furthermore, during the service life, it is valuable to inspect fatigue cracks growth, so as to determine whether to replace production or to repair defective components.

2.2.2.1 Radiological Testing

Radiological testing (RT) has been developed for over a hundred of years, which becomes a mature method for welding inspection [4]. Figure 2.11 illustrates the principle of film radiography which employs radiation sources to generate X-rays or gamma-rays to penetrate a specimen. A film is usually placed in the opposite position with respect to the source as a detector. X-rays

or gamma-rays are assumed to travel in straight line from the source to the film passing through the specimen. Hence, an image is then displayed on the film after exposure and processing. The absorption coefficient of rays varies with material properties, and less attenuation occurs when the beams travel through a defect. Therefore, radiography is usually applied to test imperfections. The penetration of X-rays is up to 500 mm in steel which depends on the energy and wavelength of the radiation [32].

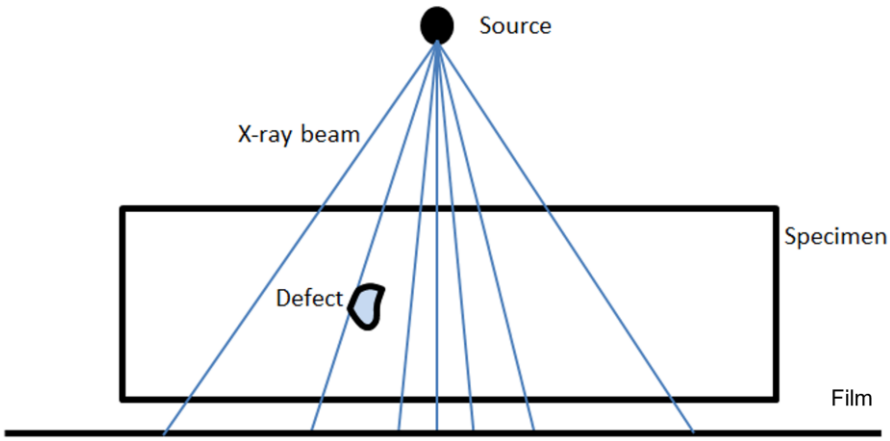

Figure 2.11 Schematic illustration of film radiography, defect is displayed on the film as a projection

The significant revolution of RT is the emergence of digital radiography (DR) and computed tomography (CT), where analogy film detector is replaced by a digital detector. The main improvement is that the film processing is discarded, and image sharpness and contrast can be enhanced. Consequently, it is faster and easier to accomplish a three-dimension image with projections from different angles [37].

An application for pipe welding is given in [37], where the radiation source is located at the cylindrical axis, and films are wrapped around the pipe. Due to the difficulty in analysing image, massive efforts were taken in image

processing to automatically extract defect information from the background information. In 1995, a weld extraction methodology was produced to improve the analysing of radiography by extracting useful information for flaw detection[38] [39]. G Wang and T Liao contributed to automatically distinguish different types of defects [40], and Liao keeps on improving the performance and accuracy [41].

RT can detect subsurface discontinuities and determine the density and thickness of any materials while there is a limitation for other NDT techniques [32]. However, the method is expensive and potentially hazardous. The main drawback is that it lacks the ability to detect closed cracks. It has difficulties in surface defect inspection with 2D (two-dimensional) radiography, and the detect orientation is significant to the results corresponding to the location and appearance of tested defect during implementation.

2.2.2.2 Ultrasonic Testing

Ultrasonic testing (UT) has been developing rapidly in the late 19th century. The brothers Curie and Lippmann discovered crystals that can convert ultrasonic energy and electrical energy either way [32], which enabled the developing of ultrasonic NDT. The UT was significantly improved for flaw testing in steel in 1940's with introduction of pulsed ultrasound. In 1960's, UT was widely employed in defect detection in metals and welds [42] [4]. It has become a desirable method in NDT compared with RT, as it performed great and robust without hazard. Figure 2.12 illustrates the basic principle of UT with two types of transducer [43] [44] [45]. The basic principle is relying on the propagation and attenuation of acoustic waves in media. The signal varies on

the received transducer depending on the physical and mechanical properties, and the presence of defects of the tested objects. The propagation velocity varies in different media, for example, one common form of ultrasonic waves has a velocity of $6 \times 10^3\ m/s$ in steel [37]. The ultrasonic waves reflect or scatter at any surface or discontinuity inside the test specimen, afterwards, the received signals together with a timer is computed to measure the distances, which represent the dimension, thickness, and location of defects. In practice, the waveforms are complicated, mainly longitudinal waves and transverse waves are considered in solid, while more complicated surface waves are introduced in [37], among which Rayleigh surface wave plays an important role in NDT.

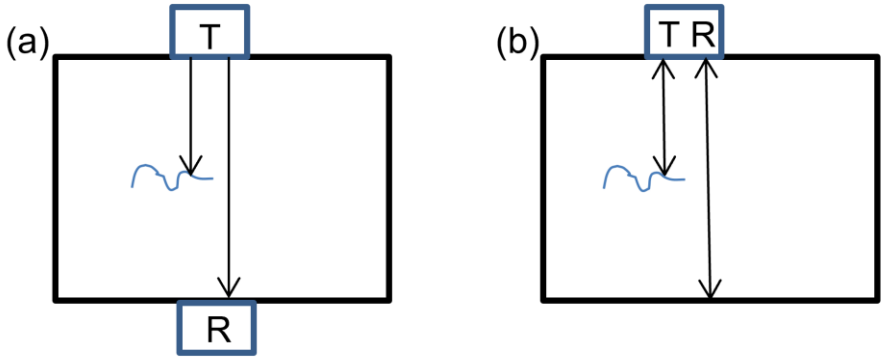

Figure 2.12 (a) Pitch-catch method with two transducers; (b) Pulse-echo method, transmitter, and receiver are the same transducer.

Different generations of ultrasonic waves enrich the application of differently designed transducers of which are mainly piezoelectric transducers, electromagnetic acoustic transducers (EMATs), and laser generated transducers. Despite EMATs and laser generated transducers support a lift-off to accomplish non-contacted NDT. Most of the widely used methods are contacted where gel or water is required as a scan couplant.

Recently, Gao et al. produced an EMAT generated system to inspect partially completed welds which achieved to implement a real-time inspection for surface and subsurface defects [46]. Laser/EMAT ultrasonic technique was used to inspect a hidden incomplete penetration in weld in the manner of C-scan image [47]. It takes around 2 hours to detect the weld of size 30 mm × 10.8 mm.

The advantages of UT are

- It can find linear defects in most orientations, and laminations.
- The method is safe and can be portable.

The disadvantages are

- It takes long time for imaging.
- The surface needs to be smooth and couplant is required.
- The receiving signal interpretation is complicated.

2.2.3 Electromagnetic Methods

In addition, EM methods have been developing fast in non-destructive testing. Magnetic particle method is well known in detecting cracks for ferromagnetic materials, such as iron, steels. In terms of electrical methods, potential drop method is one of the main methods [37]. However magnetic particle method and potential drop method requires contact. Before WWII, ECT was employed for simple sorting applications [32]. As early as 1879, Hughes used an induction coil to sort metals [48]. Eddy current is induced in conductive materials by closing a magnetic field, which generates a secondary magnetic field with opposite direction. More description for ECT is given in Chapter 3.

During the 1950s and 1960s, Forster introduced precise work both in theory, and practical instruments [49] [50], which granted frame for ECT and also accelerated the development of modern ECT. After decades, ECT was proved to be a sufficient method for metal characterisation and defect detection. And it has become a most commonly applied NDT technique. Dodd and Deeds introduced a modelling method for different arrangements between probe and specimen in 1968 [51] [52]. The method computed the surrounding magnetic fields. Subsequently, eddy current, coil impedance, flaw impedance, and mutual inductance are all computed.

ECT can characterise the composition, structure and mechanical properties of a specimen. Meanwhile, ECT is good at detecting surface and subsurface defects. However, this technique has some limitations in inspection of ferromagnetic materials, and accurate characterisation of discontinuities [53]. In order to improve the performance and overcome the drawbacks, massive efforts have been taken to improve the simulation method, and instrumentation method, such as multi-frequency, phased array, and automation progression [53]. The advantage of ECT is the relatively low expense and less time consuming without mention of its non-contact nature. On the other hand, ECT can only be applied to conductive materials. Furthermore, it lacks the ability to detect internal defects. The penetration of eddy current into materials is depending on the frequency, where low frequency is usually applied to detect subsurface defects. Considerable research of ECT has been carried out recently. The interests are mainly focused on the design of transducers, image processing, and the application of automation inspection. Some design of transducers were introduced in [54] [55]. In 2005, W Yin et al introduced a

method to imaging the continuous conductivity profile of a metal using a multi-frequency sensor [56]. And an imaging method with probe arrays was produced by Mook G et al [57]. They achieved to visualize defects in aluminium blocks and sheets. And they approached to read 7 mm font engraving clearly which had a good resolution. There are many researchers working on the detection and imaging of defects using ECT [58] [59] [60] [61]. The eddy current method has been proved to provide a robust performance.

Although ECT is widely used in defect detection, the share is still relatively small comparing with other NDT techniques, especially in weld inspection. A uniform eddy current probe was proved to reveal the flaws in weld part, where structure deformations and electromagnetic characteristics generated great noises [11]. Some experimental results tested on Inconel welds with rough surfaces indicated different designs of probes had different sensitivity to the roughness of surface, among which differential probes were more sensitive. And the notch dimensions were accomplished with a reconstructed profile [62]. Noritaka Yusa et al. compared the results of fatigue cracks detection and sizing by ECT, destructive testing, potential drop and UT method. They proved that ECT was the most efficient among these methods [63]. In their methods, it was important to choose a proper frequency to minimise the effects of surface roughness. A new differential probe termed Ionic eddy current probe was introduced to detect superficial defects on FSW specimens [64]. The probe was able to detect micro size defects as small as 60 μm. There were some research work conducting defect detection for weld [65] [66] [67] [68]. In [66] [67] [68], C-scan imaging was used which provides a visual identification of defects. However, few efforts are contributed to material characterisation

for weld. In paper [69], a C-scan conductivity image of a cross-section of friction stir weld of an aluminium plate is shown. They used a planar EM coil with 5 mm diameter at an extremely low lift-off (50 μm). The weld zones were recognized in the EM image. In addition, EM data showed a relationship with the hardness.

Speak of the correlation with hardness, the relationship between eddy current and hardness or microstructure is established for a variety kind of materials. In [70], hardness with different case depths for AISI 1045 steel was evaluated with comparison of ECT. In [71], eddy current method was used to determine the surface carbon content in AISI 4118 steel in gas carburizing process. A variety kind of cast irons was evaluated with both ECT and hardness method in [72]. The correlation between eddy current data and hardness were approved in above research. Both ferromagnetic and non-ferromagnetic samples were evaluated with different heat treatment [73]. The eddy current data and grain sizes and hardness data were compared. However, no strong relationship was established in their paper.

2.3 Summary

Fusion welding process is widely used in variety of manufacturing industries. The heat in the weld results in metal microstructure transformation. Consequently, the physical, mechanical and electromagnetic properties vary in the weld zones. Currently, ECT is developing in weld inspection due to the fact that it is fast, cheap and reliable comparing to other NDT methods. However, it mainly focuses in defect detection. There is barely any application on material characterisation for weld. In terms of the relationship between EM

data and hardness data, ECT has the potential in weld characterisation that can reveal its mechanical and microstructure information.

Chapter 3 Support Theory

An inductive sensor is usually the case for EM testing. The supporting theory includes basic Maxwell's equations, eddy current, impedance of the sensor and some geometrical effects. Dodd and Deeds [51] proposed a classic analytical solution for a coil above a planar. The solution has been expanded to co-axial and non-axial sensor structure, describing the calculation of impedance changes of sensor due to test sample.

3.1 Fundamental of Inductive Sensor

Conventional inductive sensor usually contains one or multiple coils including exciting coil and receiving coil. Depending on the operating mode, the exciting current could be sinusoidal signal or pulse signal. No matter what the exciting current is, the fundamental of an inductive sensor is described by Maxwell's equations. The alternating exciting signal in the exciting coil will produce an alternating magnetic field. An induced current will be induced in the receiving coil, and a secondary magnetic field in the receiving coil will be opposite to the primary field. The coupling between two coils is affected by approaching of an electric and magnetic conductive tested sample. Hence, the electromagnetic information of the tested sample can be deduced by examining the receiving signal.

3.1.1 Maxwell's Equations

The differential Maxwell's equations for continuous fields in today's notation are described as below [74] [75].

Equation 3-1

$$\nabla \times \boldsymbol{E} = -\frac{\partial \boldsymbol{B}}{\partial t}$$

Equation 3-2

$$\nabla \times \boldsymbol{H} = \boldsymbol{J} + \frac{\partial \boldsymbol{D}}{\partial t}$$

Equation 3-3

$$\nabla \cdot \boldsymbol{B} = 0$$

Equation 3-4

$$\nabla \cdot \boldsymbol{D} = \rho$$

Where ***E*** (unit is volt per meter, V/m) represents electric field intensity; ***H*** (A/m) is called the magnetic intensity; ***B*** (T) is the symbol of magnetic flux density; and the vector ***D*** (C/m^2) is the electric flux density. The current density is defined as ***J*** (A/m^2). And ρ is termed as the electric charge density. According to Faraday's law in Equation 3-1, with an alternating current (AC) in the inductive coil, there will be a time-varying magnetic field. The electrical Gauss's law in Equation 3-4 reveals that the electric field is produced by the displacement of electric charges. Similarly, there are no magnetic charges as described in Equation 3-3. The Ampere's circuital law in Equation 3-2 describes how magnetic field relates to electrical current and time-varying electric field.

The constitutive relations between these vectors are followed by

Equation 3-5

$$\boldsymbol{J} = \sigma \boldsymbol{E}$$

Equation 3-6

$$\boldsymbol{B} = \mu \boldsymbol{H}$$

Equation 3-7

$$\boldsymbol{D} = \varepsilon \boldsymbol{E}$$

Where μ, σ and ε denote the magnetic permeability, electrical conductivity and permittivity of the associated media, respectively. In free space, the magnetic constant μ_0 is defined by

$$\mu_0 = 4\pi \times 10^{-7}\ (H/m).$$

The vacuum permittivity related to the vacuum permeability and the speed of light in free space is defined as

$$\varepsilon_0 = 8.854\ldots \times 10^{-12}\ (F/m).$$

3.1.2 Impedance of Sensor

A coil is characterised by its impedance $\boldsymbol{Z}_0$ which is defined as

Equation 3-8

$$\boldsymbol{Z_0} = \frac{\boldsymbol{V_0}}{\boldsymbol{I_0}} = R_0 + jX_0 = R_0 + j\omega L$$

The real part of the complex impedance R_0 is the resistance, and the imaginary part X_0 is equal to ωL. ω denotes the angular frequency and L denotes the inductance of the coil.

As shown in Figure 3.1, with the proximity of a sample with conductivity σ and permeability μ, the magnetic field will change based on the permeability of the sample; and it will also induce an eddy current in the sample, which will produce a secondary magnetic field in the opposite direction of the primary

field. As a result, the impedance of the coil will change with respect to the conductivity and permeability of the sample.

With fixed exciting current, the differences in impedance or the voltage of the sensor can be used to characterise the conductivity and permeability of the tested sample.

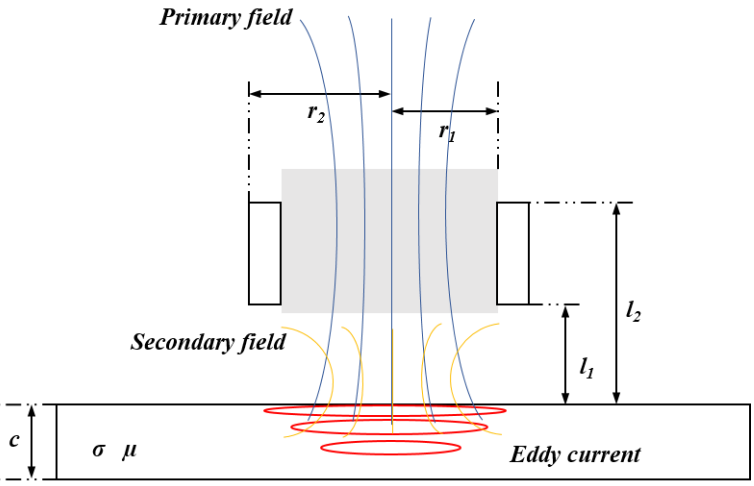

Figure 3.1 Front view of an air core rectangular cross-section coil above a tested sample (c denotes the thickness of the sample, r_1 and r_2 denote the inner and outer radius of the coil, and l_1 and l_2 denote the distance between the bottom or the top of the coil and the sample), with brief view of primary and induced eddy current and secondary field.

The normal impedance plane is illustrated in Figure 3.2 adapted from [76]. The displacement in impedance plane from P_0 to P_1 demonstrates that the sensor approaches a non-ferromagnetic material from air. Similarly, P_3 represents when the sensor approaches a ferromagnetic material. The impedance displacement is determined by the conductivity / permeability of the presented materials and lift-off. In addition, crack will cause a displacement from P_1 or P_3. For non-ferromagnetic materials, the imaginary part is smaller than that of air. For ferromagnetic materials, the imaginary part becomes larger than that of air. The real part increases for both materials because of the eddy current dissipation.

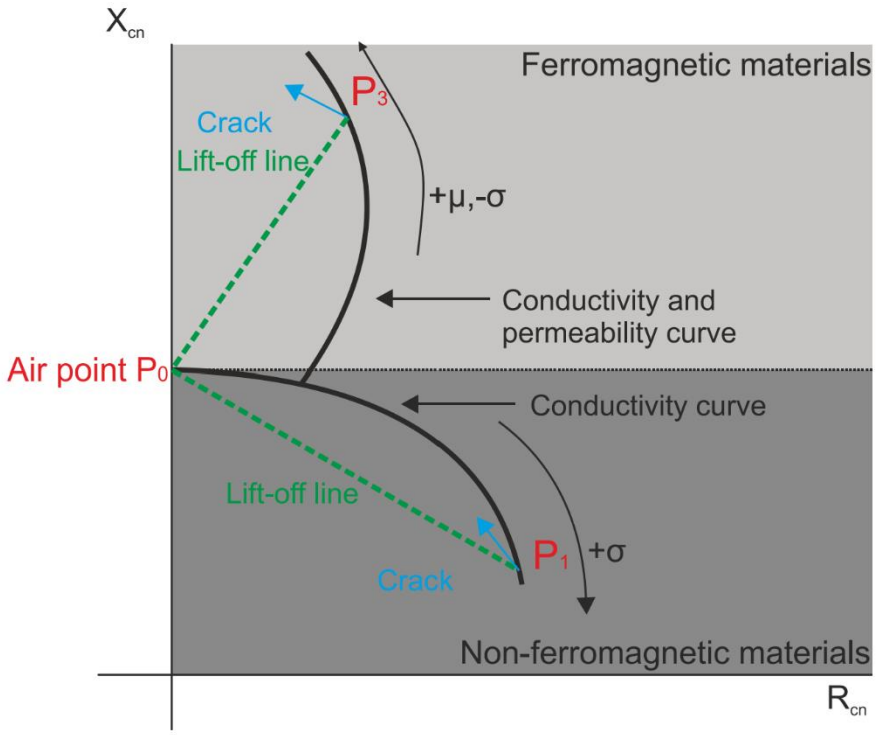

Figure 3.2 Impedance plane for ferromagnetic and non-ferromagnetic materials [76].

3.1.3 Geometry Effect of Sample

Other than the inherent EM properties, the geometry parameters of tested sample also affect the impedance changes of inductive sensor, such as shape, thickness and surface condition. These are related to the edge effect, depth of penetration and lift-off effect.

Edge effect: When the sensor is near the edge of the sample, the eddy current path is disturbed by the edge, hence it results in impedance changes of the sensor. The eddy current distribution as a cylindrical coil crossing the edge of a conductive metal was evaluated in [77]. The eddy current is not evenly distributed near the edge. It also depends on the position of the coil. As the coil is above the area of the conductor and approaching the edge, the eddy

current on the edge increases. It is best to avoid the edge area when using ECT.

Skin depth: In mathematics, the skin depth δ is defined as where the eddy current density is e^{-1} of its surface density as written as

Equation 3-9

$$\delta = \frac{1}{\sqrt{\pi\mu\sigma f}}.$$

The skin depth decreases if the conductivity σ and permeability μ of the specimen increases. In addition, the frequency f has a negative effect on skin depth. When the frequency is high, the eddy current is difficult to penetrate the sample. The effecting depth is worthy considered when a sample has multiple layers, such as a coated pipeline, or the thickness of the sample is small. Typically, at 10 kHz, the penetration depth of eddy current is 0.85 mm for pure aluminium and 0.19 mm for carbon steel. The frequency used for ECT is usually higher than 10 kHz which will results in a smaller penetration depth.

Lift-off: The distance between the sample and the sensor is named lift-off which has a significant effect on the impedance changes. Because the magnetic field decays in medium, the change caused by the sample is decreasing as the lift-off increases. In welding inspection, a coarse surface will cause a lot noisy output signal. It is challenging to reduce the lift-off effect in EM testing.

3.2 Analytical Solution based on Dodd and Deeds

The analytical solution for eddy current problems was proposed by Dodd and Deeds in 1968 [51] [52]. It has been cited and validated by many researchers that it has high accuracy for air core sensor [78] [79] [80] [81] [82] [83]. The solution is suitable for the model in this thesis, except the effect of ferrite.

The eddy current is deduced by solving Equation 3-10 and Equation 3-11 [51].

Equation 3-10

$$\nabla^2\mathbf{A} = -\mu\boldsymbol{I} + \mu\sigma\frac{\partial\mathbf{A}}{\partial t} + \mu\varepsilon\frac{\partial^2\mathbf{A}}{\partial t^2} + \mu\nabla(\frac{1}{\mu}) \times (\nabla \times \mathbf{A})$$

Equation 3-11

$$\mathbf{J} = \sigma\mathbf{E} = -\sigma\frac{\partial\mathbf{A}}{\partial t} = -\mathrm{j}\sigma\omega\mathbf{A}$$

where $\mathbf{A}$ is the vector potential generated by the coil with a driving current density $\mathbf{I}$; μ, σ, and ε are the permeability, the conductivity and the permittivity of the tested sample respectively. The eddy current density $\mathbf{J}$ is represented by $-\mathrm{j}\sigma\omega\mathbf{A}$.

The solutions deal with two main situations: a rectangular cross-section coil above a half-space planar with a conductive coating in Figure 3.3 (a), and a rectangular cross-section coil encircling a two-conductor cylinder with infinite longitude in Figure 3.3 (b).

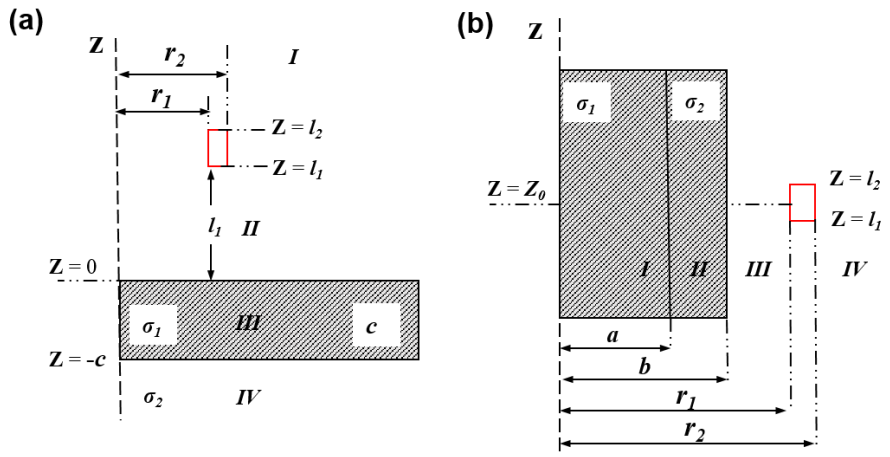

Figure 3.3 Diagrams of Dodd and Deeds' solution: (a) a rectangular cross-section coil above a half-space planar with a conductive coating; (b) a rectangular cross-section coil encircling a two-conductor cylinder with infinite longitude. The diagrams are in cylindrical coordinate system. The red rectangular represents the coil cross-section.

The thesis is interested in the situation of coil above a planar. The vector potential in each region is given as follows [51]:

Equation 3-12

$$\boldsymbol{A}^{(1)}(r,z) = \frac{1}{2}(\mu i_0)\int_0^\infty \frac{1}{\alpha^3} I(r_2,r_1) J_1(\alpha r) e^{-\alpha z} \left\{ e^{\alpha l_2} - e^{\alpha l_1} - (e^{-\alpha l_2} - e^{-\alpha l_1}) \times \left[\frac{(\alpha+\alpha_1)(\alpha_1-\alpha_2) + (\alpha-\alpha_1)(\alpha_1+\alpha_2)e^{2\alpha_1 c}}{(\alpha-\alpha_1)(\alpha_1-\alpha_2) + (\alpha+\alpha_1)(\alpha_1+\alpha_2)e^{2\alpha_1 c}} \right] \right\} d\alpha$$

Equation 3-13

$$\boldsymbol{A}^{(2)}(r,z) = \frac{1}{2}(\mu i_0)\int_0^\infty \frac{1}{\alpha^3} I(r_2,r_1) J_1(\alpha r)(e^{-\alpha l_1} - e^{-\alpha l_2}) \times \left\{ e^{\alpha z} + \left[\frac{(\alpha+\alpha_1)(\alpha_1-\alpha_2) + (\alpha-\alpha_1)(\alpha_1+\alpha_2)e^{2\alpha_1 c}}{(\alpha-\alpha_1)(\alpha_1-\alpha_2) + (\alpha+\alpha_1)(\alpha_1+\alpha_2)e^{2\alpha_1 c}} \right] e^{-\alpha z} \right\} d\alpha$$

Equation 3-14

$$\boldsymbol{A}^{(3)}(r,z) = \mu i_0 \int_0^\infty \frac{1}{\alpha^3} I(r_2,r_1) J_1(\alpha r)(e^{-\alpha l_1} - e^{-\alpha l_2}) \times \left[\frac{\alpha(\alpha_1+\alpha_2)e^{2\alpha_1 c}e^{\alpha_1 z} + \alpha(\alpha_1-\alpha_2)e^{-\alpha_1 z}}{(\alpha-\alpha_1)(\alpha_1-\alpha_2) + (\alpha+\alpha_1)(\alpha_1+\alpha_2)e^{2\alpha_1 c}} \right] d\alpha$$

Equation 3-15

$$\boldsymbol{A}^{(4)}(r,z) = \mu i_0 \int_0^{\infty} \frac{1}{\alpha^3} I(r_2, r_1) J_1(\alpha r)(e^{-\alpha l_1} - e^{-\alpha l_2}) \times \left[\frac{2\alpha\alpha_1 e^{(\alpha_1+\alpha_2)c} e^{\alpha_2 z}}{(\alpha-\alpha_1)(\alpha_1-\alpha_2) + (\alpha+\alpha_1)(\alpha_1+\alpha_2)e^{2\alpha_1 c}} \right] d\alpha$$

where $\alpha_i = \sqrt{\alpha^2 + j\omega\mu\sigma_i}$.

$\boldsymbol{A}^{(*)}(r,z)$ denotes the vector potential in corresponding area; α denotes a spatial variable; i_0 denotes the exciting current density; r_1, r_2 denotes the inner and outer radius of the coil respectively; $l_1$denotes the lift-off; $l_2 - l_1$ denotes the height of the coil; $J_1(\alpha r)$ is the first-order Bessel function. μ, σ_i denotes the permeability and conductivity of the corresponding region. Since the solution is only about conductive planar, all regions share the same permeability.

From Equation 3-11, the eddy current can be deduced.

The total voltage induced in a coil of $\boldsymbol{N}$ turns is shown in Equation 3-16.

Equation 3-16

$$\boldsymbol{V} = \frac{j2\pi\omega N}{(r_2 - r_1)(l_2 - l_1)} \iint r\mathbf{A}(r,z)\, drdz.$$

Hence the impedance of a coil is represented by $\boldsymbol{Z} = \boldsymbol{V}/\boldsymbol{I}$.

The coil impedance becomes

Equation 3-17

$$\boldsymbol{Z} = \frac{j\pi\omega\mu N^2}{(r_2 - r_1)^2(l_2 - l_1)^2}\int_0^\infty \frac{1}{\alpha^5} I^2(r_2, r_1)\left\{2(l_2 - l_1)\right.$$

$$+ \alpha^{-1}\left[2e^{\alpha l_1 - \alpha l_2} - 2\right.$$

$$+ (e^{-2\alpha l_1} + e^{-2\alpha l_2} - 2e^{-\alpha l_1 - \alpha l_2})$$

$$\left.\left.\times \frac{(\alpha + \alpha_1)(\alpha_1 - \alpha_2) + (\alpha - \alpha_1)(\alpha_1 + \alpha_2)e^{2\alpha_1 c}}{(\alpha - \alpha_1)(\alpha_1 - \alpha_2) + (\alpha + \alpha_1)(\alpha_1 + \alpha_2)e^{2\alpha_1 c}}\right]\right\} d\alpha.$$

3.2.1 Analytical Solution for Co-axial Sensor

If there is a co-axial pickup coil as shown in Figure 3.4, the mutual impedance of the sensor can be computed.

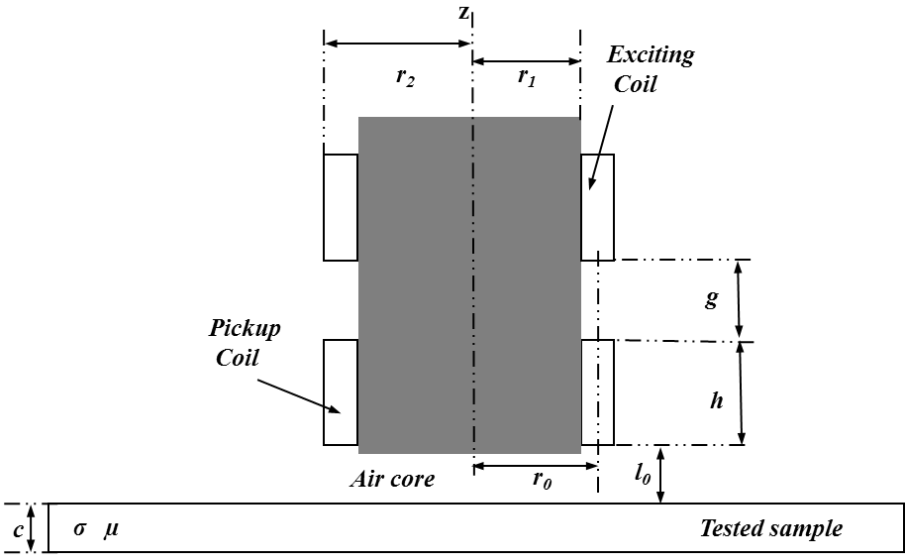

Figure 3.4 The diagram of the co-axial sensor

The difference in the complex inductance is $\Delta L(\omega) = L(\omega) - L_A(\omega)$, where the coil inductance above a plate is $L(\omega)$, and $L_A(\omega)$ is the inductance in free space.

The formulas of Dodd and Deeds are [78]:

Equation 3-18

$$\Delta L(\omega) = K\int_0^{\infty} \frac{P^2(\alpha)}{\alpha^6} A(\alpha)\phi(\alpha)d\alpha$$

Where

Equation 3-19

$$\phi(\alpha) = \frac{(\alpha_1+\alpha)(\alpha_1-\alpha)-(\alpha_1+\alpha)(\alpha_1-\alpha)e^{2\alpha_1 c}}{-(\alpha_1-\alpha)(\alpha_1-\alpha)+(\alpha_1+\alpha)(\alpha_1+\alpha)e^{2\alpha_1 c}}$$

Equation 3-20

$$\alpha_1 = \sqrt{\alpha^2 + j\omega\sigma\mu_0}$$

Equation 3-21

$$K = \frac{\pi\mu_0 N^2}{h^2(r_1-r_2)^2}$$

Equation 3-22

$$P(\alpha) = \int_{\alpha r_1}^{\alpha r_2} xJ_1(x)dx$$

Equation 3-23

$$A(\alpha) = e^{-\alpha(2l_0+h+g)}(1-e^{-2\alpha h})$$

μ_0 denotes the permeability of free space. *N* denotes the number of turns in the coil; r_1 and r_2 denote the inner and outer radii of the coil; while l_0 and *h* denote the lift-off and the height of the coil; and *c* denotes the thickness of the plate.

Equation 3-18 can be approximated based on the fact that $\phi(\alpha)$ varies slowly with α compared to the rest of the integrand, which reaches its maximum at a characteristic spatial frequency α_0. The approximation is to evaluate $\phi(\alpha)$ at α_0 and take it outside of the integral.

Equation 3-24

$$\Delta L(\omega) = \phi(\alpha_0)\Delta L_0$$

Where

Equation 3-25

$$\phi(\alpha_0) = \frac{(\alpha_1 + \mu\alpha_0)(\alpha_1 - \mu\alpha_0) - (\alpha_1 + \mu\alpha_0)(\alpha_1 - \mu\alpha_0)e^{2\alpha_1 c}}{-(\alpha_1 - \mu\alpha_0)(\alpha_1 - \mu\alpha_0) + (\alpha_1 + \mu\alpha_0)(\alpha_1 + \mu\alpha_0)e^{2\alpha_1 c}}$$

Equation 3-26

$$\Delta L_0 = K \int \frac{P^2(\alpha)}{\alpha^6} A(\alpha) d\alpha$$

Note that in Equation 3-24, the sensor phase signature is solely determined by $\phi(\alpha 0)$, which includes conductivity, the thickness of the conducting plate, and $\alpha 0$. $\Delta L0$ is the overall magnitude of the signal, which is strongly dependent on the coil geometrical parameters but independent of the thickness and electromagnetic properties of the plate.

Substituting $e^{2\alpha_1 c}$ with $1 + 2\alpha_1 c$, and considering Equation 3-20, Equation 3-25 becomes,

Equation 3-27

$$\phi(\alpha_0) \approx \frac{j\omega\sigma\mu_0 c}{j\omega\sigma\mu_0 c + 2\alpha_0{}^2 c + 2\alpha_0 + 2\alpha_0\alpha_1 c} .$$

Assigning

Equation 3-28

$$\omega_1 = \frac{2\alpha_0{}^2 c + 2\alpha_0}{\sigma\mu_0 c},$$

Equation 3-27 can be expressed as

Equation 3-29

$$\phi(\alpha) = \frac{j\omega/\omega_1}{j\omega/\omega_1 + 1 + 2\alpha_0\alpha_1 c/(2\alpha_0{}^2 c + 2\alpha_0)} .$$

In Equation 3-29, it can be seen that the peak frequency for the first order system is approximately ω_1 and from Equation 3-28, it is concluded that the peak frequency increases with α_0.

Suppose a lift-off variation of l_0 is introduced, from Equation 3-23, we can see that an increase of l_0 in lift-off is equivalent to multiplying a factor $e^{-2\alpha l_0}$:

Equation 3-30

$$A(\alpha) = \mathrm{e}^{-\alpha(2l_0+h+g)}(\mathrm{e}^{-2\alpha h}+1).$$

Due to the fact that $\Delta L_0 = K\int \frac{P^2(\alpha)}{\alpha^6} A(\alpha)d\alpha$ peaks at α_0 and that the squared Bessel term $P^2(\alpha)$ is the main contributor, a simple function $\sin^2(\frac{\alpha\pi}{2\alpha_0})$ with its maximum at α_0 is used to approximate ΔL_0 as shown in Figure 3.5.

Equation 3-31

$$\mathrm{Im}(\Delta L_0) \approx \mathrm{Im}(\Delta L_m) e^{-2\alpha l_0} \sin^2(\frac{\alpha\pi}{2\alpha_0})$$

where ΔL_m denotes the magnitude of the inductance change when the lift-off is zero. This simplification is applied to obtain an analytical solution for α_0.

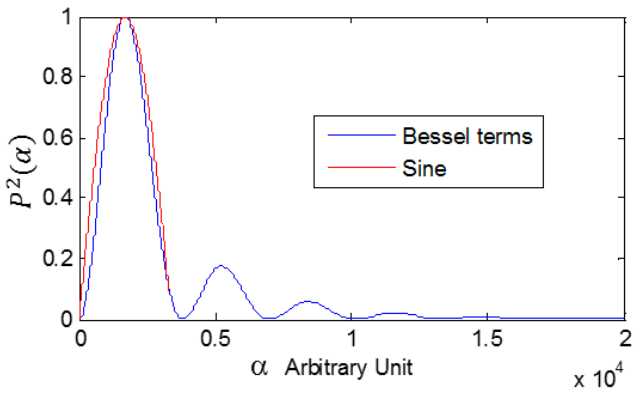

Figure 3.5 Approximation of the Bessel term with a sinusoid.

The shift in α_0 due to the effect of lift-off can be predicted as follow.

The new α should maximize $e^{-2\alpha l_0}\sin^2(\frac{\alpha\pi}{2\alpha_0})$ and therefore $e^{-\alpha l_0}\sin(\frac{\alpha\pi}{2\alpha_0})$.

The maximum can be obtained by finding the stationary point for $e^{-\alpha l_0}\sin(\frac{\alpha\pi}{2\alpha_0})$.

Let $\left(e^{-\alpha l_0}\sin(\frac{\alpha\pi}{2\alpha_0})\right)' = -l_0\cdot e^{-\alpha l_0}\sin(\frac{\alpha\pi}{2\alpha_0}) + \frac{\pi}{2\alpha_0}e^{-\alpha l_0}\cos(\frac{\alpha\pi}{2\alpha_0}) = 0$,

And through some mathematical manipulations, a new equation can be obtained:

Equation 3-32

$$\frac{\alpha\pi}{2\alpha_0} = \tan^{-1}(\frac{\pi}{2\alpha_0 l_0}).$$

With small lift-off variation, $\alpha_0 l_0 << 1$ holds, the right side can be approximated as $\frac{\pi}{2} - \frac{2\alpha_0 l_0}{\pi}$.

Therefore, the revised α_0, α_{0r} is

Equation 3-33

$$\alpha_{0r} = \alpha_0 - \frac{4\alpha_0^2 l_0}{\pi^2}$$

Combining Equation 3-28 with Equation 3-33, ω_1 becomes

Equation 3-34

$$\omega_1 \approx \frac{2\left(\alpha_0^2\pi^4 - 8\pi^2\alpha_0^3 l_0 + 16\alpha_0^4 l_0^2\right)c + 2\left(\alpha_0\pi^4 - \pi^2 4\alpha_0^2 l_0\right)}{\pi^4\sigma\mu_0 c}.$$

Combining Equation 3-31 with Equation 3-33, $\mathrm{Im}(\Delta L_0)$ becomes

Equation 3-35

$$Im(\Delta L_0) = Im(\Delta L_m)\, e^{-2(\alpha_0 - \frac{4\alpha_0^2 l_0}{\pi^2})l_0}\, cos^2(\frac{2\alpha_0 l_0}{\pi})$$

$$= Im(\Delta L_m)\, e^{-2(\alpha_0 - \frac{4\alpha_0^2 l_0}{\pi^2})l_0} \left(\frac{1}{2} cos(\frac{4\alpha_0 l_0}{\pi}) + \frac{1}{2}\right).$$

Considering $\alpha_0 l_0 << 1$ and based on small-angle approximation $\cos(\theta) \approx 1 - \frac{\theta^2}{2}$,

$\cos(\frac{4\alpha_0 l_0}{\pi})$ is substituted with $1 - \frac{\left(\frac{4\alpha_0 l_0}{\pi}\right)^2}{2}$.

$\mathrm{Im}(\Delta L_0)$ becomes

Equation 3-36

$$\mathrm{Im}(\Delta L_0) = \mathrm{Im}(\Delta L_m) e^{-2(\alpha_0 - \frac{4\alpha_0^2 l_0}{\pi^2})l_0} (1 - \frac{4\alpha^2 l^2}{\pi^2}).$$

Substituting $\left(1 - \frac{4\alpha^2 l^2}{\pi^2}\right)$ with $e^{-\frac{4\alpha_0^2 l_0^2}{\pi^2}}$,

Equation 3-37

$$\mathrm{Im}(\Delta L_0) = \mathrm{Im}(\Delta L_m) e^{-2(\alpha_0 - \frac{4\alpha_0^2 l_0}{\pi^2})l_0} e^{-\frac{4\alpha_0^2 l_0^2}{\pi^2}}$$
$$= \mathrm{Im}(\Delta L_m) e^{-2(\alpha_0 - \frac{2\alpha_0^2 l_0}{\pi^2})l_0}.$$

Taking natural logarithmic operation of both sides, we arrive at:

Equation 3-38

$$\ln \frac{\mathrm{Im}(\Delta L_0)}{\mathrm{Im}(\Delta L_m)} = -2(\alpha_0 - \frac{2\alpha_0^2 l_0}{\pi^2})l_0.$$

And further:

$$4\alpha_0^2 l_0^2 - 2\pi^2 \alpha_0 l_0 - \pi^2 \ln \frac{\mathrm{Im}(\Delta L_0)}{\mathrm{Im}(\Delta L_m)} = 0$$

This is now a quadratic equation with $\alpha_0 l_0$ as its variable.

Therefore, the solution for $\alpha_0 l_0$ is

Equation 3-39

$$\alpha_0 l_0 = \frac{1}{4}[\pi^2 - \sqrt{\pi^4 + 4\pi^2 \ln \frac{Im(\Delta L_0)}{Im(\Delta L_m)}}].$$

The other solution $\alpha_0 l_0 = \frac{1}{4}[\pi^2 + \sqrt{\pi^4 + 4\pi^2 \, ln\frac{Im(\Delta L_0)}{Im(\Delta L_m)}}]$ does not satisfy the small lift-off condition $\alpha_0 l_0 << 1$ and therefore are discarded.

From Equation 3-39, lift-off can be estimated as

Equation 3-40

$$l_0 = \frac{\pi^2 - \sqrt{\pi^4 + 4\pi^2 \ln \frac{\mathrm{Im}(\Delta L_0)}{\mathrm{Im}(\Delta L_m)}}}{4\alpha_0}.$$

Combining Equation 3-34 with Equation 3-40, the peak frequency with a lift-off of l_0 becomes

Equation 3-41

$$\omega_1 = \frac{2\alpha_0{}^2 c\left(\pi^2 + 4\ln\frac{\mathrm{Im}(\Delta L_0)}{\mathrm{Im}(\Delta L_m)}\right) + 2\alpha_0\pi\sqrt{\pi^2 + 4\ln\frac{\mathrm{Im}(\Delta L_0)}{\mathrm{Im}(\Delta L_m)}}}{\pi^2\sigma\mu_0 c}.$$

The above equation becomes a quadratic equation with an unknown α_0,

$$2c\left(\pi^2 + 4\ln\frac{\mathrm{Im}(\Delta L_0)}{\mathrm{Im}(\Delta L_m)}\right)\alpha_0{}^2 + 2\pi\sqrt{\pi^2 + 4\ln\frac{\mathrm{Im}(\Delta L_0)}{\mathrm{Im}(\Delta L_m)}}\alpha_0 - \omega_1\pi^2\sigma\mu_0 c = 0$$

And the solution is

Equation 3-42

$$\alpha_0 = \frac{-\pi\sqrt{\pi^2 + 4\ln\frac{\mathrm{Im}(\Delta L_0)}{\mathrm{Im}(\Delta L_m)}} + \sqrt{\pi^2(2\omega_1\sigma\mu_0 c^2 + 1)\left(\pi^2 + 4\ln\frac{\mathrm{Im}(\Delta L_0)}{\mathrm{Im}(\Delta L_m)}\right)}}{2c\left(\pi^2 + 4\ln\frac{\mathrm{Im}(\Delta L_0)}{\mathrm{Im}(\Delta L_m)}\right)}$$

$$= \frac{\pi\left(\sqrt{\left(1 + 2\omega_1\sigma\mu_0 c^2\right)} - 1\right)}{2c\sqrt{\pi^2 + 4\ln\frac{\mathrm{Im}(\Delta L_0)}{\mathrm{Im}(\Delta L_m)}}}.$$

Therefore, the original peak frequency (peak frequency prior to introducing the lift-off l_0) can be obtained by combining Equation 3-28 with Equation 3-42:

Equation 3-43

$$\omega_0 = \frac{2\alpha_0^{\,2}c + 2\alpha_0}{\sigma\mu_0 c}$$

$$= \frac{\pi^2\left(\sqrt{\left(1+2\omega_1\sigma\mu_0 c^2\right)}-1\right)^2 + 2\pi\left(\sqrt{\left(1+2\omega_1\sigma\mu_0 c^2\right)}-1\right)\sqrt{\pi^2 + 4\ln\frac{\mathrm{Im}\left(\Delta L_0\right)}{\mathrm{Im}\left(\Delta L_m\right)}}}{2\sigma\mu_0 c^2\left(\pi^2 + 4\ln\frac{\mathrm{Im}\left(\Delta L_0\right)}{\mathrm{Im}\left(\Delta L_m\right)}\right)}.$$

It can be seen in Equation 3-43 that through a compensation scheme, using the knowledge of the peak frequency and the amplitude at a certain lift-off, the original peak frequency (peak frequency prior to introducing the lift-off l_0) can be recovered.

3.2.2 Analytical Solution for Non-axial Sensor

Here provides the adopted solution for a non-axial sensor with coils arranged in parallel to each other [84].

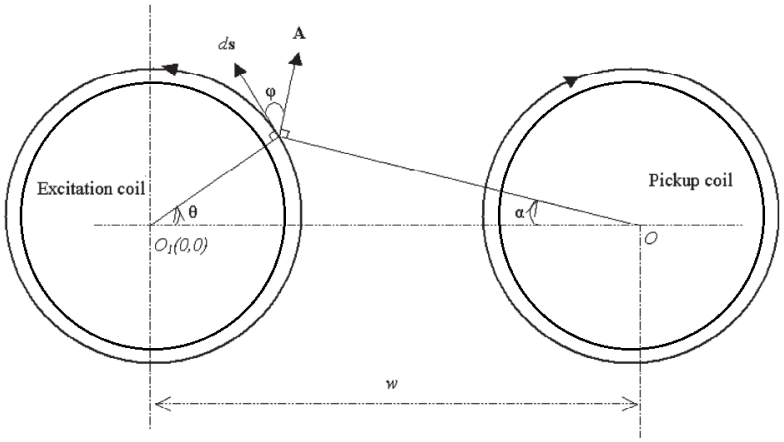

Figure 3.6 Top view of non-axial sensor

The exciting coil and pick-up coil are both on the top of the plate with coordinates of (-1.5, 0, *l*) mm and (1.5, 0, *l*) mm respectively (where *l* denotes the lift-off of probes) as shown in Figure 3.6.

In the region between l_1 and l_2, the vector potential can be expressed as Equation 3-44, where N1, N2 denote the number of turns in the excitation and pickup coil; α is a spatial frequency variable; μ_0 denotes the permeability of free space; l_{e1} and l_{e2} denote the height of bottom and top of the excitation coil; while l_{p1} and l_{p2} denote the height of bottom and top of the pickup coil; r_{e1} and r_{e2} denote the inner and outer radii of the excitation coil; while r_{p1} and r_{p2} denote the inner and outer radii of the pickup coil; and c denotes the thickness of the plate. **J**(x) is a first-order Bessel function of the first kind. **I**(x1, x2) represent the production of **J**(x) for radii of x1 and x2.

Equation 3-44

$$\mathbf{A}^{(1,2)}(r,z)$$
$$=\frac{\mu_0 IN1}{(r_{e_2}-r_{e_1})(l_{e_2}-l_{e_1})}\int_0^{\infty}\frac{1}{\alpha^3}\mathbf{I}(r_{e_2},r_{e_1})\cdot\mathbf{J}(\alpha r)[2-e^{\alpha(z-l_{e_2})}-e^{\alpha(z-l_{e_1})}$$
$$+e^{-\alpha z}\left(e^{-\alpha l_{e_1}}-e^{-\alpha l_{e_2}}\right)\frac{(\alpha_1+\mu\alpha)(\alpha_1-\mu\alpha)-(\alpha_1+\mu\alpha)(\alpha_1-\mu\alpha)e^{2\alpha_1 c}}{-(\alpha_1-\mu\alpha)(\alpha_1-\mu\alpha)+(\alpha_1+\mu\alpha)(\alpha_1+\mu\alpha)e^{2\alpha_1 c}}]d\alpha$$

.

The voltage induced in probes with a single loop can be expressed as

Equation 3-45

$$V=j\omega\int_s\mathbf{A}(r,z)d\mathbf{s}=j\omega\int_s\mathbf{A}(r,z)r_p\cos(\varphi)d\theta$$

,

where $\varphi=\theta+tg^{-1}\left(r_p\sin\theta/\left(w-r_p\cos\theta\right)\right)$ is the angle between **A** and ds; s denotes the transect area in the pickup coil; while $r=\sqrt{r_p{}^2\sin^2\theta+\left(w-r_p\cos\theta\right)^2}$ is the distance between *O* and ds; $\alpha_1=\sqrt{\alpha^2+j\omega\sigma\mu_r\mu_0}$.

Considering Equation 3-44 and Equation 3-45, the induced voltage on the receiver can yield in

Equation 3-46

$$V=\frac{N1N2\,j\omega\mu_0 I}{(r_{e_2}-r_{e_1})(l_{e_2}-l_{e_1})(r_{p_2}-r_{p_1})(l_{p_2}-l_{p_1})}\int_0^{\infty}\int_0^{2\pi}\int_{r_{p1}}^{r_{p2}}\cos\left(\theta+tg^{-1}\left(\frac{r_p\sin\theta}{w-r_p\cos\theta}\right)\right)\frac{1}{\alpha^3}\mathbf{I}(r_{e_2},r_{e_1})$$
$$\mathbf{J}(\alpha\sqrt{r_p{}^2\sin^2\theta+\left(w-r_p\cos\theta\right)^2})\{2(l_{e_2}-l_{e_1})-\frac{1}{\alpha}[2e^{-\alpha(l_{e_2}-l_{e_1})}-2+\left(e^{-\alpha l_{e_1}}-e^{-\alpha l_{e_2}}\right)^2$$
$$\frac{(\alpha_1+\mu\alpha)(\alpha_1-\mu\alpha)-(\alpha_1+\mu\alpha)(\alpha_1-\mu\alpha)e^{2\alpha_1 c}}{-(\alpha_1-\mu\alpha)(\alpha_1-\mu\alpha)+(\alpha_1+\mu\alpha)(\alpha_1+\mu\alpha)e^{2\alpha_1 c}}]\}dr_p d\theta d\alpha$$

.

Consequently, the mutual inductance between the double air-cored coils can be presented by dividing the induced voltage by the current flowing through the excitation coil, as shown in Equation 3-47.

Equation 3-47

$$L = \frac{N1N2\mu_0}{\left(r_{e_2}\text{-}r_{e_1}\right)\left(l_{e_2}\text{-}l_{e_1}\right)\left(r_{p_2}\text{-}r_{p_1}\right)\left(l_{p_2}\text{-}l_{p_1}\right)} \int_0^{\infty}\int_0^{2\pi}\int_{r_{p1}}^{r_{p2}} \cos\left(\theta + tg^{-1}\left(\frac{r_p \sin\theta}{w - r_p\cos\theta}\right)\right)\frac{1}{\alpha^3}\mathbf{I}(r_{e_2}, r_{e_1})$$

$$\mathbf{J}(\alpha\sqrt{r_p{}^2\sin^2\theta + \left(w - r_p\cos\theta\right)^2})\{2\left(l_{e_2}\text{-}l_{e_1}\right) - \frac{1}{\alpha}[2e^{-\alpha\left(l_{e_2}\text{-}l_{e_1}\right)} - 2 + \left(e^{-\alpha l_{e_1}} - e^{-\alpha l_{e_2}}\right)^2$$

$$\frac{(\alpha_1+\mu\alpha)(\alpha_1-\mu\alpha)-(\alpha_1+\mu\alpha)(\alpha_1-\mu\alpha)e^{2\alpha_1 c}}{-(\alpha_1-\mu\alpha)(\alpha_1-\mu\alpha)+(\alpha_1+\mu\alpha)(\alpha_1+\mu\alpha)e^{2\alpha_1 c}}]\}dr_p d\theta d\alpha$$

.

3.3 Summary

The fundamental theory of inductive sensor is given in this chapter. In addition, the performance of the sensor (including co-axial and non-axial types) can be studied based on the analytical solutions that is developed from Dodd and Deeds' solution. The effects of coil parameters, lift-off, sample size and working frequency can be simulated based on these solutions. The drawback is the solution is based on air core coils. It does not cover the effect of a ferrite core. However, it is sufficient to understand the behaviour of inductive sensors. The solver is used as a simulation tool in Chapter 4 and 5 to verify the experimental results and evaluate the feasibility of proposed method.

Chapter 4 Sensor Design

In this chapter, conventional inductive sensors are studied. The structures of different inductive sensors are evaluated including co-axial and non-axial sensor. An optimised design of inductive sensor is proposed for welding inspection. Its performance such as sensitivity and spatial resolution is evaluated. The lift-off effect is also assessed. A conductivity invariance phenomenon (CIP) is discovered during the lift-off effect study. The CIP is validated by analytical and experimental results. The contents in Sections 4.6 and 4.7 have been published on NDT & E International [84]. As a co-author, I contributed to the experimental parts of the paper. Lu contributed to the calculation of the analytical solver.

4.1 Design Strategy

Nowadays an EM inspection system usually contains a hosting device, excitation, data acquisition module and sensing module. Thanks to the advanced chip development, the performance of hardware for hosting device and data acquisition module is normally surplus. Sensor design is a key factor to improve the performance of an EM inspection system [85] [86] [87] [88] [89].

The impedance of an inductive sensor is determined by its configuration involving the number and arrangements of coils and their parameters such as coil winding turns, dimensions and exciting frequency, etc [90]. The coupling effect between exciting and pickup coils is affected by the electromagnetic and geometrical parameters of the test sample. Metal shields are also considered in sensor design to improve the detectability of defects [91]. It is reported that the shield can improve the sensor's sensitivity of defects. Generally high-

quality welding products have small electromagnetic properties variances between different weld zones and the possible existing defects size is insignificant. Sensitivity and spatial resolution are of primary importance for sensor specification for material characterisation, in particular for imaging. It is well known that reducing the sensor size can provide a better spatial resolution whereas it also results in a reduction in signal level and sensitivity. A sensor is therefore desired to be as small as possible while meeting the requirements of producing adequate signal.

4.2 Study of Traditional Sensor

For a sensor comprising an exciting coil and a pickup coil, two arrangements are studied: one is when two coils are co-axial arranged; the other is when two coils are arranged non-axially as shown in Figure 4.1. Ferrite core is used to reduce the magnetic flux leakage in both configurations.

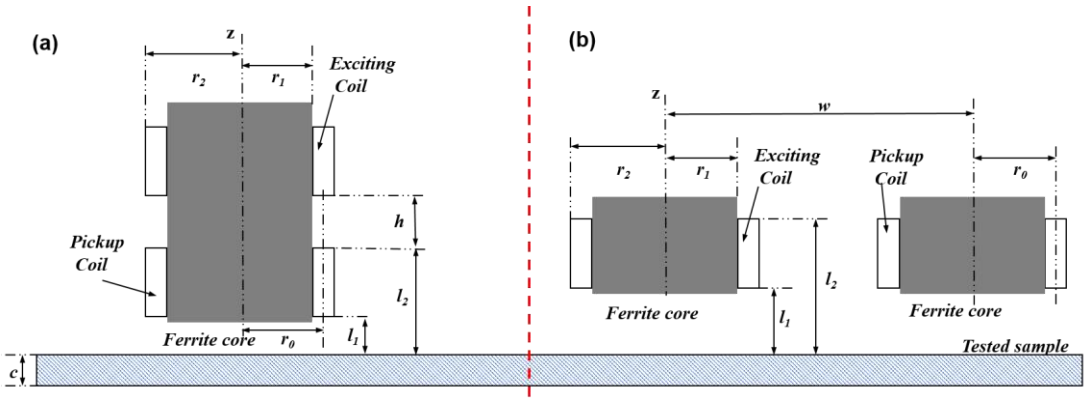

Figure 4.1 The configuration of sensors: (a) with co-axial coils; (b) with non-axial coils.

The parameters of the sensor studied are listed in Table 4-1. The two sensors comprise the same exciting coil and pickup coil parameters, only have different arrangements. The distance (h) between two coils is 3 mm for co-axial sensor, while distance (w) means the distance between two axial centers for non-axial

sensor. The ferrite core has 0.75 mm radius and 2300 relative permeability (μ_r).

Table 4-1 Parameters of sensor

Inner radius r_1 (exciting/pickup)	0.75mm/0.75mm
Outer radius r_2 (exciting/pickup)	1mm/1.25mm
$r_0 = (r_{1+} r_2)/2$ (exciting/pickup)	0.88mm/1mm
h (distance between two coils in (a))	3 mm
w (width between two coils' center in (b))	3mm
$l_2 - l_1$ (height of coils)	3mm
l_1 (lift-off)	0-10mm
Plate thickness c	5mm
Number of turns N1 / N2 N1 for Exciting coil, N2 for pickup coil	160/200

4.2.1 FEM Model

The two sensors mentioned above are simulated by commercial software ANSYS Maxwell. The software is based on finite element method (FEM). Models of sensors built in ANSYS Maxwell are shown in Figure 4.2 (a) and (b) with the predefined parameters shown in Table 4-1. The sensors are simulated above an aluminium plate with dimensions of 30 mm × 30 mm × 5 mm. The length of aluminium plate is larger than 5 times of the sensor size. Hence the model can be regarded as sensor above an infinite plane. The meshing region is set as 50% larger on each coordinate direction. The region is assigned as vacuum. In Figure 4.2 (c) and (d), the models are meshed with numbers of triangles. The accuracy of FEM simulation depends on the meshing amounts. Generally, larger amounts of meshing contribute to more accurate results but also consume longer computation time. The aiming percentage error is set as

0.5% which provides enough accuracy, and the meshing numbers are determined in the software. The PC used to perform the simulation features Intel Core i5-4690K and 16 GB RAM.

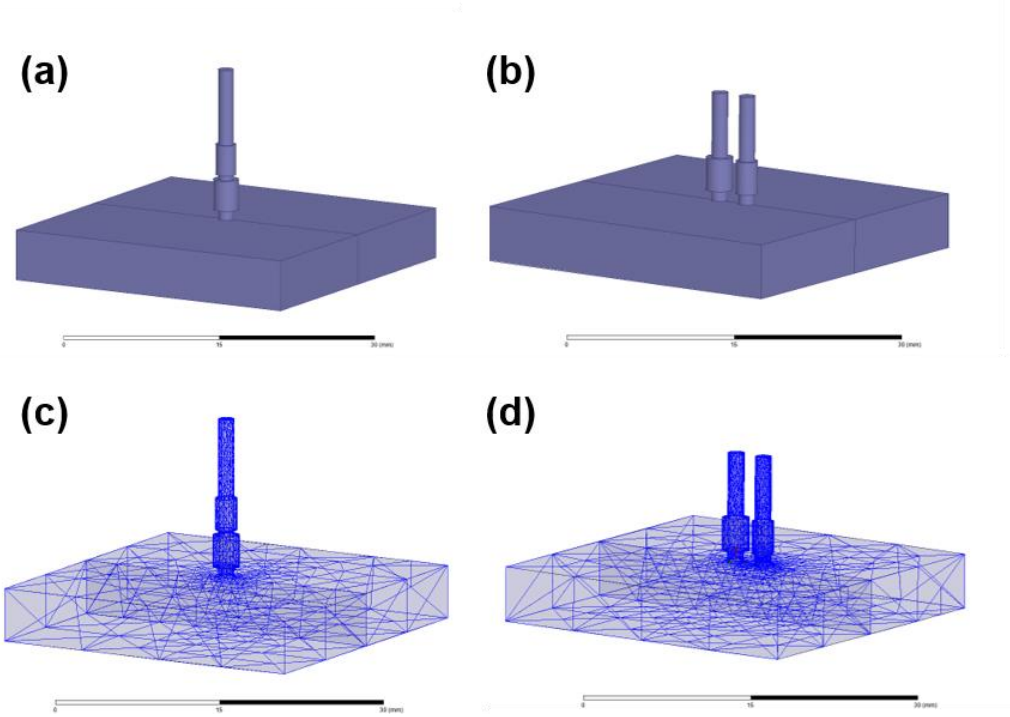

Figure 4.2 (a) and (b) are the models of sensors built in ANSYS Maxwell; (c) and (d) illustrate the mesh condition for numerical solution.

The eddy current induced on the surface of aluminium is computed as shown in Figure 4.3. The magnitude of the eddy current maximises right underneath the edge of the coil. Besides the eddy current of non-axial sensor is larger than that of co-axial sensor. This is because both exciting and pickup coils are closer and the coupling between the sensors and the tested sample is stronger. For the co-axial sensor, the eddy current circulates into a relatively large area compared to the non-axial sensor. For the non-axial sensor, the large amount of eddy current is concentrating in the center area of the exciting and pickup coils. Therefore, the non-axial sensor has a better spatial resolution than the co-axial sensor. Along with the increasing of frequency, the magnitude of eddy

current is increasing. The range of eddy current shrinks into finer area underneath the sensor. When the frequency is high e.g. 100 kHz, the spatial resolution of two types of sensors becomes similar.

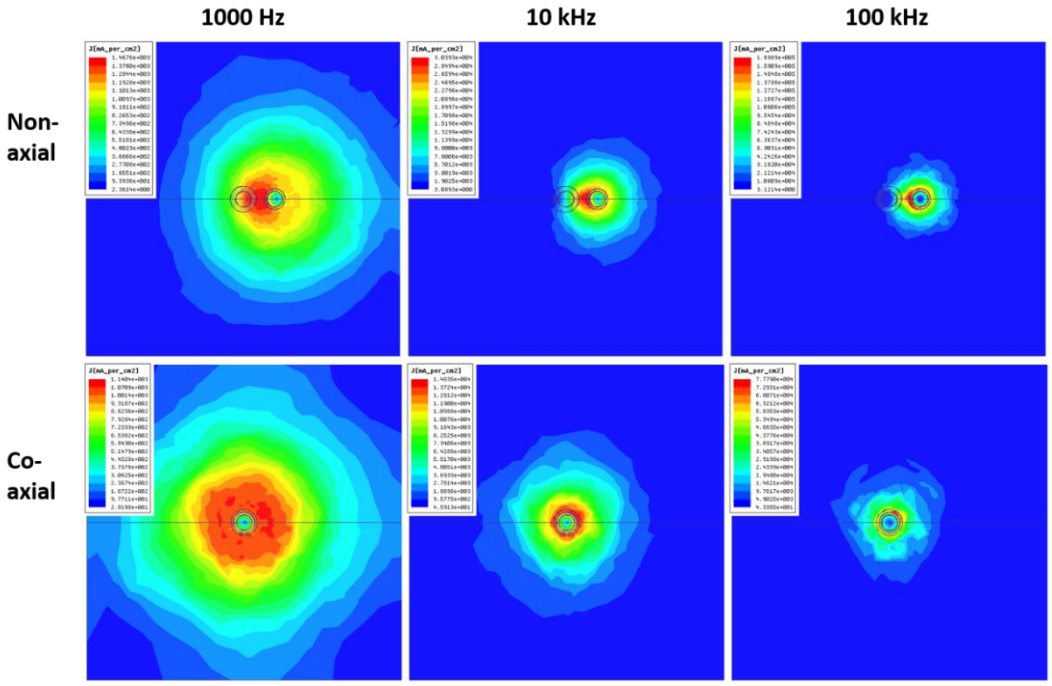

Figure 4.3 The eddy current on the surface of aluminium plate from the top view for two models at frequencies of 1 kHz, 10 kHz and 100 kHz.

4.2.2 Summary

The co-axial and non-axial sensors with one exciting and one pickup coil are studied. From the FEM modelling, the eddy current induced in the conductive plate reaches maximum magnitude at the edge of the coils. The eddy current of the non-axial sensor is larger than that of the co-axial sensor. And the non-axial sensor possesses a better spatial resolution as the eddy current concentrates more between the exciting and pickup coils. Consequently, the gap distance between exciting and pickup coil should be minimised to achieve a fine spatial resolution.

4.3 Sensor Configurations

The magnetic flux distribution can be restricted by ferrite due to its higher permeability than air. Thus, a cup-ferrite is used to improve the flux path of a traditional open T-R sensor. Practical models of the proposed cup-ferrite enclosed T-R sensor and traditional sensor are made and shown in Figure 4.4. The coils are wound around ferrite core, by copper wires with 0.056 mm diameter. The parameters are specified as in Table 4-1. The cup-ferrite has a 10 mm diameter and 1 mm wall thickness.

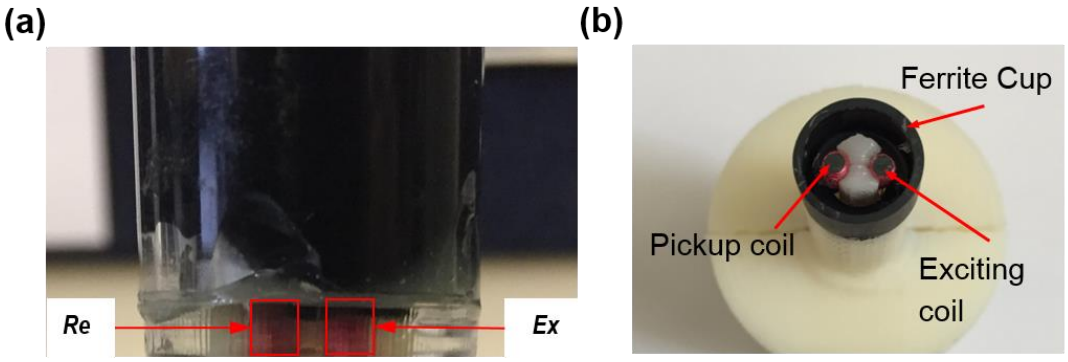

Figure 4.4 The pictures of practical models; (a) traditional open T-R sensor, and (b) cup-ferrite enclosed T-R sensor.

Traditional open T-R sensor is put inside a plastic cover and encapsulated with epoxy glue (black colour). Cup-ferrite enclosed T-R sensor is assembled inside a 3D printed outer shell (non-metal) as illustrated in Figure 4.5. Both the cup-ferrite sensor and T-R sensor are featured an Ethernet connection for the instrument. The ethernet connection provides an easy plug-in connection with the instrument and a robust signal communication.

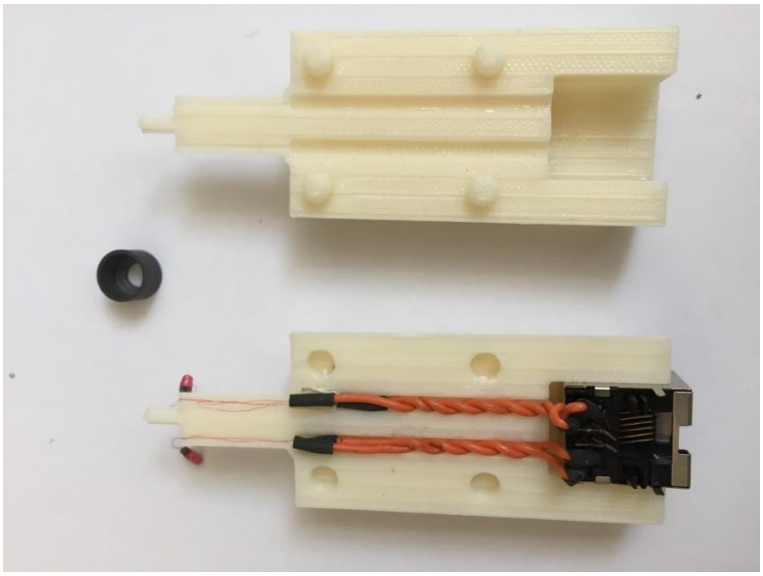

Figure 4.5 The picture of inner structure of the cup-ferrite T-R sensor, showing the exciting and pickup coils, cup-ferrite, and Ethernet socket for connections with instrument.

4.4 EM Instrument

A bespoke, high-speed EM testing instrument has been fabricated by the Sensing, Imaging and Signal Processing group at the School of Electrical and Electronic Engineering at the University of Manchester [92] [93]. The FPGA-based instrument (Field Programmable Gate Array) shown in Figure 4.6 can operate from 5 kHz to 200 kHz, perform digital demodulation at the rate of 100 k/second and features an Ethernet communication to PC. The transmitting coil is excited by an alternating current generated by the FPGA board. The current is then converted by a digital to analogue converter (DAC) and subsequently amplified with a total gain of 0.8. For the receiving coil, the signal is amplified by a gain of 205.8. Afterwards, the signal is controlled by a PGA (Programmable Gain Amplifier) with a gain of 0.32 and then is fed into an analogue to digital converter (ADC). The driving current from the instrument is 48 mA rms (the current depends on the impedance of connecting sensor; this current is for the open T-R sensor). The amplified voltages on the pickup coil

are then acquired and recorded by a host PC. The instrument has been demonstrated to provide an SNR (Signal to Noise Ratio) of ~96 dB at frequently used frequencies (10 – 100 kHz). The high demodulation rate enables high speed data recording under the circumstance of imaging. In addition, the signal amplification improves the sensitivity of ECT, especially when the EM properties change is small in samples.

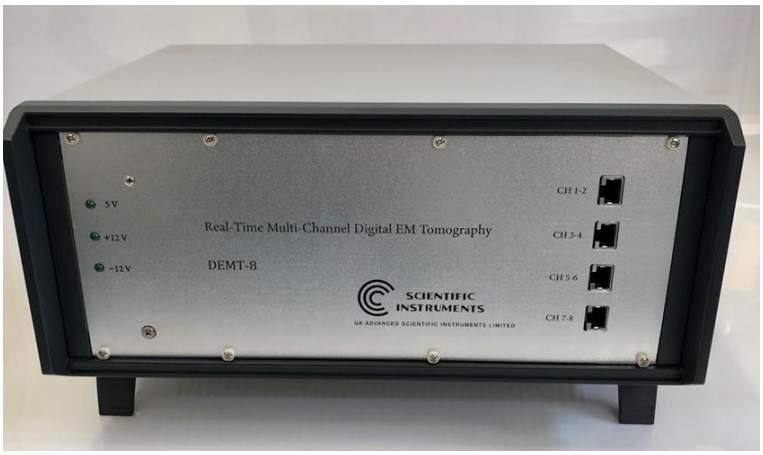

Figure 4.6 The picture of the custom designed EM inspection instrument.

4.5 Sensor Characterisation

4.5.1 Sensitivity

The performance of a cup-ferrite enclosed T-R sensor and a traditional open T-R sensor is evaluated.

4.5.1.1 FEM Simulation

Figure 4.7 illustrates the FEM model of traditional T-R sensor and cup-ferrite enclosed T-R sensor above ferrite material build in the ANSYS Maxwell. The sensors are in the same size as in Section 4.2. The effects of frequency and lift-off are displayed in Figure 4.8.

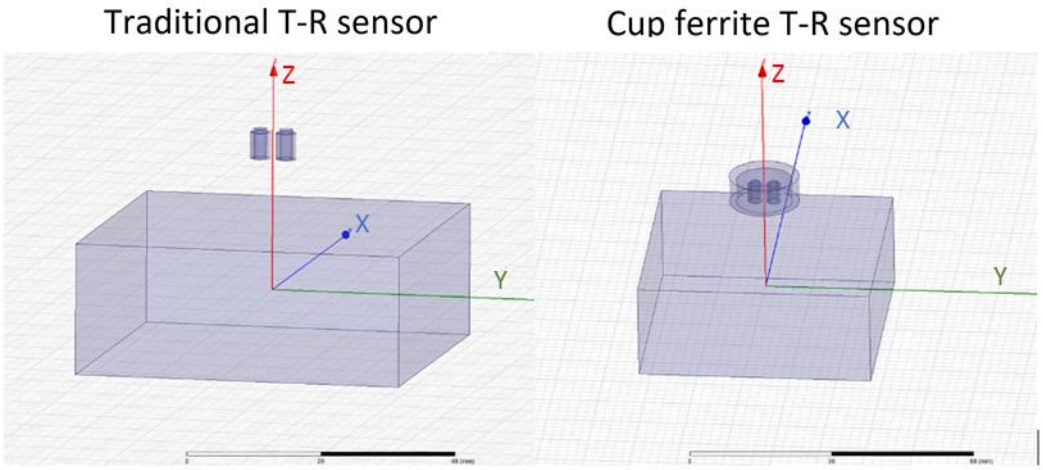

Figure 4.7 The FEM models for traditional T-R sensor and cup-ferrite T-R sensor in ANSYS Maxwell; The sensors are above a ferrite plate.

The negative sign of the mutual inductance can be ignored because of the opposite current direction for exciting and pickup coil settings in the simulation. At large lift-off where can be termed as free space (air), the cup-ferrite sensor has smaller mutual inductance than the traditional T-R sensor. The mutual inductance for both sensors peaks at a certain lift-off (when frequency is higher than 1 kHz). In addition, the peak lift-off increases while increasing frequency. The cup-ferrite sensor has a better sensitivity as shown in Figure 4.8 that the

cup-ferrite sensor has larger mutual inductance changes when the sensors approaching a sample from the air to the peak lift-off. It is also noticed that at extremely small lift-off, the traditional sensor has larger response to the sample. However, the extremely small lift-off is not applicable in real scanning scenarios.

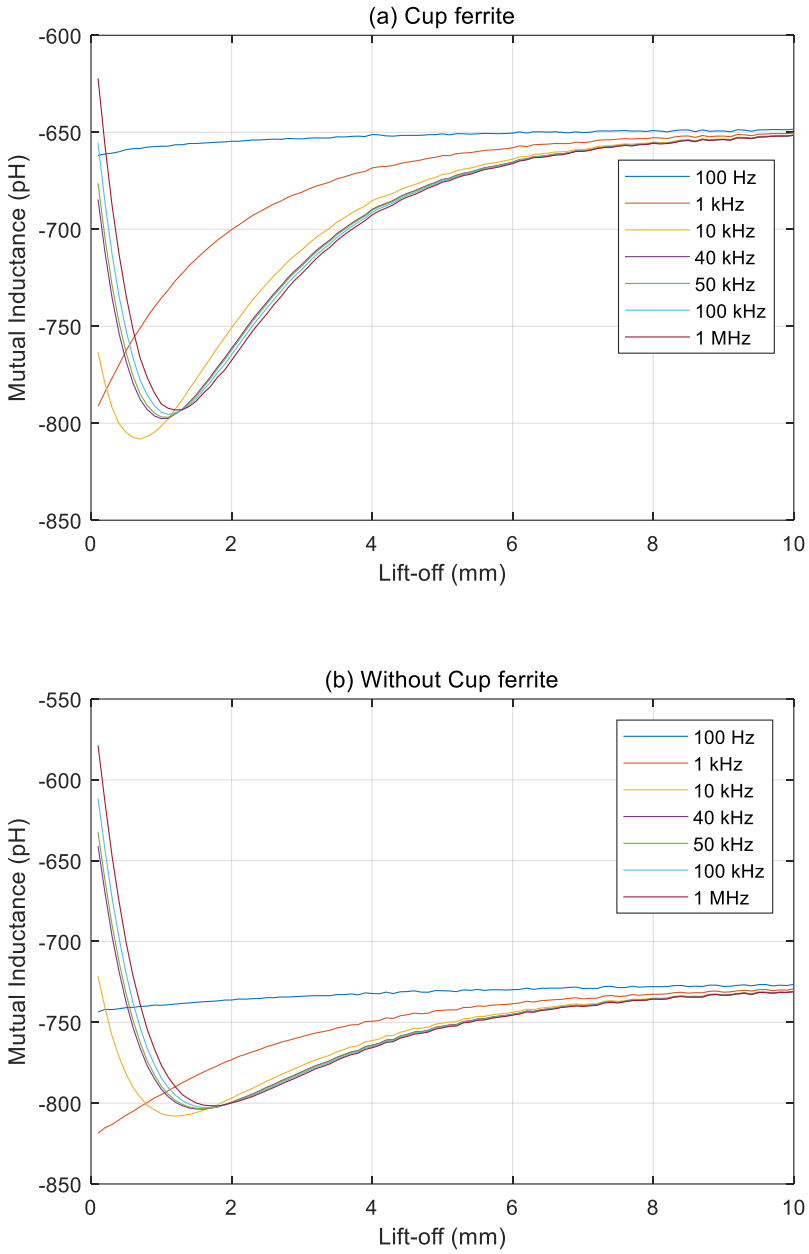

Figure 4.8 Mutual inductance of (a) Cup-ferrite sensor and (b) traditional T-R sensor. The figures illustrate the mutual inductance changes with lift-off and frequency.

4.5.1.2 Experiment

The frequency responses of two sensors were measured by the Impedance Analyser (SI1260) as indicated in Figure 4.9. The mutual inductance in free space is 70.3 μH for T-R sensor and 17.75 μH for cup-ferrite sensor. Their resonance frequencies are 631 kHz and 794.3 kHz respectively.

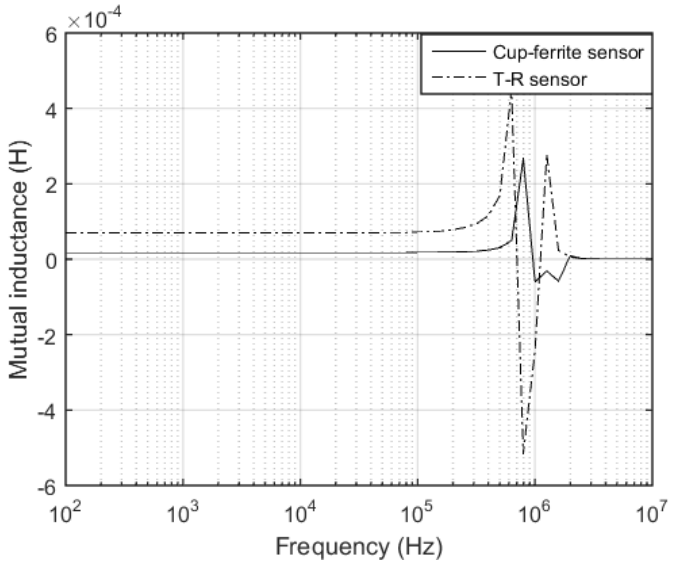

Figure 4.9 Mutual inductance of the T-R sensor and cup-ferrite sensor in the air measured by the Impedance Analyser (SI1260) with frequency sweeping from 10 – 10^7 Hz

Similar to the FEM simulation results, the T-R sensor has a stronger mutual coupling than the cup-ferrite sensor in free space. This could because the magnetic flux is distributed by the path between the ferrite cup and the coils.

4.5.2 Spatial Resolution

The spatial resolution of the sensor was tested with a custom-designed instrument described in Session 4.4. The sensor travels above a vertically placed ferrite rod as shown in Figure 4.10. The 0.75 mm diameter ferrite rod acts as a point simulation. A 40 kHz excitation frequency was employed.

A peak occurs as the sensor passing the ferrite rod as exhibited in Figure 4.11 and Figure 4.12. The signal represents the changes of imaginary part of the

impedance. A list of lift-offs is evaluated from 0.125 mm to 2.5 mm (Several sets are plotted in the figure), and the magnitude of signal decreases as the lift-off increases.

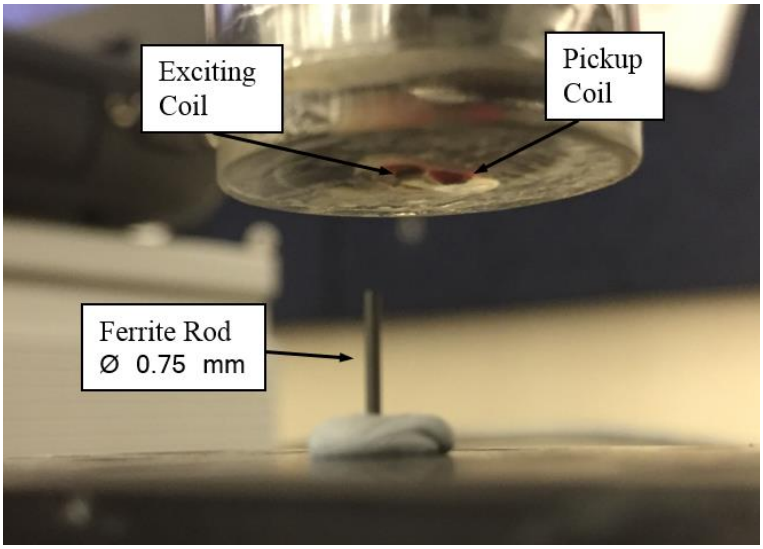

Figure 4.10 The picture of sensitive resolution setup, with T-R sensor and ferrite rod under tested.

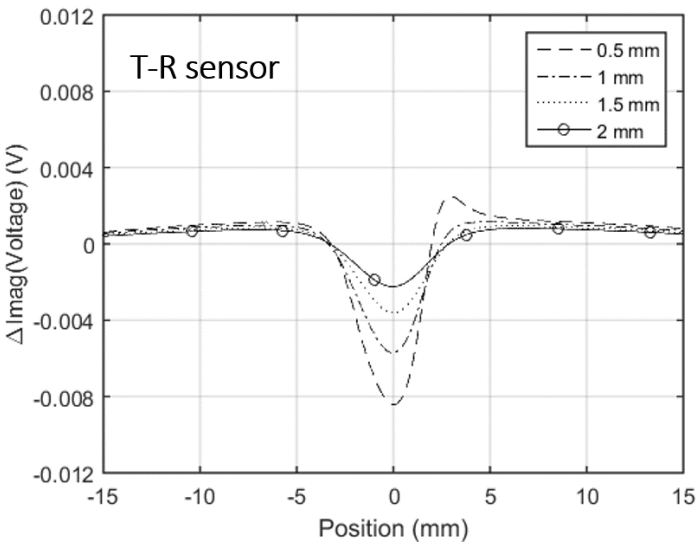

Figure 4.11 The spatial resolution curves of T-R sensor of different lift-offs with respect to 0.75 mm ferrite rod. Y-axis is the imaginary part of induced voltage with normalisation by subtracting the induced voltage in the air. The measurements were acquired by a custom-designed instrument under 40 kHz.

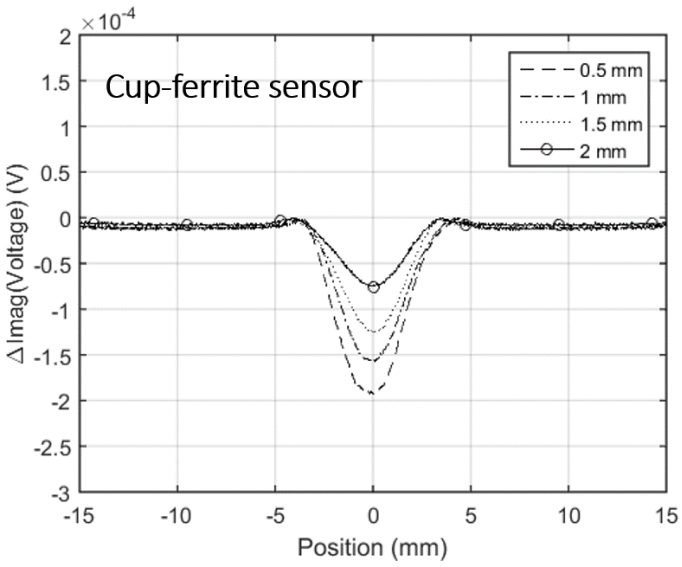

Figure 4.12 The spatial resolution curves of cup-ferrite sensor of different lift-offs with respect to the ferrite rod. Y-axis is the imaginary part of induced voltage with normalisation by subtracting the induced voltage in the air. The measurements were acquired by a custom-designed instrument under 40 kHz.

Table 4-2 The spatial resolution of T-R sensor and Cup-ferrite sensor

Lift-off (mm)		0.125	0.5	0.625	0.75	1	1.5	2	2.5
Resolution to ferrite rod diameter Ratio	T-R Sensor	3.243	3.876	4.332	4.813	6.560	8.259	9.120	9.300
	Cup Sensor	2.964	2.622	2.533	2.508	2.470	2.533	2.584	2.597

The spatial resolution of the sensor was defined as the magnitude of the response signal reached half of the peak magnitude. The ratio of resolution to ferrite rod diameter was then used to define the spatial performance. As exhibited in Table 4-2, the ratio of T-R sensor increases with increased the lift-off while the ratio of cup-ferrite sensor remains almost constant and relatively smaller. These experimental results prove that the ferrite cup is effective at improving the spatial resolution performance compared with a traditional open T-R sensor. The lift-off effects on spatial resolution can be ignored within a reasonable lift-off range using the cup-ferrite T-R sensor.

From Table 4-2, it can be seen that the resolution to ferrite rod diameter ratio is around 2.5 for the cup ferrite sensor. It stays relatively constant in a lift-off range of 0.5 mm – 2.5 mm.

4.6 Conductivity Invariance Phenomenon (CIP)

During the experimental evaluation of effects of lift-off and EM properties of test sample for the traditional T-R sensor (air core), a Conductivity Invariance Phenomenon (CIP) with a controlled lift-off is discovered and studied. Yu has proposed a permeability measurement device based on the CIP [94]. The measured results were proved to be accurate. The imperfection of this device is that it requires substrate metal on the top and bottom sides of sample, which is impractical in some applications.

The analytical solver introduced in section 3.2.2 is applied to validate the finding. The difference in the complex inductance is $\Delta L = L - L_A$, where the coil inductance above a plate is L, and L_A is the inductance in free space. The simulations were computed on ThinkStation P510 platform with Dual Intel Xeon E5-2600 v4 Processor, with 16G RAM. And the experimental data was achieved by Impedance analyser SL 1260.

Figure 4.13 illustrates both the analytical and experimental data of the inductance variance with respect to σ_0 (conductivity of brass sample 15.9 MS/m) versus lift-offs with the same excitation frequency of 90 kHz. It can be clearly seen that the inductance curve for all samples almost overlap at a lift-off of approximately 1.9 mm. Zooming in, the inductance curves overlap at multiple points for all the models, but the overlapped points are very close to each other.

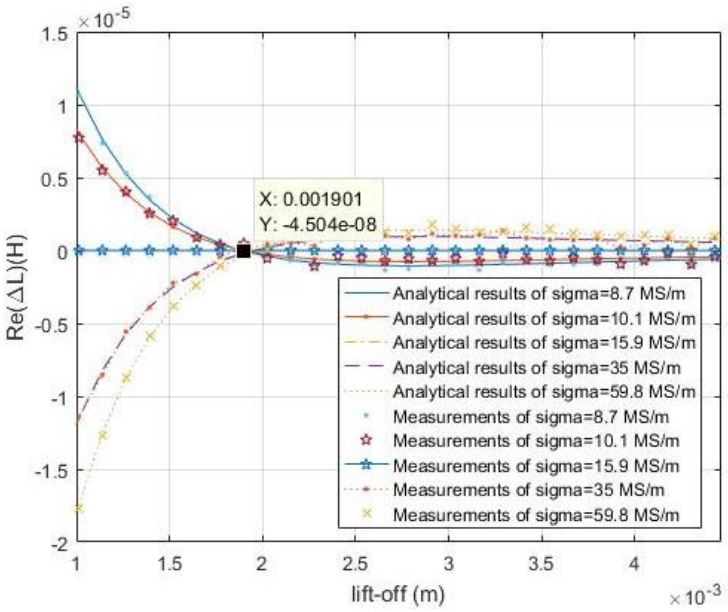

Figure 4.13 Analytical and experimental data of given samples inductance variance with respect to brass sample (conductivity of brass sample is 15.9 MS/m).

Since the analytic solution is proved to be accurate enough when compared to the experimental data, the influence of conductivity range, excitation frequency, and sample thickness is analysed as follows.

4.6.1 Influence of Conductivity Range

In a small conductivity range, the inductance curves for different conductivities overlap. The range effects on the CIP are investigated. Therefore, a series of models with conductivity ranging from 40% to 160% of (conductivity of brass sample 15.9 MS/m) were simulated. And the Conductivity Invariance Lift-off in this range is calculated to be 1.896 mm when the average value of inductance variance has reached its minimum value as shown in Figure 4.14.

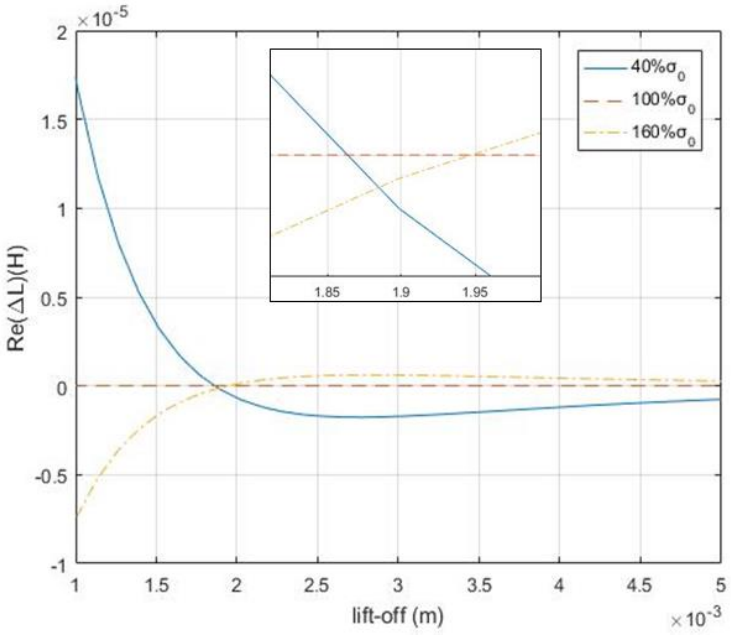

Figure 4.14 Analytical data of 40% σ_0, 100% σ_0, and 160% σ_0 inductance variance with respect to brass sample

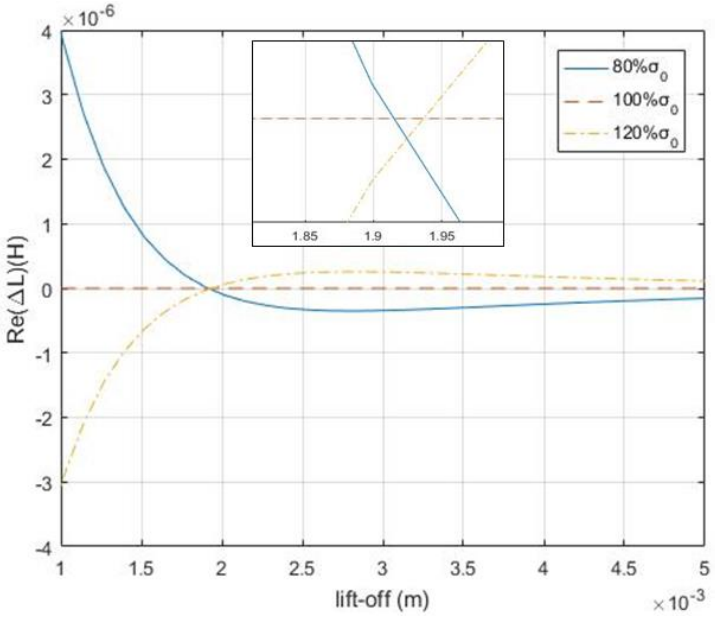

Figure 4.15 Analytical data of 80% σ_0, 100% σ_0, and 120% σ_0 inductance variance with respect to brass sample

Table 4-3 Inductance variance of samples with different conductivity under the Conductivity Invariance Lift-off

Conductivity (% of σ_0)	ΔL (H)	$\Delta L / L(\sigma_0, l_0)$
40	-2.007E-7	0.627%
60	-2.576E-9	0.008%
80	2.118E-8	0.066%
100	0	0
120	-3.284E-8	0.103%
140	-6.891E-8	0.215%
160	-1.023E-7	0.320%

In Table 4-3, ΔL denotes Inductance Variance compared to σ_0 under the Conductivity Invariance Lift-off l_0 . $\Delta L / L(\sigma_0, l_0)$ represents Inductance Variance bp (basis point - per ten thousand) related to inductance of σ_0 under the Conductivity Invariance Lift-off l_0 .

It can be clearly seen from Figure 4.14, Figure 4.15, and Table 4-3 that conductivity with wide range will result in larger average value of inductance variance related to 100% σ_0 (15.9 MS/m) for all conductivity samples within the range. And at a certain range, the conductivity at the proposed Conductivity Invariance Lift-off has little influence on the inductance. As can be seen from Table 4-3 that the inductance relative variance under a conductivity range from 40% to 160% is less than 0.0063% compared to σ_0 case. In addition, the gap between the multiple overlapped points will be enlarged for wider conductivity ranges, which will result in larger inductance relative variances under the

corresponding Conductivity Invariance Lift-off.

4.6.2 Influence of Excitation Frequency

Figure 4.16 exhibits the inductance variance with respect to σ_0 (15.9 MS/m) versus lift-offs under excitation frequencies of 80, 90, and 100 kHz. These frequencies are commonly used frequencies for ECT. Besides it will enable better SNR considering the corresponding experiment. It can be clearly seen that a higher excitation frequency will result in larger Conductivity Invariance Lift-off, which is affected by the skin effect. In addition, the inductance variance compared to 100% σ_0 under the corresponding Conductivity Invariance Lift-off is much reduced under the higher excitation frequency.

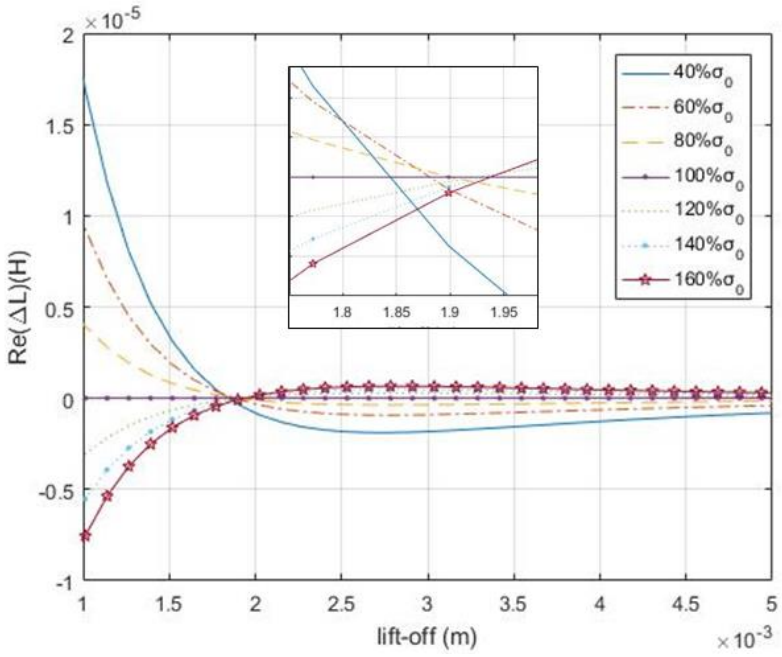

(a)

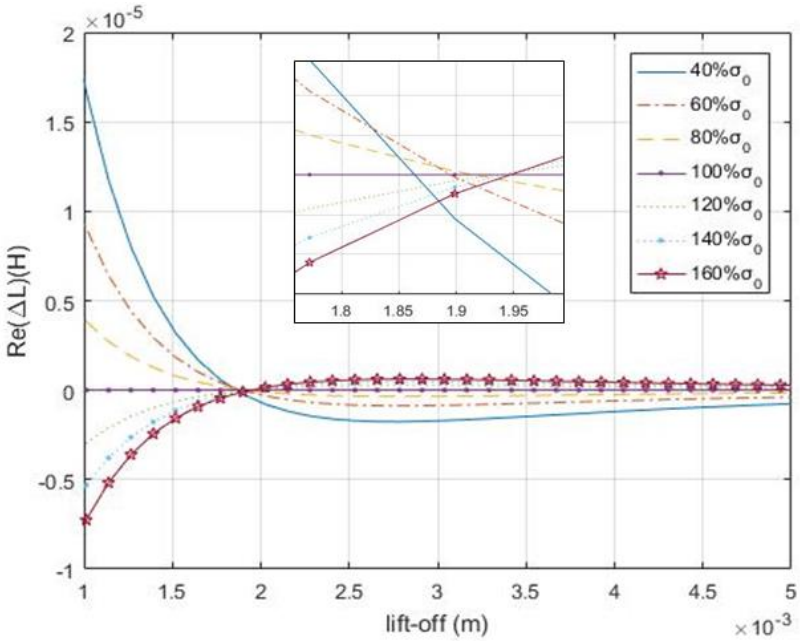

(b)

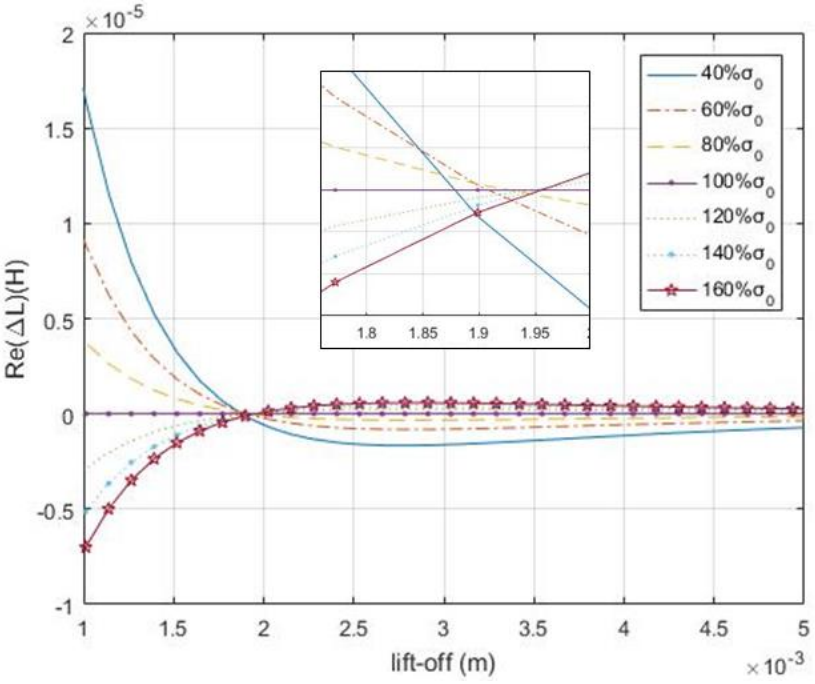

(c)

Figure 4.16 Analytical results of given samples inductance variance with respect to brass sample under different excitation frequencies (a) 80 kHz (b) 90 kHz (c) 100 kHz.

4.6.3 Influence of Sample Thickness

Figure 4.17 shows the inductance variance with respect to σ_0 (15.9 MS/m) versus lift-offs under a same excitation frequency of 90 kHz but different

sample thickness (a series of 0.5 mm, 5 mm and 10 mm). It can be clearly seen from (b) and (c) that the inductance curves are almost immune to the thickness of the sample when the thickness of sample is large enough that the eddy current would not penetrate the plate. In addition, the skin depth range of $40\%\sigma_0$ ~ $160\%\sigma_0$ samples is from 0.333 mm to 0.665 mm. The thickness of case (a) is 0.5 mm, which is amid the skin depth range of given samples. Therefore, the eddy current would penetrate some plate samples in case (a) and the inductance curve of these plate samples in case (a) would differ from that of case (b) and (c). In conclusion, thinner samples (when thickness is smaller than the skin depth of given samples) will result in larger Conductivity Invariance Lift-off. Meanwhile, the inductance variance compared to 100% σ_0 under the corresponding Conductivity Invariance Lift-off is much increased when sample thickness is smaller than its skin depth.

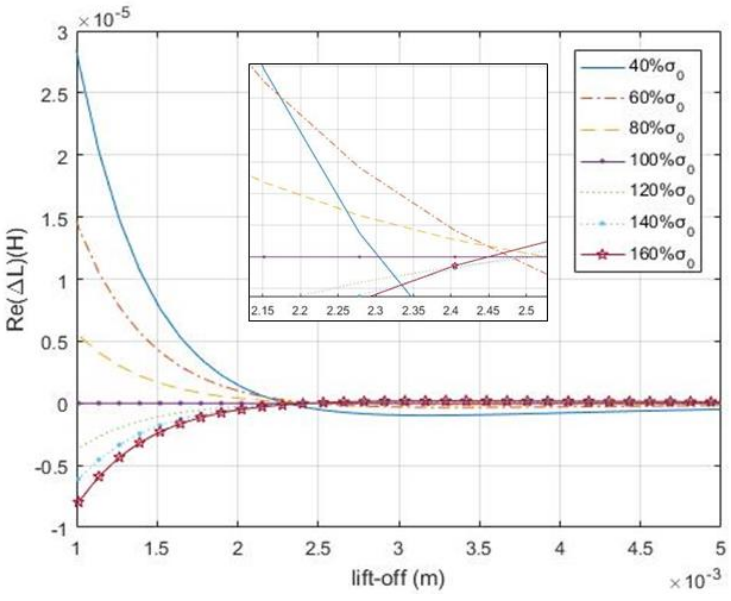

(a)

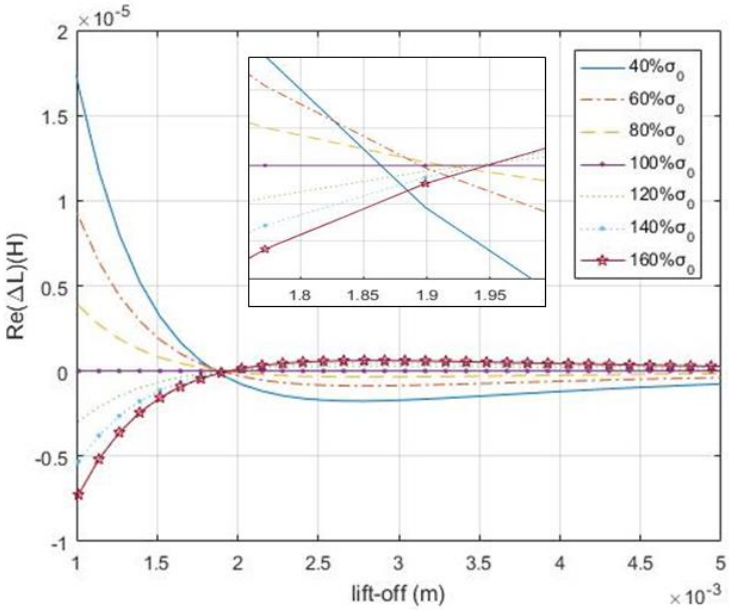

(b)

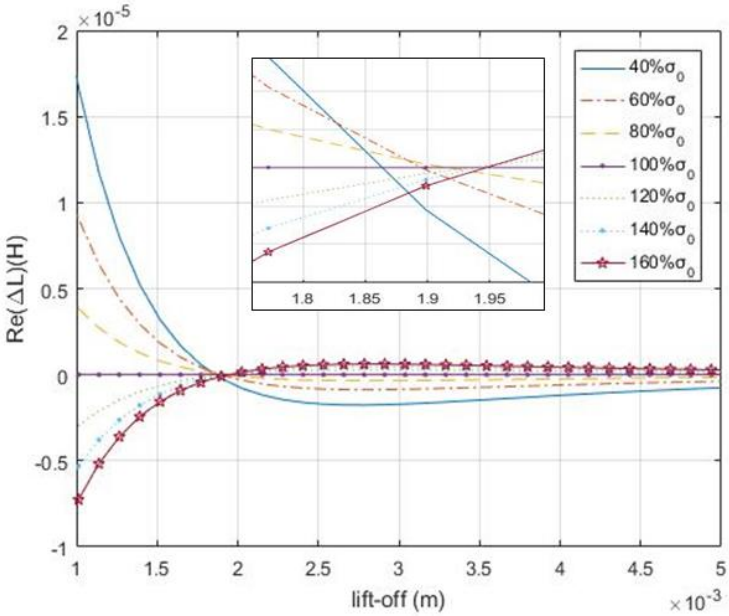

(c)

Figure 4.17 Analytical results of given samples inductance variance with respect to brass sample under different plate thickness (a) 0.5 mm (b) 5 mm (c) 10 mm.

If $\mathrm{L}(\sigma, l)$ represent the inductance of sample with an electrical conductivity σ and lift-off l , then we can find a specific lift-off l_0 that $\sum_{i=0}^{4} \Delta \mathrm{L}(\sigma_i, l_0) = \sum_{i=0}^{4} \left(\mathrm{L}(\sigma_i, l_0) - \mathrm{L}(\sigma_0, l_0) \right)$ has reached its minimum value ($\sigma_0 \ldots \sigma_4$

denotes conductivity of brass, tin, iron, aluminium and copper respectively). The reason why these samples are chosen is because these metals are readily available and have relative permeability of 1. In addition, these metals offer a reasonable range of conductivity which covers target practical applications. Since the conductivity has little influence on the inductance change at this overlapped lift-off, termed as the Conductivity Invariance Lift-off, is an ideal sensor position that can be used for the permeability measurement.

In practice, we could not get the accurate conductivity profiles of the tested samples such as some alloy steel strip (or even under the oxide coating condition). In addition, the conductivity profiles of some steel strip such as steels with high thermal conductivity values are very sensitive to the environmental temperature. Fortunately, under this controlled lift-off (Conductivity Invariance Lift-off), the reconstruction of samples permeability profiles can almost immune to the influence of inaccurate samples conductivity profiles.

The analytical solution based on the Dodd and Deeds method has been widely applied to solve the impedance calculations of samples with infinite dimensions in x and y directions. However, the Dodd and Deeds analytical solution can also be valid for samples with finite dimensions in x and y if its dimensions in x and y is much larger than the region of the magnetic flux produced by the sensor and therefore the edge of sample would not influence the magnetic flux distributions within the samples in a significant way.

4.6.4 Effect of Test Sample Dimension

Figure 4.18 shows the x – z cross-section of the magnetic vector potential magnitude for a 100% σ_0 sample simulated by the analytical solution given in Equation 3-44 under 90 kHz. The maximum width of the region where the magnetic vector potential is not negligible is 0.0046 m. And the magnitudes of the vector potential beyond this band are all nearly zeros. Therefore, the sample plates used in our test (20 mm) can be treated as infinite plates and calculated using the Dodd and Deeds method. In general, when the plate is 5 times larger than the sensor, it can be treated as infinite without introducing significant errors. For similar reasons, in many finite element solvers, the padding region is normally 3–5 times larger than the actual sensor sizes.

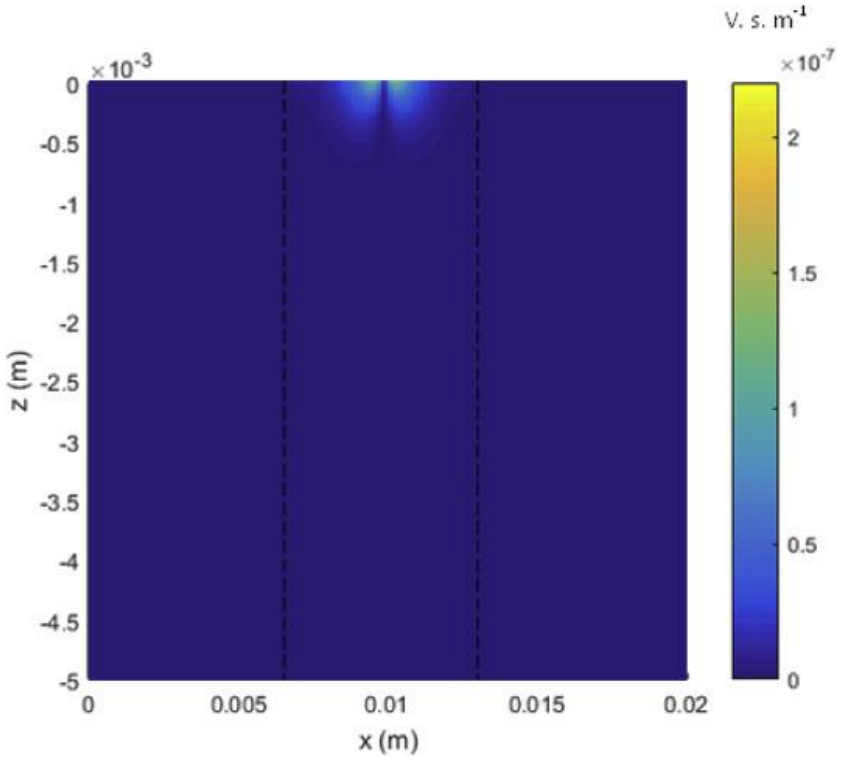

Figure 4.18 Magnitude of vector potential in x – z plane.

4.7 Permeability Measurement Based on CIP

Since both the electrical conductivity and permeability can affect the tested inductance [95] [96] [97]. It is very hard to estimate the sample's permeability in the NDT inverse problem, due to the coupling impact of the sample's electrical conductivity and permeability. Fortunately, we have found a lift-off that model's conductivity has little influence on the output signal (mutual inductance of the sensor). Therefore, the proposed Conductivity Invariance Lift-off can be used for the metallic sample's permeability measurement. The principle of samples permeability measurement is adjusting the permeability profile in the analytical solver so that the analytical values would be fitted well with that of measurement under the same samples, sensors, excitation current, and lift-offs. To verify the feasibility of this permeability measurement method using Conductivity Invariance Lift-off, a series of numerical simulations were carried out for some Dual-phase steel (DP steel) samples under a excitation frequency of 90 kHz and same planar dimensions of A4 size and thickness of 1.4 mm. The probe with same dimensions as in Table 4-1 is located on its Conductivity Invariance Lift-off of 1.9 mm and its neighbours. A comparison of permeability calculated by both Conductivity Invariance Lift-off and its neighbours is shown in Table 4-4.

Table 4-4 A comparison of given samples permeability calculated by both Conductivity Invariance Lift-off and its neighbours

Lift-offs	Relative permeability calculated by the lift-off			Actual relative permeability			Relative error for the relative permeability calculated by the lift-off (%)		
	DP-600	DP-800	DP-1000	DP-600	DP-800	DP-1000	DP-600	DP-800	DP-1000
1.3	202	118	99	220	140	120	-8.18	-15.71	-17.50
1.5	208	124	105	220	140	120	-5.45	-11.43	-12.50
1.7	213	131	113	220	140	120	-3.18	-6.43	-5.83
1.9 (Conductivity Invariance Lift-off)	222	144	122	220	140	120	0.91	2.86	1.67
2.1	227	148	127	220	140	120	3.18	5.71	5.83
2.3	234	156	134	220	140	120	6.36	11.43	11.67
2.5	241	164	143	220	140	120	9.55	17.14	19.17

The DP steel samples have different parameters as: DP600 steel (with an electrical conductivity of 4.13 MS/m and relative permeability of 220 ± 1.5), DP800 steel (with an electrical conductivity of 3.81 MS/m and relative

permeability of 140 ± 1.3), and DP1000 steel (with an electrical conductivity of 3.80 MS/m and relative permeability of 120 ± 1.2). At different lift-offs, the calculated permeability varies largely for each steel. It can be seen that the calculated permeability is the most accurate at the Conductivity Invariance Lift-off (1.9 mm). It is 2.86% for DP800, 1.67% for DP1000 and 0.91% for DP600.

4.8 Summary

The study of traditional sensor shows that the non-axial sensor has better spatial resolution than the co-axis sensor. In addition, a novel proposed cup ferrite enclosed T-R sensor significantly improves the spatial resolution which is less affected by the lift-off. Despite the ferrite cup reduces the coupling effect between the transmitter and pickup coils, the sensitivity of the cup ferrite T-R sensor is improved. The sensor applies a frequency range of up to 794.3 kHz (resonance frequency), which suits most welding inspection requirements.

A novel permeability measurement approach based on a Conductivity Invariance Lift-off is investigated, which can tackle the solution uniqueness problem caused by the coupling impact of the sample's electrical conductivity and magnetic permeability in the inverse problem. And both simulation and experimental data have verified that the conductivity has little influence on the mutual inductance change when probes are assigned with the proposed Conductivity Invariance Lift-off. In addition, the effect of conductivity range, excitation frequency, and samples thickness on the proposed Conductivity Invariance Lift-off are all. Finally, a comparison of permeability calculated by different lift-offs (both Conductivity Invariance Lift-off and its neighbours) is exhibited for the performance of the proposed permeability measurement

method based on the Conductivity Invariance Lift-off. And the proposed approach is proved can accurately estimate the permeability (with an error of 2.86 %) without the influence of its conductivity.

Chapter 5 Imaging of Weld Cross-section

Experiments are carried out for a weld cross-section of high strength steel API X70, which is widely used in pipeline. The weld sample is introduced in this chapter, including its macrograph, microstructure information and hardness data measured by Vickers micro-hardness test. The designed sensor introduced in Section 4.3 and the custom designed EM instrument introduced in Section 4.4 are used for the EM data measuring. The imaging results presented in Section 5.3 are published on NDT & E International [98]. The results in Section 5.4 are published to INSIGHT [99]. There are co-authors that contributed to the weld sample's preparation and hardness test.

5.1 Sample Preparation

Thick section steel welds are widely used in oil and gas industries, where the structural member requires high tensile strength, good low temperature toughness, high deformability and corrosion resistance. The BM used was API X70 steel rolled to a 26.8 mm $\times$ 200 mm $\times$ 1 m thick plate. The material was joined by a multi-electrode SAW approach with double 'V' groove. The consumable electrodes used were 4 mm in diameter. The welding parameters are giving in Table 5-1. The groove angle was 70° for both backing and finishing sides. The sample was the cross-section extracted from the welding joint as shown in Figure 5.1. The weld cross-section sample gives the dimensions of 49 mm traverse (X-axis), 9 mm longitude (Z-axis), and 26.8 mm height (Y-axis) [100]. The surface of the specimen was ground for metallography and hardness testing.

Table 5-1 SAW input parameters and weld dimensions.

Weld	Groove depth (mm)	FZ width (mm)	Welding speed (mm/min)	Heat input (kJ/mm)	Arc power (kW)
Backing	9.5	13.5	1600	4.44	188.40
Finishing	11.0	15.3	1470	5.97	146.27

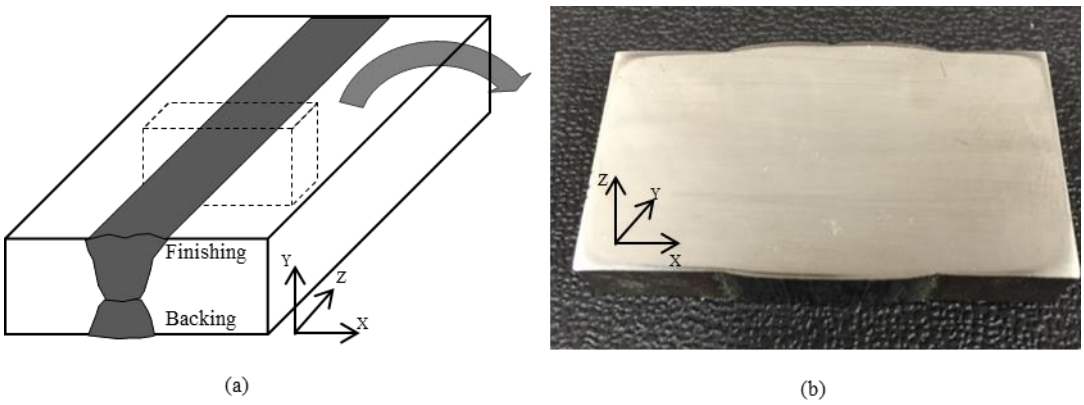

Figure 5.1 (a) Schematic of SAW thick plate with finishing and backing bead contour. The steel dimensions are 26.8 mm × 200 mm × 1 m; (b) picture of the weld cross-section sample extracted from the SAW API X70 steel as illustrated in (a). The specimen dimensions are 49 mm traverse (X-axis), 9 mm longitude (Z-axis), and 26.8 mm height (Y-axis).

5.1.1 Macrograph and Hardness

Macrograph of the sample is taken to evaluate the weld conditions and dimensions such as penetration depth, bead height, and width of weld zones. Hardness investigations on weld cross-section are useful in several ways / scenarios. During a welding process, the metal microstructure experiences complex transformation which is controlled by adjusting welding parameters such as heat input, welding speed, component size and temperature, etc. Depending on these parameters, steels can develop different microstructure phases such as ferrite, austenite, martensite and bainite which all exhibit different hardness values. The weld sample employed for this study was mapped using a Vickers indenter and a 1 kg load, with an inter-indent spacing of approximately 1 mm, all hardness values obtained conformed to ASTM E384-10/ISO 6507.

Figure 5.2 (a) shows the macrograph of the weld cross-section, a small weld crown (<2.5 mm) on the finishing weld was obtained. The FZ has a width of 15.34 mm. Figure 5.2 (b) shows the hardness map obtained spanning all regions of the weld. The areas of the weld are apparent, including the WN, FZ, and HAZ. Specifically, moving from the weld centerline out to the base metal, the WN has a hardness between 230-220 HV1, the FZ is demarked by a drop from 220 to 200 HV1, and the HAZ with a hardness of 200-180 HV1.

Hardness values are obtained by preparing a metallographic surface to a sufficient degree such that indentations can be readily measured. Therefore, increasing level of surface preparation is required to obtain smaller indents, and by virtue, a higher resolution. Micro-hardness testing can, however, produce a reasonable degree of information, albeit with discrete values which must be interpolated over.

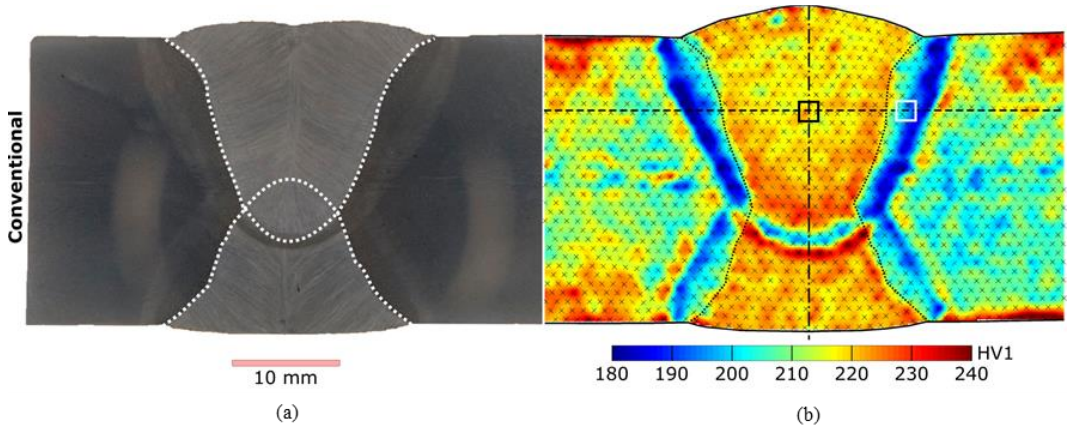

Figure 5.2 (a) The macrograph of the weld cross-section, dotted lines indicate the weld metal boundaries; (b) the hardness map of the sample; black crosses indicate hardness measurement point locations; and the squares indicate the location of micrographs in Figure 5.3.

5.1.2 Micrograph

Figure 5.3 illustrates the micrograph of weld metal and HAZ of the finishing weld. The locations of where they were taken are indicated in Figure 5.2. The microstructure of the WN is fine, acicular ferrite, which then turns to bainite in

the HAZ immediately adjacent to the fusion boundary. Regions of high hardness (e.g. the bottom of the WN) are attributed to carbon segregation induced by the back-to-back welding procedure. The obtained microstructure is typical of welds performed in this class of steel.

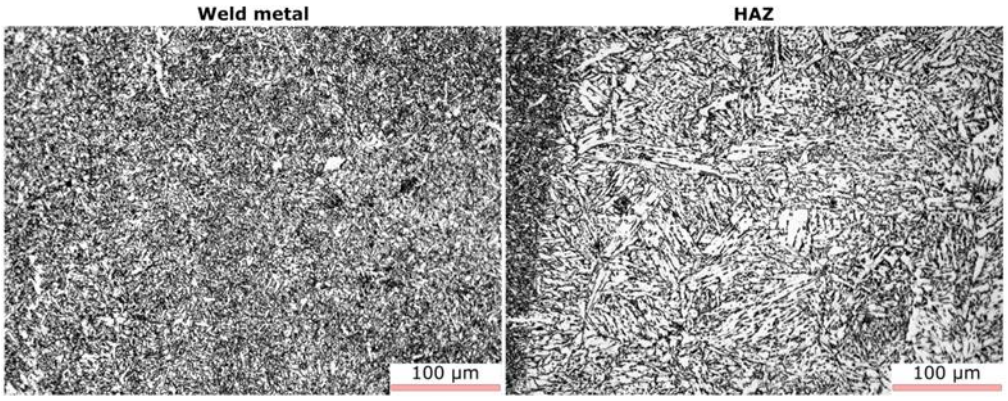

Figure 5.3 Micrographs of weld metal (left) and HAZ (right) of the weld (adapted from [100]). The locations from which the micrographs were taken are indicated in Figure 5.2.

5.2 Imaging Procedure

The image scanning is operated by a programmable C scan stage from Newmark systems Inc. USA as shown in Figure 5.4 (a). The stage consists of two stepper motors to drive X and Y axis which sit on a breadboard base. The base and X and Y axis of the stage were installed with the aid of a computer numerical control (CNC) machine to ensure orthogonality to within 10 μm over the full length of travel. The stage can provide a scanning speed of up to 100 mm/s with a 200 mm travel length and a 0.2 μm resolution. During scanning, the weld specimen was attached to the platform and was moved in the workspace of the stage. The EM sensor is mounted onto a height adjustable gauge bar, which had an accuracy of 8 μm. Therefore, the stage is well suited for scanning small sized specimens with good spatial accuracy. The scanning area and path is controlled by an Arduino-based controller board from a host PC.

For the weld specimen, the scanning direction is illustrated in Figure 5.4 (b). The excitation and pickup coils were aligned to be parallel with X-axis. The sensor scans across the weld specimen in X-axis, and returns backwards after stepping down in Y-axis, rastering in this direction. In this scanning method, a detailed surface image can be obtained in 6 minutes with an X and Y resolution of 0.019 mm × 0.5 mm (Determined by motor scanning steps and instrument data transmission speed).

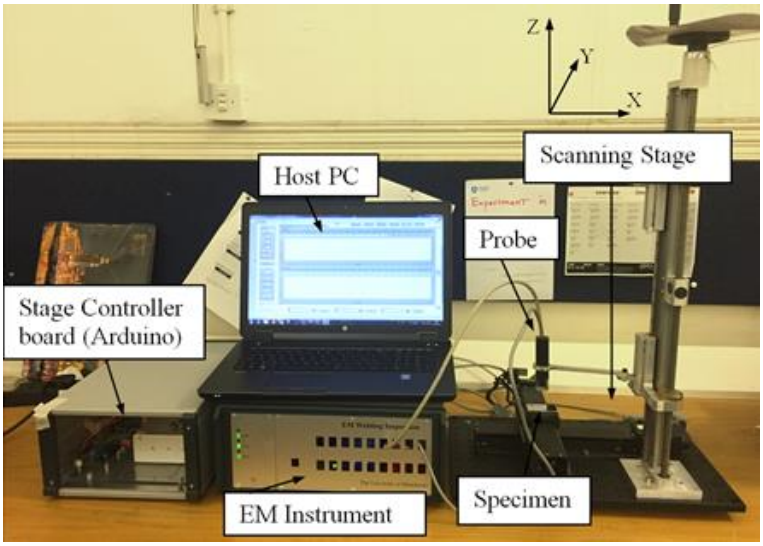

(a)

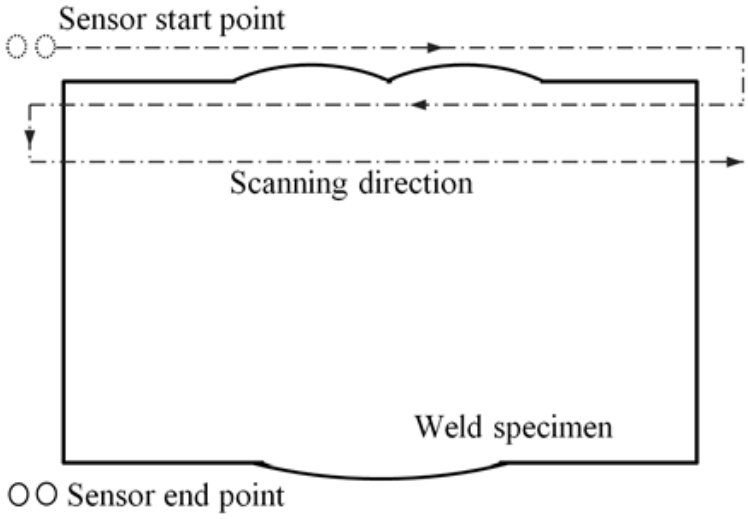

(b)

Figure 5.4 (a) The picture of setup of experimental system with EM instrument, scanning stage, host PC, stage driver system, EM probe and tested specimen; (b) the diagram of scanning, shows the sensor arrangement, scanning path and sensor starting and ending position.

5.3 EM Imaging with Inductance

The real and imaginary parts of EM images are illustrated in Figure 5.5. The contours of the weld specimen, including WN, FZ, HAZ and the base metal can be identified clearly in Figure 5.5 (d). The estimated dimensions of the weld specimen are 49.36 mm × 26.5 mm as found by EM scanning. This is a departure of 0.7% in the X-axis and 1.1% for the Y-axis when compared to the actual sample sizes.

By comparing Figure 5.5 (a) and (b), the real part image gives more identifiable details of weld structures than imaginary part. Theoretically, for steel, which is both electrical and magnetic conductive, real part of EM measurements is mainly attributed to the eddy current losses, which is related to the conductivity of tested sample, while the imaginary part is mainly determined by the permeability of the steel. During the welding process, the microstructure and grain size mainly change the permeability; the conductivity is similar between WN, FZ, HAZ and BM. After calibration, the phase of the EM signals can be corrected as shown in Figure 5.5 (c) and (d). The imaginary impedance has a much larger magnitude than the real impedance.

The signal response of HAZ is larger than BM and FZ. As high imaginary impedance indicates higher permeability on the weld specimen, we can deduce that larger permeability corresponds to lower hardness, which is consistent with previous studies. The large responses occurred at the center of the EM images is related to the increased hardness at the intersection of WN. Overall the EM imaging results correlate well with the hardness map as shown in Figure 5.2 (b).

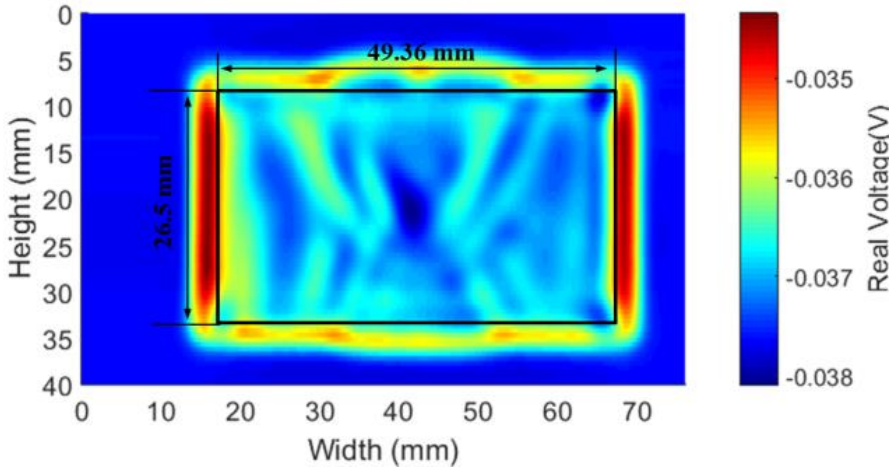
49.36 mm
26.5 mm
Height (mm)
Width (mm)
Real Voltage(V)
-0.035
-0.036
-0.037
-0.038

(a)

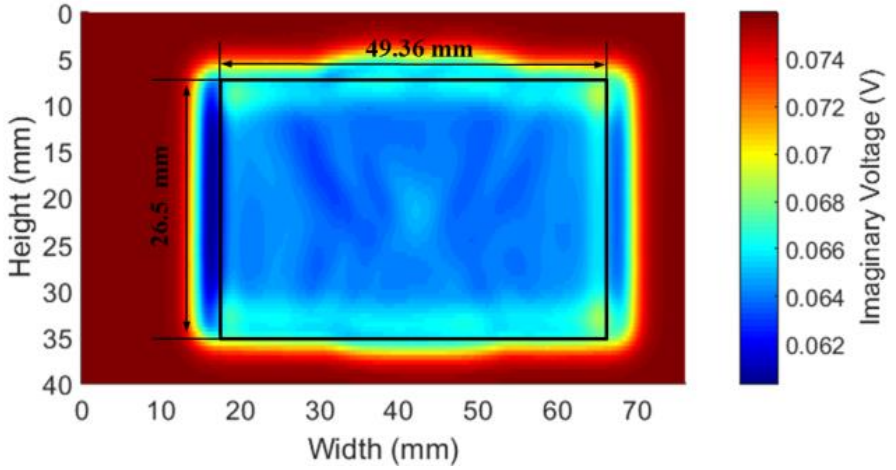
49.36 mm
26.5 mm
Height (mm)
Width (mm)
Imaginary Voltage (V)
0.074
0.072
0.07
0.068
0.066
0.064
0.062

(b)

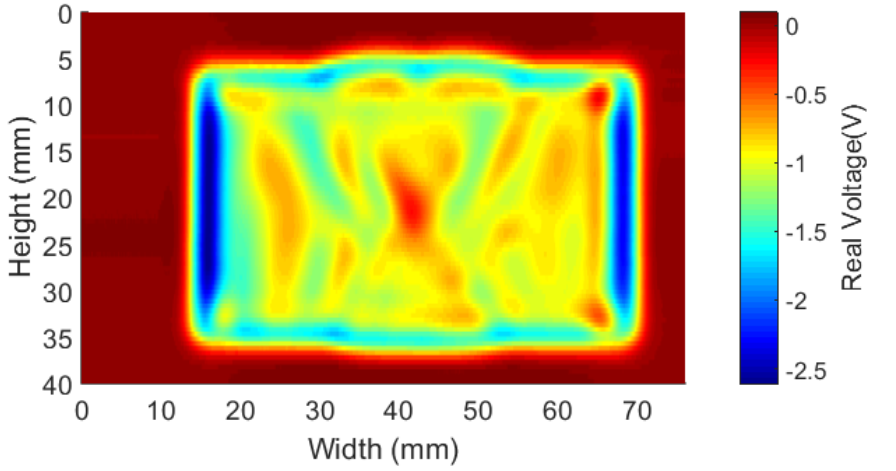
Height (mm)
Width (mm)
Real Voltage(V)
0
-0.5
-1
-1.5
-2
-2.5

(c)

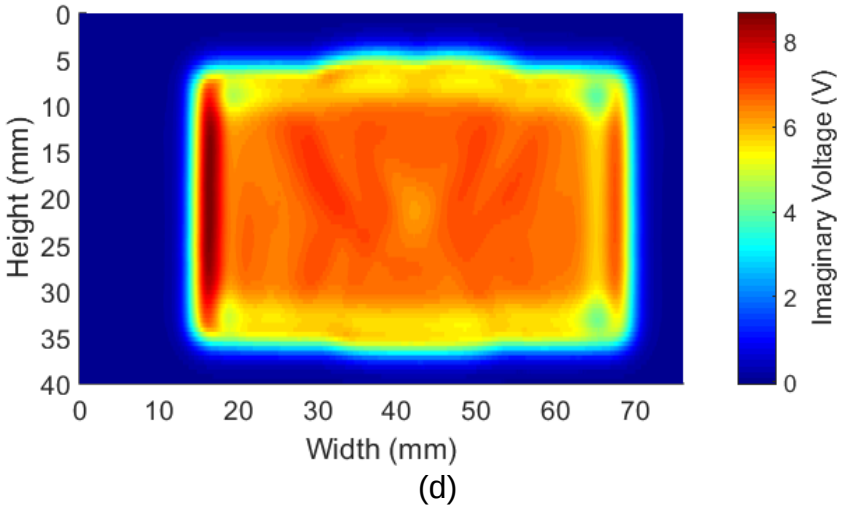

Figure 5.5 EM images of the weld specimen with 40 kHz excitation frequency, and circumstance of 0.5 mm lift-off (a) and (b) are EM images with the air boundaries when the sensor is out of the specimen; (c) and (d) are EM images of the specimen extracted from (a) and (b), also with calibration applied; X-axis and Y-axis display the width and height of the scanning; (a), (c) and (b), (d) exhibit the images of real parts and imaginary parts respectively. The contour of the weld specimen is clearly defined, and the estimated dimensions are 49.36 mm × 26.5 mm for 0.5 mm lift-off.

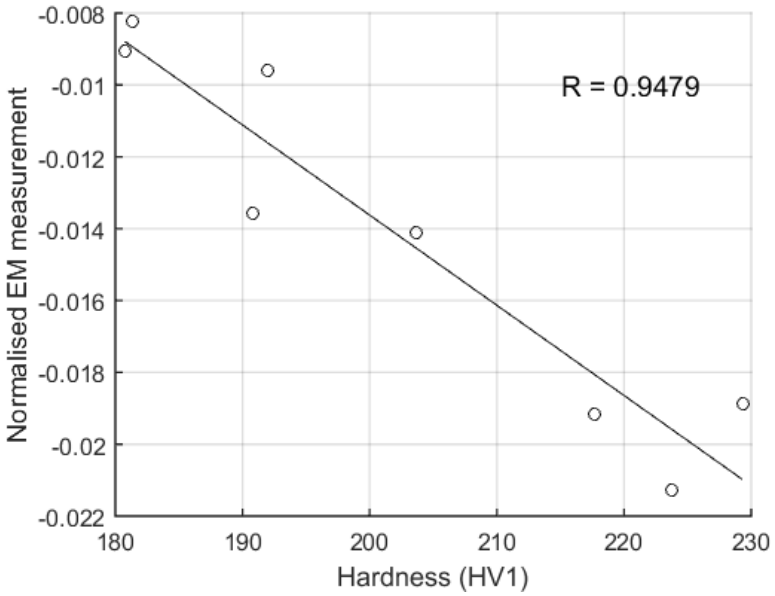

Figure 5.6 The correlation between EM signals and hardness at same locations, which are picked randomly in BM, WN, FZ and HAZ.

A quantified comparison between EM signals and hardness are shown in Figure 5.6. The locations of the data points were randomly picked in BM, WN, FZ and HAZ. The result shows a linear correlation between the hardness and EM properties. The correlation coefficient between EM signal and hardness is 0.9479.

5.4 EM Imaging with Offset-Crossing Frequency

In this section, sweeping frequency is used to test the weld cross-section. A novel frequency feature (the frequency at which the real part of the inductance reaches a specified value) is proposed for imaging.

5.4.1 Crossing Frequency Feature

With the presence of a test sample, the changes in complex mutual inductance of the sensor are defined as

Equation 5-1

$$\mathrm{Re}(\Delta \mathrm{L}) = \mathrm{Re}(\frac{\mathrm{Z}(\omega)-\mathrm{Z}_{\mathrm{air}}(\omega)}{\mathrm{j}\omega})$$

Equation 5-2

$$\mathrm{Im}(\Delta \mathrm{L}) = \mathrm{Im}(\frac{\mathrm{Z}(\omega)-\mathrm{Z}_{\mathrm{air}}(\omega)}{\mathrm{j}\omega}),$$

where $\mathrm{Z}(\omega)$ donates the mutual impedance of the sensor with presence of test sample, and $\mathrm{Z}_{\mathrm{air}}(\omega)$ donates the mutual impedance when the sensor is in free space (air). For material such as ferritic steel, which is both electrical and magnetic conductive, $\mathrm{Re}(\Delta \mathrm{L})$ reflects the mutual inductance changes due to both effects, i.e. eddy current and magnetisation. The induced eddy current would generate a secondary magnetic field that resists the primary magnetic field from the transmitting coil. Meanwhile the magnetisation due to the magnetic permeability of steel will strengthen the primary magnetic field. Hence the mutual inductance of the T-R sensor is increased by magnetisation and simultaneously decreased by the effect of eddy current.

To provide physical insight to the new crossing frequency feature proposed in this section, we start from air cored co-axial T-R sensor. The complex mutual

inductance for an air-cored T-R sensor can be determined as shown in Equation 5-3 [79] [101] [102], which can also be find in Section 3.2.1.

Equation 5-3

$$\Delta L(\omega) = K \int_0^\infty A\phi(\alpha) d\alpha$$

Equation 5-4

$$\phi(\alpha) = \frac{(\alpha_1+\mu_r\alpha)(\alpha_1-\mu_r\alpha)-(\alpha_1+\mu_r\alpha)(\alpha_1-\mu_r\alpha)e^{2\alpha_1 c}}{-(\alpha_1-\mu_r\alpha)(\alpha_1-\mu_r\alpha)+(\alpha_1+\mu_r\alpha)(\alpha_1+\mu_r\alpha)e^{2\alpha_1 c}}$$

Equation 5-5

$$\alpha_1 = \sqrt{{\alpha_0}^2 + j\omega\sigma\mu_r\mu_0}.$$

A denotes magnitude that is independent of the thickness and the electromagnetic properties of the sample. Kdenotes a constant value that is related to the dimensions and turns of coils. μ_0 denotes the permeability of free space. μ_r denotes the relative permeability of sample. σ denotes the conductivity of sample. c denotes the thickness of sample. α_0 denotes the spatial frequency which is related to the geometry parameters of the sensor. The sensor phase signature is solely determined by the permeability, conductivity, the thickness of the tested sample, and spatial frequency. It reaches its maximum at a characteristic spatial frequency α_0 (introduced in Section 3.2.1). The $\phi(\alpha_0)$ can be taken outside of the integral, it is described as shown in Equation 5-6. The Equation 5-3 becomes Equation 5-7.

Equation 5-6

$$\phi(\alpha_0) = \frac{1-\sqrt{1/{\mu_r}^2+j\omega\sigma\mu_0/\mu_r{\alpha_0}^2}}{1+\sqrt{1/{\mu_r}^2+j\omega\sigma\mu_0/\mu_r{\alpha_0}^2}},$$

Equation 5-7

$$\Delta L(\omega) = \phi(\alpha_0)\Delta L_0,$$

where $\Delta L_0 = K \int A \, d\alpha$ is the amplitude of the signal which is strongly dependent on the coil geometrical parameters but independent of the thickness and electromagnetic properties of the tested sample.

Neglect $1/{\mu_r}^2$ when μ_r is much larger than 1,

Equation 5-8

$$\phi(\alpha_0) = \frac{1-\sqrt{j\omega\sigma\mu_0/\mu_r{\alpha_0}^2}}{1+\sqrt{j\omega\sigma\mu_0/\mu_r{\alpha_0}^2}}.$$

Assigning $\omega_0 = \frac{\mu_r{\alpha_0}^2}{\mu_0\sigma}$,

Equation 5-8 can be rewritten as

Equation 5-9

$$\phi(\alpha_0) = \frac{1-\sqrt{j\omega/\omega_0}}{1+\sqrt{j\omega/\omega_0}}.$$

The real part of $\phi(\alpha_0)$ equals zero when $\omega = \omega_0$ and $\phi(\alpha_0)$ determines the phase of ΔL, hence the zero-crossing frequency for the first order system is approximately ω_0.

Based on Equation 5-7 and Equation 5-9, $\mathrm{Re}(\Delta \mathrm{L})$ can be described as

Equation 5-10

$$\mathrm{Re}(\Delta \mathrm{L}) = \Delta L_0 \cdot \frac{-\sqrt{2}\sqrt{\frac{\omega}{\omega_0}}}{\frac{\omega}{\omega_0}+\sqrt{2}\sqrt{\frac{\omega}{\omega_0}}+1}.$$

When $\mathrm{Re}(\Delta \mathrm{L})$ crosses a specific value, ω can be derived as shown in Equation 5-11 as below,

Equation 5-11

$$\omega = T \cdot \frac{\mu_r{\alpha_0}^2}{\mu_0\sigma},$$

where

Equation 5-12

$$T = \frac{\left[\sqrt{2}\mathrm{Re}(\Delta L)/\Delta L_0 + \sqrt{2} \pm \sqrt{-2\left(\frac{\mathrm{Re}(\Delta L)}{\Delta L_0}\right)^2 + 4(\mathrm{Re}(\Delta L)/\Delta L_0) + 2}\right]^2}{4(\mathrm{Re}(\Delta L)/\Delta L_0)^2}.$$

Here ω is proportional to μ_r whereat a specific value of $\mathrm{Re}(\Delta L)$.

The real and imaginary parts of complex inductance are demonstrated in Figure 5.7 with the presence of steel sample described below. $\mathrm{Re}(\Delta L)$ crosses zero at 12.5 kHz. By selecting the crossing value of $\mathrm{Re}(\Delta L)$, the range of crossing frequency can be adjusted. The value of $\mathrm{Re}(\Delta L)$ is defined as the crossing offset. The offset-crossing frequency can be potentially used to evaluate the permeability distribution of a test sample.

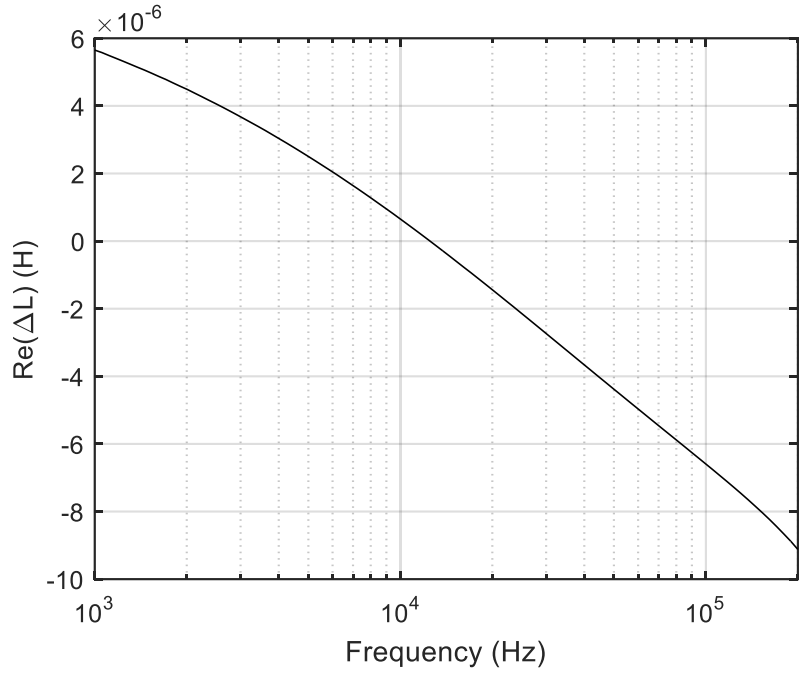

(a)

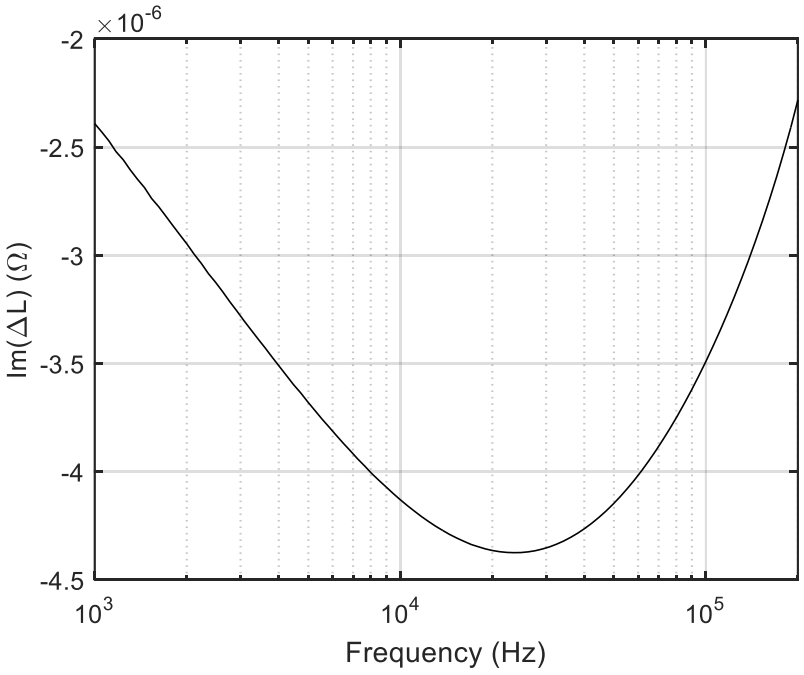

(b)

Figure 5.7 (a) Real part and (b) imaginary part of complex inductance, tested on the X70 sample with 1 mm lift-off.

5.4.2 Offset-Crossing Frequency Image

The resulted offset-crossing frequency images are shown in Figure 5.8. In general, the shape and contour of the WN and HAZ is clearer. The range of

the frequency imaging data is much large than that of the impedance data, indicating a higher sensitivity to EM properties. As indicated in the derivations in previous sections, the images are a better indication of permeability change. The images all reveal surface information of the sample. The frequency range increases as the $\mathrm{Re}(\Delta \mathrm{L})$ value increases. When $\mathrm{Re}(\Delta \mathrm{L})$ is set to 1.7×10^{-5}, the frequency range is beyond 20 kHz, the images become clearer. This is partly related to the performance of the sensor and the instrument because at this frequency range, the instrument has a higher SNR. All the offset-crossing frequency images show good consistency with the macrograph and hardness of the sample as shown in Figure 5.2.

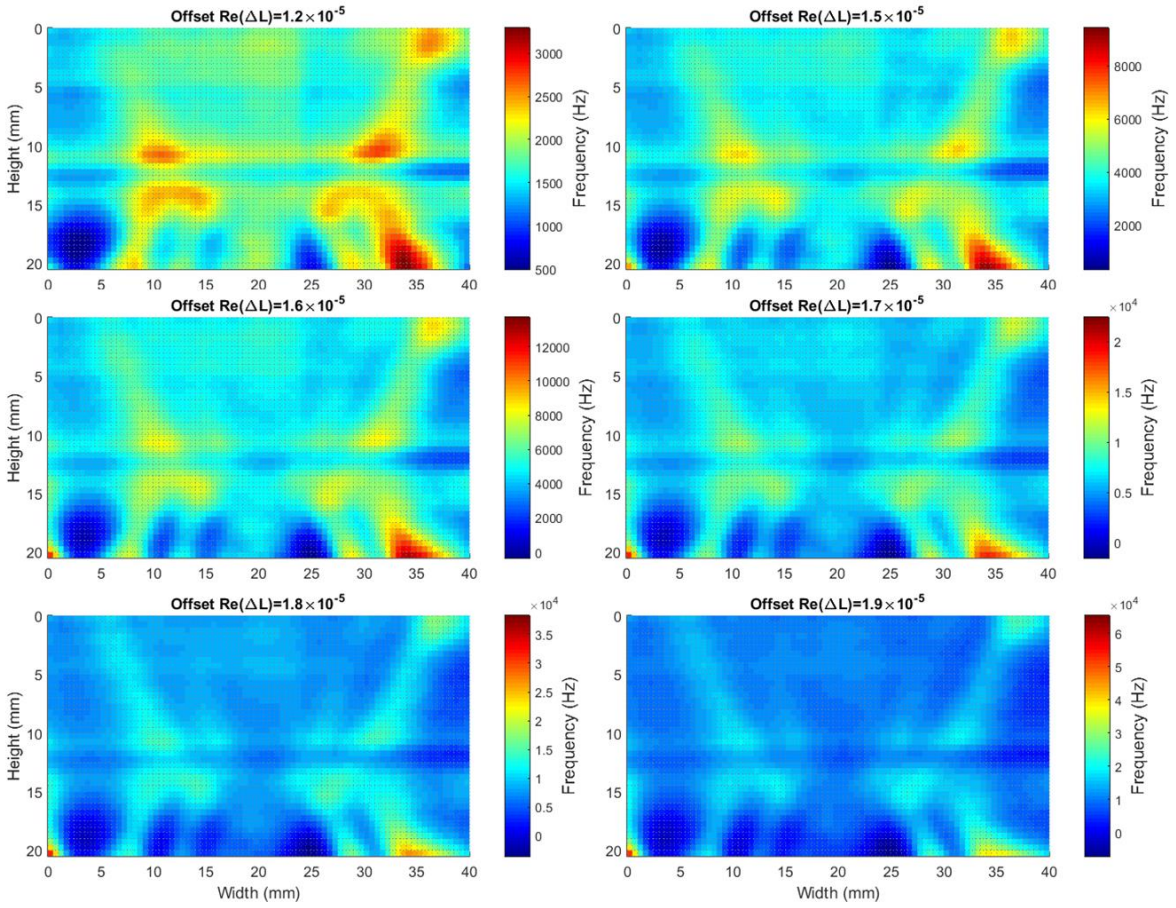

Figure 5.8 Images of the weld cross-section, reconstructed by offset-crossing frequency with Re(ΔL) offset from 1.2×10^{-5} to 1.9×10^{-5}.

5.4.3 Relationship Between Offset-Crossing Frequency and Hardness

The comparison of the two X70 cross-section images by the means of offset-crossing frequency and hardness is illustrated in Figure 5.9. The contours of FZ, HAZ are drawn along the outlines in Figure 5.9 (a). The frequency image has great consistency comparing to the hardness image with insignificant distortion caused by the eddy current edge effect. And the image contrast can be physically approved by improving the sensor spatial resolution.

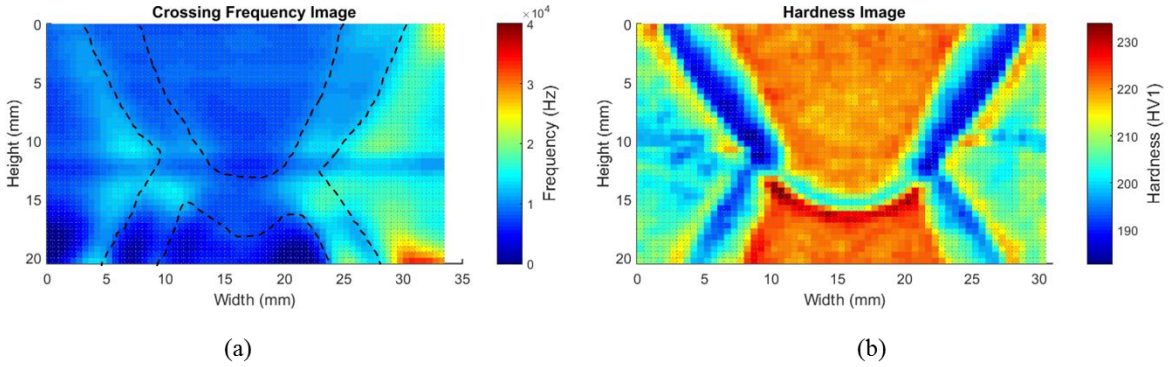

Figure 5.9 Images of the X70 cross-section sample reconstructed by (a) offset-crossing frequency, the dotted lines indicate the boundary of weld metal and HAZ; and (b) hardness map (Same as Figure 5.2 (b)).

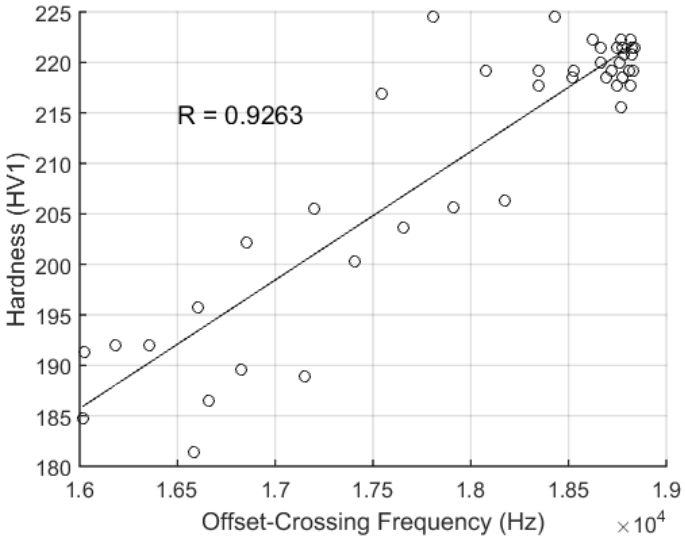

Figure 5.10 Correlation of zero-crossing frequency and hardness data at a position of 4 mm away from the top of the image.

As shown in Figure 5.10, offset-crossing frequency is linear proportional to the hardness with a correlation coefficient of 0.9263.

5.5 Summary

An experimental scanning method using a cup-ferrite sensor has been devised to image the EM properties X70 steel SAW cross-section sample. The EM images were compared with a corresponding hardness map of the weld sample. A calibration was applied to the EM signal responses from a custom-designed EM instrument. These images show good correlation with the hardness map and metallurgical information of the weld cross-section. The estimated weld sample sizes from the EM images have an error of 1.1% compared to the actual size.

An approximate linear relationship was found between the EM signal and the hardness of SAW of X70 steel. The scanning method can serve as a complementary tool for hardness test without the need for sophisticated surface preparation. In the future, considering a weighted point spread function, an approximate hardness map could be inferred directly by an EM sensor.

In addition, a novel frequency feature (the frequency at which the real part of the inductance reaches a specified value) is proposed for imaging an X70 welding cross-section. It is derived that this frequency feature is related to the permeability of the sample and therefore the imaging results obtained from this feature is a reflection of the electromagnetic properties (in particular permeability) map of the sample. The resulted images are then compared with the weld macrograph and hardness map. The shape and contour of three weld

zones (fusion zone, heat affected zone, and base metal) can be identified. This novel imaging method has a high sensitivity to microstructure changes and by adjusting the inductance value it crosses; the frequency range can be adjusted to suit a particular instrument capability.

Chapter 6 Conclusion

6.1 Summary

The major work carried out in this research is to design an EM weld imaging method. An imaging system has been successfully manufactured through integrating an EM measurement instrument, an EM sensor and a scanning stage. The EM images of a weld cross-section obtained by the system show good consistency with the hardness mapping and macrograph of the sample. This method provides a non-destructive method for weld inspection.

The research work includes:

i. The design of EM sensor
    - FEM simulations have been carried out for the structures of sensor, effects of operating frequency, and lift-off.
    - Analytical solutions of air-cored sensor have been adopted which can evaluate the effects of sensor parameters.
    - Experiments have been carried out to characterise the performance of the sensor.

ii. The manufacture of the imaging system
    - EM sensor
    - Scanning stage
    - Custom-designed EM measurement instrument

iii. Weld inspection in the lab
    - Evaluate the detectability of the X70 weld sample
    - Image the weld cross-section by C-scan

- Evaluate the system's stability for online welding inspection

The main findings and results of the research are summarised as below:

i. The FEM simulation results of both co-axial and non-axial EM sensors indicate that the non-axial sensor possesses better spatial resolution. The spatial resolution is improved by increasing the operating frequency.

ii. The experimental results of cup-ferrite enclosed T-R sensor indicate that a ferrite cup can improve the spatial resolution without sacrificing the sensitivity. With the help of the ferrite cup, the spatial resolution can stay relatively constant in a lift-off range of 0.5 mm to 2.5 mm.

iii. During the experimental evaluation of lift-off effect of the non-axial T-R sensor, a CIP with a controlled lift-off is discovered. The phenomenon shows that at certain lift-off, the effects of a sample's conductivity on the sensor's response is reduced.

iv. A permeability estimation method based on the CIP has been applied on dual phase steels. The results show that the method can improve the accuracy of permeability estimation (2.86%) without the influence of the steels' conductivity.

v. In the experiments of weld cross-section, the imaging results from the proposed EM method show clearly different weld zones. The EM images through the impedance and frequency feature all indicate good consistency with the hardness map and macrograph of the sample. This finding shows a linear relationship between the EM measurements and hardness measurements.

vi. The EM method using the frequency feature enables the adjustment of frequency range to suit a particular instrument capability, that can potentially improve the SNR.

6.2 Future Work

To develop the EM method for off-line weld inspection and fulfil online welding testing, further research is required.

For off-line weld inspection:

- Evaluate the EM imaging method for other welding samples, such as aluminium alloys and dissimilar metals.
- Due to the limitation of ferrite core, winding wire diameters and ferrite cup shape and size, the current sensor performance can be further improved. An optimisation in sensor design is needed in future work, for example, the spatial resolution can be further improved by decreasing the gap distance between the excitation and pickup coils.
- Post imaging processing method can be evaluated. A numerical method can be developed to improve the spatial resolution based on eddy current distribution underneath the sensor.
- Based on the relationship between hardness measurements and EM data, a hardness estimation method for weld can be investigated based on EM data. This may require a large amount of data base.

For online welding testing:

- Large sizes of sensor are desired for online weld inspection that can improve the sensitivity and increase the detectable lift-off.
- The performance of the EM sensor is worth investigating with thermal effect.
- Design the mounting device to install the EM sensor onto the welding equipment that the sensor can detect the potential defects of the weld simultaneously during welding process.

REFERENCES

1. G. D. Goodfellow, C.J.L.a.J.V.H., *UKOPA Pipeline Product Loss Incidents and Faults Reports (1962 - 2017)*. 2019, United Kingdom Onshore Pipeline Operators' Association.
2. John, V., *Testing of Materials*. 1992: Macmillan Publishers Limited.
3. Hughes, S.E., *Chapter 6 - Non-destructive and Destructive Testing*, in *A Quick Guide to Welding and Weld Inspection*, S.E. Hughes, Editor. 2009, Woodhead Publishing. p. 67-87.
4. Ditchburn, R.J., S.K. Burke, and C.M. Scala, *NDT of welds: state of the art.* NDT & E International, 1996. **29**(2): p. 111-117.
5. Kim, N.J. and G. Thomas, *Effects of morphology on the mechanical behavior of a dual phase Fe/2Si/0.1C steel.* Metallurgical Transactions A, 1981. **12**(3): p. 483-489.
6. Kim, Y.M., H. Lee, and N.J. Kim, *Transformation behavior and microstructural characteristics of acicular ferrite in linepipe steels.* Materials Science and Engineering: A, 2008. **478**(1): p. 361-370.
7. Guo, W., et al., *Comparison of microstructure and mechanical properties of ultra-narrow gap laser and gas-metal-arc welded S960 high strength steel.* Optics and Lasers in Engineering, 2017. **91**: p. 1-15.
8. Lin, H., et al., *Effect of cooling conditions on microstructure and mechanical properties of friction stir welded 7055 aluminium alloy joints.* Materials Characterization, 2018. **141**: p. 74-85.
9. Bhadeshia, H. and R. Honeycombe, *Chapter 8 - Heat Treatment of Steels: Hardenability*, in *Steels: Microstructure and Properties (Fourth Edition)*, H. Bhadeshia and R. Honeycombe, Editors. 2017, Butterworth-Heinemann. p. 217-236.
10. Rao, B.P.C., et al., *An artificial neural network for eddy current testing of austenitic stainless steel welds.* NDT & E International, 2002. **35**(6): p. 393-398.
11. Koyama, K., H. Hoshikawa, and N. Taniyama. *Investigation of eddy current testing of weld zone by uniform eddy current probe*. in *Proceedings of WCNDT*. 2000.
12. Weman, K., *1 - Arc welding – an overview*, in *Welding Processes Handbook*, K. Weman, Editor. 2003, Woodhead Publishing. p. 1-25.
13. Weman, K., *19 - The weldability of steel*, in *Welding Processes Handbook (Second Edition)*, K. Weman, Editor. 2012, Woodhead Publishing. p. 191-206.
14. Chandel, R.S., H.P. Seow, and F.L. Cheong, *Effect of increasing deposition rate on the bead geometry of submerged arc welds.* Journal of Materials Processing Technology, 1997. **72**(1): p. 124-128.
15. Muthupandi, V., et al., *Effect of weld metal chemistry and heat input on the structure and properties of duplex stainless steel welds.* Materials Science and Engineering: A, 2003. **358**(1): p. 9-16.
16. Gery, D., H. Long, and P. Maropoulos, *Effects of welding speed, energy input and heat source distribution on temperature variations in butt joint welding.* Journal of Materials Processing Technology, 2005. **167**(2): p. 393-401.

17. Murugan, N. and V. Gunaraj, *Prediction and control of weld bead geometry and shape relationships in submerged arc welding of pipes.* Journal of Materials Processing Technology, 2005. **168**(3): p. 478-487.
18. Weman, K., *8 - Pressure welding methods*, in *Welding Processes Handbook*, K. Weman, Editor. 2003, Woodhead Publishing. p. 80-92.
19. Weman, K., *11 - Pressure welding methods*, in *Welding Processes Handbook (Second Edition)*, K. Weman, Editor. 2012, Woodhead Publishing. p. 119-132.
20. El-Banna, M., D. Filev, and R.B. Chinnam, *Automotive Manufacturing: Intelligent Resistance Welding*, in *Computational Intelligence in Automotive Applications*, D. Prokhorov, Editor. 2008, Springer Berlin Heidelberg: Berlin, Heidelberg. p. 219-235.
21. Besharati Givi, M.K. and P. Asadi, *1 - General introduction*, in *Advances in Friction-Stir Welding and Processing*, M.K.B. Givi and P. Asadi, Editors. 2014, Woodhead Publishing. p. 1-19.
22. Houldcroft, P. and R. John, *Chapter 9 - Gas welding and cutting*, in *Welding and Cutting*, P. Houldcroft and R. John, Editors. 1988, Woodhead Publishing. p. 155-169.
23. Weman, K., *2 - Gas welding*, in *Welding Processes Handbook*, K. Weman, Editor. 2003, Woodhead Publishing. p. 26-30.
24. Houldcroft, P. and R. John, *Chapter 1 - Background and scope*, in *Welding and Cutting*, P. Houldcroft and R. John, Editors. 1988, Woodhead Publishing. p. 1-10.
25. Houldcroft, P. and R. John, *Chapter 2 - Principles of arc welding*, in *Welding and Cutting*, P. Houldcroft and R. John, Editors. 1988, Woodhead Publishing. p. 11-39.
26. Weman, K., *7 - Submerged arc welding*, in *Welding Processes Handbook*, K. Weman, Editor. 2003, Woodhead Publishing. p. 68-79.
27. Weman, K., *9 - Other methods of welding*, in *Welding Processes Handbook*, K. Weman, Editor. 2003, Woodhead Publishing. p. 93-101.
28. Bhadeshia, H. and R. Honeycombe, *Chapter 1 - Iron and Its Interstitial Solutions*, in *Steels: Microstructure and Properties (Fourth Edition)*, H. Bhadeshia and R. Honeycombe, Editors. 2017, Butterworth-Heinemann. p. 1-22.
29. Bhadeshia, H. and R. Honeycombe, *Chapter 13 - Weld Microstructures*, in *Steels: Microstructure and Properties (Fourth Edition)*, H. Bhadeshia and R. Honeycombe, Editors. 2017, Butterworth-Heinemann. p. 377-400.
30. Bhadeshia, H. and R. Honeycombe, *Chapter 7 - Acicular Ferrite*, in *Steels: Microstructure and Properties (Fourth Edition)*, H. Bhadeshia and R. Honeycombe, Editors. 2017, Butterworth-Heinemann. p. 203-216.
31. Hughes, S.E., *Chapter 8 - Codes, Standards and Documentation*, in *A Quick Guide to Welding and Weld Inspection*, S.E. Hughes, Editor. 2009, Woodhead Publishing. p. 108-124.
32. Shull, P.J., *Nondestructive evaluation: theory, techniques, and applications*. 2002: CRC press.
33. Petroleum, N., *natural gas industries Materials for use in H2S-containing environments in oil and gas production.* Part. **1**: p. 15156-1.

34. Pressure, A., *Qualification Standard for Welding and Brazing Procedures, Welders, Brazers, and Welding and Brazing Operators*. 2010: American Society of Mechanical Engineers.
35. Beidokhti, B., A.H. Koukabi, and A. Dolati, *Effect of titanium addition on the microstructure and inclusion formation in submerged arc welded HSLA pipeline steel.* Journal of Materials Processing Technology, 2009. **209**(8): p. 4027-4035.
36. Hashemi, S.H. and D. Mohammadyani, *Characterisation of weldment hardness, impact energy and microstructure in API X65 steel.* International Journal of Pressure Vessels and Piping, 2012. **98**: p. 8-15.
37. Halmshaw, R., R. Honeycombe, and P. Hancock, *Non-destructive testing*. 1991: Arnold.
38. Liao, T.W. and J. Ni, *An automated radiographic NDT system for weld inspection: Part I — Weld extraction.* NDT & E International, 1996. **29**(3): p. 157-162.
39. Liao, T.W. and Y. Li, *An automated radiographic NDT system for weld inspection: Part II—Flaw detection.* Ndt & E International, 1998. **31**(3): p. 183-192.
40. Wang, G. and T.W. Liao, *Automatic identification of different types of welding defects in radiographic images.* NDT & E International, 2002. **35**(8): p. 519-528.
41. Liao, T.W., *Improving the accuracy of computer-aided radiographic weld inspection by feature selection.* NDT & E International, 2009. **42**(4): p. 229-239.
42. Banks, B., *Ultrasonic flaw detection in metals: theory and practice*. 1962: Iliffe Books.
43. Firestone, F.A., *The supersonic reflectoscope, an instrument for inspecting the interior of solid parts by means of sound waves.* The Journal of the Acoustical Society of America, 1946. **17**(3): p. 287-299.
44. Firestone, F.A. and J.R. Frederick, *Refinements in supersonic reflectoscopy. Polarized sound.* The Journal of the Acoustical Society of America, 1946. **18**(1): p. 200-211.
45. Firestone, F.A., *Flaw detecting device and measuring instrument*. 1942, Google Patents.
46. Gao, H., et al. *Ultrasonic inspection of partially completed welds using EMAT-generated surface wave technology*. in *2015 IEEE Far East NDT New Technology & Application Forum (FENDT)*. 2015.
47. Yang, L. and I.C. Ume, *Weld quality inspection using laser-EMAT ultrasonic system and C-scan method.* AIP Conference Proceedings, 2014. **1581**(1): p. 412-419.
48. Hughes, D., *V. Induction-balance and experimental researches therewith.* The London, Edinburgh, and Dublin Philosophical Magazine and Journal of Science, 1879. **8**(46): p. 50-56.
49. Forster, F., * *THEORETISCHE UND EXPERIMENTELLE GRUNDLAGEN DER ZERSTORUNGSFREIEN WERKSTOFFPRUFUNG MIT WIRBELSTROMVERFAHREN. 1. DAS TASTSPULVERFAHREN.* Zeitschrift fur Metallkunde, 1952. **43**(5): p. 163-171.
50. Forster, F. and K. Stambke, * *THEORETISCHE UND EXPERIMENTELLE GRUNDLAGEN DER ZERSTORUNGSFREIEN*

WERKSTOFFPRUFUNG MIT WIRBELSTROMVERFAHREN. 3. VERFAHREN MIT DURCHLAUFSPULE ZUR QUANTITATIVEN ZERSTORUNGSFREIEN WERKSTOFFPRUFUNG. Zeitschrift fur Metallkunde, 1954. **45**(4): p. 166-179.
51. Dodd, C. and W. Deeds, *Analytical Solutions to Eddy‐Current Probe‐Coil Problems.* Journal of applied physics, 1968. **39**(6): p. 2829-2838.
52. Dodd, C.V., et al., *SOME EDDY-CURRENT PROBLEMS AND THEIR INTEGRAL SOLUTIONS*. 1969, Oak Ridge National Lab., Tenn.
53. Raj, B., et al., *Non-destructive testing of welds*. 2000: Narosa publishing house New Delhi, India.
54. Tumanski, S., *Induction coil sensors—A review.* Measurement Science and Technology, 2007. **18**(3): p. R31.
55. Grimberg, R., *Electromagnetic nondestructive evaluation: present and future.* Strojniški vestnik-Journal of Mechanical Engineering, 2011. **57**(3): p. 204-217.
56. Yin, W., S.J. Dickinson, and A. Peyton, *Imaging the continuous conductivity profile within layered metal structures using inductance spectroscopy.* Sensors Journal, IEEE, 2005. **5**(2): p. 161-166.
57. Mook, G., F. Michel, and J. Simonin, *Electromagnetic imaging using probe arrays.* Strojniški vestnik-Journal of Mechanical Engineering, 2011. **57**(3): p. 227-236.
58. Helifa, B., et al., *Detection and measurement of surface cracks in ferromagnetic materials using eddy current testing.* NDT & E International, 2006. **39**(5): p. 384-390.
59. Chen, Z., et al., *A Nondestructive Strategy for the Distinction of Natural Fatigue and Stress Corrosion Cracks Based on Signals From Eddy Current Testing.* Journal of Pressure Vessel Technology, 2006. **129**(4): p. 719-728.
60. He, Y., et al., *Pulsed eddy current imaging and frequency spectrum analysis for hidden defect nondestructive testing and evaluation.* NDT & E International, 2011. **44**(4): p. 344-352.
61. Tian, G.Y. and A. Sophian, *Defect classification using a new feature for pulsed eddy current sensors.* NDT & E International, 2005. **38**(1): p. 77-82.
62. Yusa, N., et al., *Application of eddy current inversion technique to the sizing of defects in Inconel welds with rough surfaces.* Nuclear Engineering and Design, 2005. **235**(14): p. 1469-1480.
63. Yusa, N., et al., *Detection of embedded fatigue cracks in Inconel weld overlay and the evaluation of the minimum thickness of the weld overlay using eddy current testing.* Nuclear Engineering and Design, 2006. **236**(18): p. 1852-1859.
64. Rosado, L.S., et al., *Advanced technique for non-destructive testing of friction stir welding of metals.* Measurement, 2010. **43**(8): p. 1021-1030.
65. Dmitriev, S.F., et al., *Eddy-current measuring system for analysis of alloy defects and weld seams.* Russian Engineering Research, 2016. **36**(8): p. 626-629.
66. Todorov, E.I., W.C. Mohr, and M.G. Lozev, *DETECTION AND SIZING OF FATIGUE CRACKS IN STEEL WELDS WITH ADVANCED EDDY CURRENT TECHNIQUES.* AIP Conference Proceedings, 2008. **975**(1): p. 1058-1065.

67. Postolache, O., A.L. Ribeiro, and H. Ramos. *Weld testing using eddy current probes and image processing*. in *XIX IMEKO World Congress Fundamental and Applied Metrology,(438-442), Lisbon*. 2009.
68. Todorov, E., et al., *Inspection of laser welds with array eddy current technique.* AIP Conference Proceedings, 2013. **1511**(1): p. 1065-1072.
69. Santos, T.G., P. Vilaça, and R.M. Miranda, *Electrical conductivity field analysis for evaluation of FSW joints in AA6013 and AA7075 alloys.* Journal of Materials Processing Technology, 2011. **211**(2): p. 174-180.
70. Kahrobaee, S. and M. Kashefi, *Hardness profile plotting using multi-frequency multi-output electromagnetic sensor.* NDT & E International, 2011. **44**(4): p. 335-338.
71. Sheikh Amiri, M. and M. Kashefi, *Application of eddy current nondestructive method for determination of surface carbon content in carburized steels.* NDT & E International, 2009. **42**(7): p. 618-621.
72. Uchimoto, T., et al., *Eddy current evaluation of cast irons for material characterization.* Journal of Magnetism and Magnetic Materials, 2003. **258–259**: p. 493-496.
73. Zergoug, M., et al., *Relation between mechanical microhardness and impedance variations in eddy current testing.* NDT & E International, 2004. **37**(1): p. 65-72.
74. Cook, D.M., *The theory of the electromagnetic field*. 1975: Courier Corporation.
75. Jones, D.S., *The theory of electromagnetism*. 2013: Elsevier.
76. García-Martín, J., J. Gómez-Gil, and E. Vázquez-Sánchez, *Non-Destructive Techniques Based on Eddy Current Testing.* Sensors, 2011. **11**(3): p. 2525-2565.
77. Theodoulidis, T. and J.R. Bowler, *Interaction of an Eddy-Current Coil With a Right-Angled Conductive Wedge.* IEEE Transactions on Magnetics, 2010. **46**(4): p. 1034-1042.
78. Yin, W., A.J. Peyton, and S.J. Dickinson, *Simultaneous measurement of distance and thickness of a thin metal plate with an electromagnetic sensor using a simplified model.* IEEE Transactions on Instrumentation and Measurement, 2004. **53**(4): p. 1335-1338.
79. Yin, W., et al. *Analysis of the Lift-off Effect of Phase Spectra for Eddy Current Sensors*. in *2005 IEEE Instrumentationand Measurement Technology Conference Proceedings*. 2005.
80. Yin, W. and A.J. Peyton, *A planar EMT system for the detection of faults on thin metallic plates.* Measurement Science and Technology, 2006. **17**(8): p. 2130-2135.
81. Yin, W. and A.J. Peyton, *Thickness Measurement of Metallic Plates With an Electromagnetic Sensor Using Phase Signature Analysis.* IEEE Transactions on Instrumentation and Measurement, 2008. **57**(8): p. 1803-1807.
82. Yin, W., et al., *Noncontact Characterization of Carbon-Fiber-Reinforced Plastics Using Multifrequency Eddy Current Sensors.* IEEE Transactions on Instrumentation and Measurement, 2009. **58**(3): p. 738-743.
83. Lu, M., et al., *A Novel Compensation Algorithm for Thickness Measurement Immune to Lift-Off Variations Using Eddy Current*

Method. IEEE Transactions on Instrumentation and Measurement, 2016. **65**(12): p. 2773-2779.
84. Lu, M., H. Xu, et al., *Conductivity Lift-off Invariance and measurement of permeability for ferrite metallic plates.* NDT & E International, 2018. **95**: p. 36-44.
85. Zhou, D., et al., *Influence of key factors on Eddy current testing sensitivity and monotonicity on subsurface depth for ferromagnetic and non-ferromagnetic materials.* Sensors and Actuators A: Physical, 2018. **278**: p. 98-110.
86. Zhou, H.T., et al., *Study on the Optimization of Eddy Current Testing Coil and the Defect Detection Sensitivity.* Procedia Engineering, 2015. **130**: p. 1649-1657.
87. Wilde, J. and Y. Lai, *Design optimization of an eddy current sensor using the finite-elements method.* Microelectronics Reliability, 2003. **43**(3): p. 345-349.
88. Chady, T. and R. Sikora, *Optimization of eddy-current sensor for multifrequency systems.* IEEE Transactions on Magnetics, 2003. **39**(3): p. 1313-1316.
89. Nabavi, M.R. and S.N. Nihtianov, *Design Strategies for Eddy-Current Displacement Sensor Systems: Review and Recommendations.* IEEE Sensors Journal, 2012. **12**(12): p. 3346-3355.
90. Thollon, F., et al., *Numerical and experimental study of eddy current probes in NDT of structures with deep flaws.* NDT & E International, 1995. **28**(2): p. 97-102.
91. Zhou, D., et al., *Influence of metallic shields on pulsed eddy current sensor for ferromagnetic materials defect detection.* Sensors and Actuators A: Physical, 2016. **248**: p. 162-172.
92. Yin, W., S.J. Dickinson, and A.J. Peyton, *A multi-frequency impedance analysing instrument for eddy current testing.* Measurement Science and Technology, 2006. **17**(2): p. 393-402.
93. Avila, J.R.S., et al. *A multi-frequency NDT system for imaging and detection of cracks*. in *2018 IEEE International Symposium on Circuits and Systems (ISCAS)*. 2018.
94. Yu, Y., et al., *Conductivity Invariance Phenomenon of Eddy Current NDT: Investigation, Verification, and Application.* IEEE Transactions on Magnetics, 2017. **53**(1): p. 1-7.
95. Ma, X., A. Peyton, and Y. Zhao, *Eddy current measurements of electrical conductivity and magnetic permeability of porous metals.* NDT & E International, 2006. **39**(7): p. 562-568.
96. Yin, W. and A. Peyton, *Thickness measurement of non-magnetic plates using multi-frequency eddy current sensors.* Ndt & E International, 2007. **40**(1): p. 43-48.
97. Yin, W., et al., *Measurement of permeability and ferrite/austenite phase fraction using a multi-frequency electromagnetic sensor.* NDT & e International, 2009. **42**(1): p. 64-68.
98. Xu, H., et al., *Imaging x70 weld cross-section using electromagnetic testing.* NDT & E International, 2018. **98**: p. 155-160.
99. Xu, H., et al., *Imaging a weld cross-section using a novel frequency feature in multi-frequency eddy current testing.* Insight-Non-Destructive Testing and Condition Monitoring, 2019. **61**(12): p. 738-743.

100. Ishigami, A., et al., *The effect of the weld fusion zone shape on residual stress in submerged arc welding.* The International Journal of Advanced Manufacturing Technology, 2017. **90**(9): p. 3451-3464.
101. Zhu, W., et al., *Modeling and experimental study of a multi-frequency electromagnetic sensor system for rail decarburisation measurement.* NDT & E International, 2017. **86**: p. 1-6.
102. Lu, M., et al., *Reducing the Lift-Off Effect on Permeability Measurement for Magnetic Plates From Multifrequency Induction Data.* IEEE Transactions on Instrumentation and Measurement, 2018. **67**(1): p. 167-174.